

Møller Scattering at Low Energy

by

Charles S. Epstein

S.B. in Physics, Massachusetts Institute of Technology (2013)

Submitted to the Department of Physics
in partial fulfillment of the requirements for the degree of

Doctor of Philosophy

at the

MASSACHUSETTS INSTITUTE OF TECHNOLOGY

September 2018

© Massachusetts Institute of Technology 2018. All rights reserved.

Author
Department of Physics
August 17, 2018

Certified by
Richard G. Milner
Professor of Physics
Thesis Supervisor

Accepted by
Nergis Mavalvala
Associate Department Head, Physics

Møller Scattering at Low Energy

by

Charles S. Epstein

Submitted to the Department of Physics
on August 17, 2018, in partial fulfillment of the
requirements for the degree of
Doctor of Philosophy

Abstract

Møller scattering is one of the most fundamental processes in QED. Its knowledge at high precision is necessary for a variety of modern nuclear and particle physics experiments. However, most treatments have neglected the electron mass, which is an approximation that breaks down at relevant low energies. In this thesis, existing soft-photon radiative corrections were combined with new hard-photon bremsstrahlung calculations to take into account the effect of photon emission at any photon energy. The electron mass was included at all steps. The radiative corrections were compiled into a Monte Carlo event generator. To test the results, an experiment was designed, constructed, installed, and executed at the MIT High Voltage Research Laboratory. Measurements are reported, comparing the simulated radiative Møller spectra to data at 2.5 MeV. Good agreement between the measurements and the new calculation is observed in the momentum spectrum at three angles.

Thesis Supervisor: Richard G. Milner
Title: Professor of Physics

THIS PAGE INTENTIONALLY LEFT BLANK

Acknowledgments

This project would not have been possible without the collaborative effort of a wide group of people. I have been fortunate to work with not just great collaborators, but also great people, and I have enjoyed my time working with them immensely.

To begin, I am especially grateful to my advisor, Richard Milner, for his incredible support throughout this whole process. Richard has been an endless source of excellent ideas and advice, as well as unfailing positivity. I in particular owe it to Richard for noticing and promoting the opportunity to run this experiment at the HVRL, and I am extremely grateful for having had the privilege to work with and learn from him. I would also like to especially thank my other committee members, Profs. Peter Fisher and Jesse Thaler. Peter, in addition to Richard, has generously lent his valuable time, expertise, and support towards making this experiment happen. I would also like to thank the DOE NNSA and the staff at the Krell Institute, for providing me four years of excellent support under the Stewardship Science Graduate Fellowship.

It has been a true privilege working with the engineers and staff at the MIT Bates Research and Engineering Center. While I risk omitting someone by listing names, I would like to especially thank Jim Kelsey, Ernie Ihloff, Joe Dodge, Peter Binns, Chris Tschalär, Brian O'Rourke, Bob Abruzzio, and Chris Vidal, without whom none of this would have ever been possible. Their engineering support has been world-class, and their camaraderie invaluable. They have each helped in so many ways that I cannot begin to list. I am extremely grateful to Joe for his tireless hands-on work making our experiment a reality, and for dealing on short notice with our varied, and often convoluted requests.

I would also like to thank Chathan Cooke of the MIT High Voltage Research Laboratory, for his extraordinary support of our endeavor. He has been extremely flexible with our timeline, and a continuous source of good experimental ideas. Chat has singlehandedly kept the accelerator in working condition over recent years, and has provided so much of his time to operate it for us at practically any moment.

In addition, Doug Hasell, Steve Steadman, Jan Bernauer, Ivica Frišćić, and Ross Corliss have provided a huge amount of support over the course of this experiment. Jan deserves an immense amount of credit for designing the amplifier/discriminator cards that read out our detector, and for providing his expertise in more areas than I can count. Thank you also to Karen Dow, for teaching me so many techniques for how to do a precise optical survey of our detector. Thank you as well to Bill Donnelly and Mike Williams, for enlightening discussions respectively about electron scattering and iterative unfolding. And

while not still with the group, I deeply appreciate the contributions of both Jan Balewski and Tom Willard; Jan helped identify DarkLight's original issue with Møllers that motivated the start of this experiment, and Tom performed much of the initial experimental engineering design.

Fellow students Bobby Johnston, Sangbaek Lee, Patrick Moran, and Yimin Wang also deserve a special thank-you. They have generously been available to help at a moment's notice with so many aspects of this experiment. Thank you as well to Bobby for working with Bates to design and construct a Faraday Cup in his first few weeks as a graduate student. Thank you Yimin for lending his extreme skill at assembling electronics.

Even though for the most part I did not work directly with them, I have had the privilege of working in parallel with a wonderful group of now-former graduate students, including Axel Schmidt, Brian Henderson, John Hardin, Becky Russell, Lauren Ice, and Colton O'Connor. I have learned an immense amount from them, and our time together has yielded a countless number of hilarious and unforgettable moments. I owe a special thanks to Axel, who taught me an extraordinary amount over the years, including how to write an event generator. I am also grateful for all of the time spent with Axel and Richard rocking out with our band The Quantum Beats. And of course, I will miss my time with the intramural physics hockey team, the Annihilation Operators.

Looking further back in time, I would like to thank all of my teachers that helped me solidify my love of science, especially Brian Gauvin and Robert Schwartz. Mr. Schwartz helped me complete a lab in which I measured the electron mass, which turned out to be a very prescient topic!

None of this would have been possible without my parents, Phyllis and Earl. Thank you, Mom and Dad, for facilitating all of my childhood science obsessions, for helping me build a hovercraft in elementary school, for showing me how circuits work, for letting me take apart old answering machines in the car even though I would lose pieces everywhere. Thank you for your love and support.

Lastly, my fiancée, Diana, has been a constant source of inspiration, support, love, and happiness, especially throughout the crunch of the last few years. I am relieved that my frequent complaining did not deter her from following her dream and pursuing her own career in physics, and I can only aspire to match her optimism and kindness. Thank you, Diana.

Contents

1	Introduction	17
1.1	Low Energy Electron Scattering	17
1.1.1	Electron-Nucleus Scattering	18
1.1.2	Møller Scattering	20
1.2	Experimental Motivation	21
2	Radiative Corrections and the Event Generator	25
2.1	Approach to the Radiative Corrections	25
2.2	Treatment of the Radiative Corrections	28
2.2.1	Elastic Events with Soft-Photon Radiative Corrections	30
2.2.2	Hard Bremsstrahlung Events	31
2.3	Results of the Calculation	32
2.4	Description of the Generator	37
2.4.1	Considerations for Weighted Event Generation	38
2.4.2	Notes on Running the Generator	39
2.4.3	Proper Counting of Møller Electrons	40
2.5	Event Generation Algorithm	41
2.6	Radiative Pair Annihilation Generator	42
3	The HVRL eBeam Facility	43
3.1	Main Structure of the Accelerator	43
3.1.1	Setting the voltage and current	43
3.2	Components Inside the Tank	45
3.3	Control Panel Components	50
3.4	Typical Operating Conditions	50
4	Design and Commissioning of the Radiative Møller Experiment	55
4.1	Development of an Experiment at the HVRL	55
4.1.1	Design of a Focusing Spectrometer	55
4.1.2	Considerations for Luminosity Monitoring	56
4.1.3	Continuous versus Discrete Angles	60

4.2	Experimental Design	62
4.3	Estimation of Target Foil Heating	62
4.4	Considerations on Overall Precision	75
4.5	Possible Measurement of the Beam Energy	77
4.5.1	Direct Calculation of the Uncertainty	83
4.5.2	Surveying and Current Measurement Precision	83
4.6	Focal Plane Detector	86
4.6.1	SiPMs and Readout Electronics	86
4.6.2	Detector Construction	91
4.6.3	Initial Idealized Simulations	91
4.7	Commissioning Run	94
4.7.1	Beam Delivery and Focus	94
4.7.2	Target Scan	95
4.7.3	Accelerator Optimization	97
4.7.4	Conclusions from the Commissioning Run	99
4.8	Upgrades Installed after the Commissioning Run	99
4.8.1	Faraday Cup	99
4.8.2	Quadrupoles and Steering Magnets	99
5	Slow Control and Data Acquisition Systems	107
5.1	Data Acquisition with the VME TDC	107
5.1.1	Programming the TDC	108
5.2	Data Acquisition Software	109
5.2.1	Software Structure	110
5.3	Magnets and their Controls	112
5.4	LabView Control Software	113
5.5	Typical Run Protocol	114
6	Data Analysis and Results	115
6.1	Construction of a Matching Simulation	115
6.1.1	Event Generators used in Simulation	116
6.1.2	Consideration of Systematic Uncertainties	116
6.2	Calibration of the Spectrometer Mapping	118
6.3	Estimation of the Detector Efficiencies	118
6.3.1	Detector Rate Linearity	121
6.4	Comparison of Data with Simulation	121
6.5	Discussion and Future Directions	124
A	DAQ and TDC Software Documentation	131
A.1	DAQ Code Documentation	131

- A.1.1 Readers 132
 - A.1.2 Processors 132
 - A.1.3 Detectors 133
 - A.1.4 Internal / Auxiliary 134
- A.2 File Documentation 136
 - A.2.1 Readers.pyx 136
 - A.2.2 Detectors.pyx 136
 - A.2.3 Processors.pyx 136
 - A.2.4 Display.pyx 137
 - A.2.5 PyDAQ.pyx 137
- A.3 Example TDC configuration script 138
- A.4 Example Run Script 139

B Software Development 141

- B.1 The QSquared Data Analysis Toolkit 141
- B.2 GDML Generation in Python 142
 - B.2.1 General Workflow 142
 - B.2.2 Overview of File Contents 142
 - B.2.3 Classes and Methods 143
 - B.2.4 Project Structure 147

List of Figures

- 1-1 Leading-order electron-muon Feynman diagram. 18
- 1-2 Leading-order electron-proton Feynman diagram. 19
- 1-3 Leading-order Feynman diagrams for Møller scattering. 21
- 1-4 Schematic of the DarkLight experiment, showing the Møller envelope (the largest radius to which Møller electrons can bend within the solenoidal field). 22
- 1-5 Geant4 simulation of Møller electrons in the DarkLight experiment. (J. Balewski) 23

- 2-1 Comparison of the Møller radiative correction term, δ , for a 100 MeV DarkLight beam at 5° in the CM frame for different electron masses. With $m_e = 0$ (Tsai [14]), the downward-sloping behavior is unphysical; this is fixed when the electron mass is taken into account (Kaiser [18]). 27
- 2-2 The Møller radiative correction term from Tsai [14], in the CM frame at an energy corresponding to a 100 MeV lab-frame beam. Note the unphysical change in sign of the slope. 27
- 2-3 The Møller radiative correction term from Kaiser [18], in the CM frame at an energy corresponding to a 100 MeV lab-frame beam. The inclusion of the electron mass has eliminated the unphysical change in sign of the slope. 28
- 2-4 Feynman diagrams for radiative Møller scattering. 28
- 2-5 Feynman diagrams for radiative Bhabha scattering. 29
- 2-6 Single-loop Feynman diagrams for Møller scattering. 29
- 2-7 Single-loop Feynman diagrams for Bhabha scattering. 29
- 2-8 Cross-sections for hard bremsstrahlung (thick lines) compared with soft-photon corrections (thin lines [18]) at various center-of-mass frame lepton angles for Møller and Bhabha Scattering, for the range $\xi < E_\gamma < E_{\gamma_0}$. 33

- 2-9 Ratio of hard bremsstrahlung (Eq. 2.10) to the soft-photon corrections (Eq. 2.9). The agreement as $E_\gamma \rightarrow \xi$ indicates the bremsstrahlung behaves as expected. Deviations from unity are expected as the soft-photon approximation breaks down. 34
- 2-10 Bremsstrahlung cross-section at various center-of-mass frame lepton angles for Møller and Bhabha Scattering, plotted at the highest-allowable photon energies. 35
- 2-11 This work (line) compared with BabaYaga@NLO at order alpha (boxes), for detecting an electron at 90° in the CM frame, as a function of photon energy. Box height (not visible at lower photon energies) indicates statistical Monte Carlo error. 36
- 2-12 Three possible kinematic scenarios for Møller events (CM frame with incoming beams). 40
- 2-13 The event generation decision tree. 41

- 3-1 The main accelerator tank. 44
- 3-2 Side view of the acceleration column. In this image, the beam travels downward. Not to scale. 46
- 3-3 Top view schematic of the tank. Note: the accelerating electrodes and solenoid are not shown. Not to scale. 47
- 3-4 A set of electrodes similar to those inside the tank. This particular set is optimized for ion beams and contains curved electrodes. Those used for electron beams are flat. 47
- 3-5 The acceleration column inside the tank. 48
- 3-6 The top of the acceleration column, with the cover removed. 49
- 3-7 Left accelerator control panel. 52
- 3-8 Right accelerator control panel. 53

- 4-1 Initial schematic of the experiment layout. 56
- 4-2 Schematic of distances and angles in the focusing spectrometer. 57
- 4-3 Raw Møller momentum spectrum at 25° , integrated over $\pm 0.5^\circ$, for a 2.5 MeV beam. 58
- 4-4 Scattered Møller electron energy as a function of angle, for beam energies ranging from 1–100 MeV. 58
- 4-5 Scattered Møller electron momentum as a function of angle (in the spectrometer’s range), for selected beam energies. 59
- 4-6 Differential Møller cross-section as a function of angle (in the spectrometer’s range), for selected beam energies. 59
- 4-7 Layout of the installation at the HVRL. 61

- 4-8 Cutaway view of the tungsten collimator. The center rectangular aperture defines the acceptance, and the two rotated holes provide additional conductance to allow the vacuum to equalize. 63
- 4-9 Bellows at the nominal 35° angle. 64
- 4-10 Bellows when the spectrometer is moved to 25°. 64
- 4-11 Drawing of the bellows, including dimensions. 65
- 4-12 Angle and position of the focal-plane exit window. 65
- 4-13 Front view of the experiment apparatus. 66
- 4-14 Locking pin system used to select the spectrometer angle. 66
- 4-15 The rolling apparatus used to allow movement of the main spectrometer (view from below). 67
- 4-16 Drawing of the full spectrometer apparatus. 67
- 4-17 The target ladder apparatus. 68
- 4-18 Top view drawing of the apparatus 68
- 4-19 Kapton window assembly adjacent to the focal plane. 69
- 4-20 Kapton window assembly at the rear of the spectrometer. 70
- 4-21 Cutaway view of the spectrometer magnet, showing the internal vacuum chamber. 71
- 4-22 Top view of the apparatus, including the original fixed luminosity arm (left). 72
- 4-23 The moving spectrometer arm. 73
- 4-24 Diagram of heat transfer in the foil. 74
- 4-25 5 μm target, 3 MeV, 1.0 μA beam with 0.1 mm radius. 75
- 4-26 5 μm target, 3 MeV, 10.0 μA beam with 0.1 mm radius. 76
- 4-27 5 μm target, 100 MeV, 1.0 μA beam with 0.1 mm radius. 76
- 4-28 5 μm target, 100 MeV, 10.0 μA beam with 0.1 mm radius. 77
- 4-29 The radiative Møller spectrum for beam energies of 2.6 MeV and 2.4 MeV, divided by the spectrum at 2.5 MeV. This is for scattering at 25°. Note the approximately 10% effect in the near-elastic region. 78
- 4-30 The radiative Møller spectrum at 25.1° and 24.9°, divided by the spectrum at 25.0°. This is for a 2.5 MeV beam. 78
- 4-31 The radiative Møller spectrum for beam energies of 2.51 MeV and 2.49 MeV, divided by the spectrum at 2.5 MeV. This is for scattering at 25°. 79
- 4-32 The ratio $P_{\text{mol}}/P_{\text{beam}}$ as a function of beam momentum. The beam momentum corresponding to $E_{\text{kinetic}} = 2.5$ MeV is marked. 80
- 4-33 Derivative $\partial R/\partial P_{\text{beam}}$ as a function of P_{beam} . The beam momentum corresponding to $E_{\text{kinetic}} = 2.5$ MeV is marked. 80

- 4-34 Møller electron momentum as a function of scattering angle, for a beam kinetic energy of 2.5 MeV. The spectrometer's 25°–45° acceptance is marked. 81
- 4-35 Derivative $\partial P_{\text{mol}}/\partial\theta$, as a function of θ . The spectrometer's 25°–45° acceptance is marked. 81
- 4-36 Møller momentum as a function of the beam kinetic energy, at a scattering angle of 25°. The nominal beam kinetic energy of 2.5 MeV is marked. 82
- 4-37 Derivative $\partial P_{\text{mol}}/\partial T_{\text{beam}}$. The nominal beam kinetic energy of 2.5 MeV is marked. 82
- 4-38 Uncertainty on the beam momentum δP_{beam} resulting from the error on the measurement of the current ratio. The error on the angle measurement is held at zero. 84
- 4-39 Uncertainty on the beam momentum δP_{beam} resulting from the error on the measurement of the angle. The error from the current ratio is held at zero. 84
- 4-40 Schematic of the survey layout, with the four measured angles. 85
- 4-41 Layout of the detector, including scintillating tiles, SiPMs (and boards), amplifier boards, and a frame. The image is “upside-down”; electrons travel upward from the magnet and strike this shown side first. 86
- 4-42 The scintillating tiles, in their packaging. 87
- 4-43 An amplifier board with connectors labeled. 88
- 4-44 The partially-assembled focal plane detector, showing 2 mm SiPMs oriented at an angle. 89
- 4-45 Closeup of the focal plane detector support structure. 90
- 4-46 Overall amplifier/discriminator board schematic. (J. Bernauer) 90
- 4-47 Circuit diagram for a single channel. (J. Bernauer) 91
- 4-48 Circuit diagram for the DAC component. (J. Bernauer) 92
- 4-49 Circuit diagram for the discriminator section, including the comparator. (J. Bernauer) 92
- 4-50 Diagram of the connector inputs/outputs. (J. Bernauer) 93
- 4-51 The focal plane detector, mounted to the spectrometer. Data cables are not shown. 93
- 4-52 Idealized simulated hit map on the focal plane detector for a 2.5 MeV beam at 25°. *X Fiber* corresponds to momentum (lowest left), and *Y Fiber* scattering angle (lowest top). 94
- 4-53 The commissioning run apparatus. 95

- 4-54 The commissioning run beamline configuration. The dashed line indicates the nominal border between the accelerator and the Radiative Møller apparatus. 96
- 4-55 The beam profile, without focusing. 96
- 4-56 The beam profile, after focusing by a single quadrupole. 97
- 4-57 The quadrupole installed on the beamline. 98
- 4-58 One of the beam parameters explored: the angle/position entering the 90° bend magnet (shaded area). 98
- 4-59 Diagram of the Faraday Cup construction. 100
- 4-60 Faraday Cup cutaway view including dimensions. Bracketed dimensions are in millimeters, unbracketed in inches. 101
- 4-61 The Faraday Cup, installed directly on the beamline. 102
- 4-62 The quadrupoles, steering magnets, and gate valve. 103
- 4-63 Steering magnets and quadrupoles. 104
- 4-64 Haimson steering coils, attached to the beamline. 104
- 4-65 Beam spot after installation of the quadrupoles and steerers. The halo is visible, while the majority of the beam passes through the 1/8" hole. 105
- 5-1 Diagram of the times measured in a trigger window. *Clock* refers to the bunch clock ETTT; T_A and T_B are measured using the high resolution, 98 ps timer. Based on figure from [36]. 108
- 5-2 Diagram of the configurable trigger timing options. Items in bold are programmable. Based on figure from [36]. 109
- 5-3 The data path in the acquisition software. 110
- 5-4 Layout of the experiment control panel. 112
- 6-1 The GDML model of the detector, used in Geant4 simulations. The view is into the beamline. 116
- 6-2 Fit used to determine the location of the elastic peak. The y axis is in thousands of counts. The fit indicates a peak location of 7.41 ± 0.07 (effective tile number). 119
- 6-3 Mapping from magnet current to peak position. 120
- 6-4 Mapping from hit position to momentum, for real data events. $\chi_r^2 = 1.12$. 121
- 6-5 Mapping from hit position to momentum, for simulated events. $\chi_r^2 = 0.83$. 122
- 6-6 Example of an even-odd dual-spline fit used to extract the attenuation length. Only statistical errors are shown (efficiencies have not yet been corrected). 123

- 6-7 Recovered efficiency parameters compared with truth, for a toy model. The distributions have been normalized. **124**
- 6-8 Raw constructed “flat” hit map used for efficiency reconstruction (linear color scale). **124**
- 6-9 Recovered “flat” hit map after efficiency reconstruction (linear color scale). **125**
- 6-10 Raw hit data at 30° (linear color scale). **125**
- 6-11 Recovered hit data at 30° (linear color scale). **125**
- 6-12 Simulated hit data at 30° (linear color scale). **125**
- 6-13 Normalized rate as a function of beam current. **126**
- 6-14 Data versus simulation at 30°. **127**
- 6-15 Data versus simulation at 35°. **127**
- 6-16 Data versus simulation at 40°. **128**
- 6-17 Full-scale momentum spectrum at 30°, showing the Møller and electron-carbon peaks. **128**
- 6-18 Extracted Møller cross-section, compared with theoretical calculations. **129**
- 6-19 Ratio of measured Møller cross-section to theoretical calculations. **129**
- 6-20 Radiative versus non-radiative simulation at 30°, for nominal and low-emittance beams. **130**

List of Tables

- 3.1 Solenoid currents used to achieve the minimum beam spot size at various beam energies. Shown for when the spot is optimized at both the upstairs and downstairs beam locations. 51
- 4.1 Initial Detector Design Goals 57
- 5.1 Typical TDC configuration parameters. 110
- 6.1 Selected systematic uncertainties included in simulations. 117

Chapter 1

Introduction

Møller (electron-electron) scattering is a background in electron scattering experiments, and is a purely QED process at low energies. It is theoretically straightforward to calculate, and has been so for decades. However, a modern retrospective has revealed gaps in previous treatments, particularly the omission of the electron mass in the radiative corrections. This thesis documents the effort to address these issues, and to verify the solution with data. A recalculation of radiative Møller scattering will be presented, as will a description of the effort to measure it.

1.1 Low Energy Electron Scattering

Electron scattering has been an active area of study since the 1940s. Some of the first experiments were performed using a Van de Graaff accelerator at MIT; for example, those of Buechner, Van de Graaff, and Feshbach ([1], and also [2], [3]). These experiments measured electron nucleus scattering, typically using ionization chambers. One of the first results was the validation of the Mott cross-section.

Today, we are revisiting these experiments in both scope and in actual location. However, we have approached the problem with modern detector and simulation technology in order to take a more precise look. In particular, however, our focus is on Møller (electron-electron) scattering. This is perhaps the most fundamental process in QED, and is one of the first calculations performed by students learning the trade. It is thus a natural place to start a series of measurements.

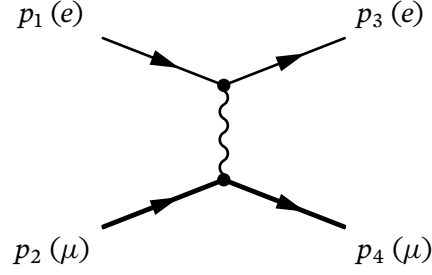


Figure 1-1: Leading-order electron-muon Feynman diagram.

1.1.1 Electron-Nucleus Scattering

Mott scattering is one of the most basic relativistic scattering processes, in which an electron scatters off a spin-zero nucleus whose recoil can be ignored. At low energies, this is a reasonable approximation. As reported in the 1947 paper by Buechner, et. al. [1], this can be described as

$$\frac{d\sigma}{d\Omega} = \left(\frac{Ze^2}{2mc^2} \right)^2 \frac{1-\beta^2}{\beta^4} \csc^4 \frac{\theta}{2} \left[1 - \beta^2 \sin^2 \frac{\theta}{2} + \frac{Z\pi\beta}{137} \cos^2 \frac{\theta}{2} \sin \frac{\theta}{2} \right]. \quad (1.1)$$

Here, Z is the atomic number of the target and β is the velocity of the incoming electron. In some sources, the higher-order terms in the brackets are omitted. This formula is valid for low Z and relatively low electron energies, and was validated to within roughly 10% below the 2 MeV level [1].

A natural next step towards understanding electron-nucleus (and electron-proton) scattering is to consider electron-muon scattering. This can be treated in the context of quantum field theory similarly to electron-proton scattering, except with an exact point-like coupling. This section closely follows a review by F. E. Close [4].

First, it is important to note that cross-sections are comprised of a Lorentz-invariant matrix-element $|M|^2$ and a phase-space factor. In particular for $2 \rightarrow 2$ scattering:

$$d\sigma = \frac{1}{|v_1 - v_2|} \frac{1}{2E_1 2E_2} |M|^2 \frac{d^3p_3}{(2\pi)^3 2E_3} \frac{d^3p_4}{(2\pi)^3 2E_4} (2\pi)^4 \delta^{(4)}(p_1 + p_2 - p_3 - p_4). \quad (1.2)$$

Here, the E_i and v_i are the energies and velocities of the particles. The matrix element can then be calculated by considering the Feynman diagram (Fig. 1-1):

$$\langle |M|^2 \rangle = \frac{1}{4} \sum_{\pm s} \left| \bar{u}(p_3) \gamma^\lambda u(p_1) \frac{e^2}{q^2} \bar{u}(p_4) \gamma_\lambda u(p_2) \right|^2 \quad (1.3)$$

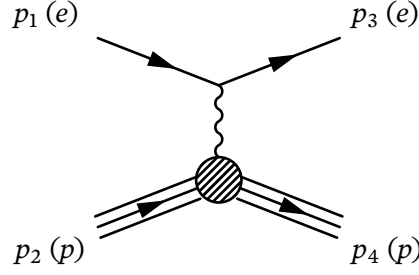


Figure 1-2: Leading-order electron-proton Feynman diagram.

where the sum (and angle brackets) indicate that we average over incoming spins and sum over outgoing spins. With the simplification

$$\sum_{\pm s} u_{\alpha}(p)\bar{u}_{\beta}(p) = (\not{p} + m)_{\alpha\beta}, \quad (1.4)$$

this can be written as

$$|M|^2 = \frac{e^4}{q^4} L_{\lambda\nu}^{(e)} L^{\lambda\nu}_{(\mu)} \quad (1.5)$$

with the electron tensor

$$L_{\lambda\nu}^{(e)} = \frac{1}{2} \text{Tr}(\not{p}_3 + m_e)\gamma_{\lambda}(\not{p}_1 + m_e)\gamma_{\nu} \quad (1.6)$$

and the muon tensor

$$L^{\lambda\nu}_{(\mu)} = \frac{1}{2} \text{Tr}(\not{p}_4 + m_{\mu})\gamma^{\lambda}(\not{p}_2 + m_{\mu})\gamma^{\nu}. \quad (1.7)$$

Evaluating this completely yields the electron-muon cross-section:

$$\frac{d\sigma}{d\Omega} = \left(\frac{d\sigma}{d\Omega} \right)_{\text{Mott}} \frac{E_3}{E_1} \left(1 + \frac{Q^2}{2m_{\mu}^2} \sin^2 \frac{\theta}{2} \right). \quad (1.8)$$

This cross-section has been decomposed into three parts: the Mott cross-section, a recoil term E_3/E_1 , and a spin term (in parentheses).

The electron-muon cross-section is an ideal starting point for considering electron-proton scattering (Fig. 1-2). Hofstadter, et. al. famously measured deviation from point-like theory, suggesting the presence of internal structure [5]. We can begin by writing the matrix element as

$$\langle |M|^2 \rangle = \frac{e^4}{q^4} L_{\lambda\nu}^{(e)} L^{\lambda\nu}_{(p)} \quad (1.9)$$

with $L_{\lambda\nu}^{(e)}$ unchanged, and

$$L_{(p)}^{\lambda\nu} = \frac{1}{2} \text{Tr}(\not{p}_4 + m_p) \Gamma^\lambda (\not{p}_2 + m_p) \Gamma^\nu. \quad (1.10)$$

Here, the coupling Γ^μ replaces γ^μ as a way to include the proton's structure:

$$\Gamma^\lambda \equiv \gamma^\lambda F_1(q^2) + \frac{\kappa F_2(q^2)}{2m_p} i\sigma^{\lambda\alpha} q_\alpha \quad (1.11)$$

where F_1 and F_2 are the Dirac and Pauli form factors, respectively, and κ is the proton's anomalous magnetic moment. Combining these yields the electron-proton cross-section:

$$\frac{d\sigma}{d\Omega} = \left(\frac{d\sigma}{d\Omega} \right)_{\text{Mott}} \frac{E_3}{E_1} \left[\left(F_1^2 + \frac{\kappa^2 Q^2}{4m_p^2} F_2^2 \right) + \frac{Q^2}{2m_p^2} (F_1 + \kappa F_2)^2 \tan^2 \frac{\theta}{2} \right]. \quad (1.12)$$

When $F_1 = 1$ and $F_2 = 0$, the electron-muon result is recovered.

More typically, the electron-proton cross-section is expressed in terms of the Sachs electric and magnetic form factors:

$$G_E \equiv F_1 - \frac{\kappa Q^2}{4m_p^2} F_2 \quad (1.13)$$

$$G_M \equiv F_1 + \kappa F_2$$

such that the cross-section becomes the well-known Rosenbluth formula:

$$\frac{d\sigma}{d\Omega} = \frac{\alpha^2}{4E_1^2 \sin^4 \theta/2} \cos^2 \frac{\theta}{2} \frac{E_3}{E_1} \left[\frac{G_E^2 + \tau G_M^2}{1 + \tau} + 2\tau G_M^2 \tan^2 \frac{\theta}{2} \right] \quad (1.14)$$

with $\tau = Q^2/4m_p^2$ [6]. This formula can be reduced to that for a spin-zero point-like nucleus by letting $m_p \rightarrow m_N$, $G_E \rightarrow Z$, and $G_M \rightarrow 0$, recovering essentially the same result as the Mott formula at very low energies.

1.1.2 Møller Scattering

The calculation of Møller scattering is quite similar to electron-muon scattering, except there are now two diagrams to be considered (Fig. 1-3). Solving these yields the spin-averaged matrix element:

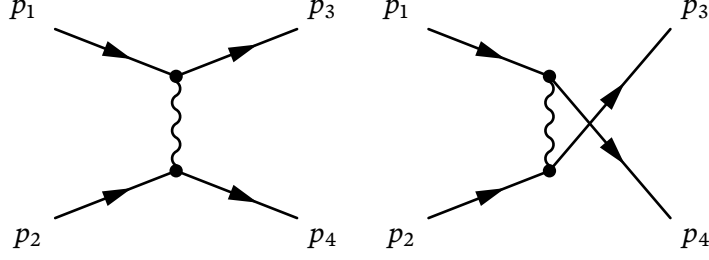


Figure 1-3: Leading-order Feynman diagrams for Møller scattering.

$$\begin{aligned}
 \langle |M|^2 \rangle = 64\pi^2\alpha^2 & \left[\frac{m^4}{t^2} \left(\frac{s^2 + u^2}{2m^4} + 4\frac{t}{m^2} - 4 \right) \right. \\
 & + \frac{m^4}{u^2} \left(\frac{t^2 + s^2}{2m^4} + 4\frac{u}{m^2} - 4 \right) \\
 & \left. + \frac{m^4}{ut} \left(\frac{s}{m^2} - 2 \right) \left(\frac{s}{m^2} - 6 \right) \right]. \quad (1.15)
 \end{aligned}$$

Here, s , t , and u are the usual Mandelstam variables. To produce a cross-section, this is combined with the scattering phase space. When expressed for identical particles in the center-of-mass frame, this takes the simple form:

$$\frac{d\sigma}{d\Omega} = \frac{\langle |M|^2 \rangle}{128\pi^2s} \quad (1.16)$$

where Ω refers to the solid-angle of a particular final-state electron. For many purposes, it is sufficient to stop here. Experiments measuring parity-violating Møller scattering, for example MØLLER [7] and E158 [8], are often interested in spin-dependent asymmetries in this cross-section, rather than the exact value. However, other experiments require a more precise understanding of Møller scattering, and for this, radiative corrections are necessary.

1.2 Experimental Motivation

This research began with an analysis of the physics processes occurring in the proposed DarkLight experiment. DarkLight aims to search for a new massive boson, the A' , by precisely measuring the process $ep \rightarrow ep e^+ e^-$. This involves scattering a high-intensity 100 MeV electron beam off a gaseous hydrogen target.

Møller scattering, owing to its large cross-section, is the highest-rate process occurring in the DarkLight detector. As a result, it is the dominant source

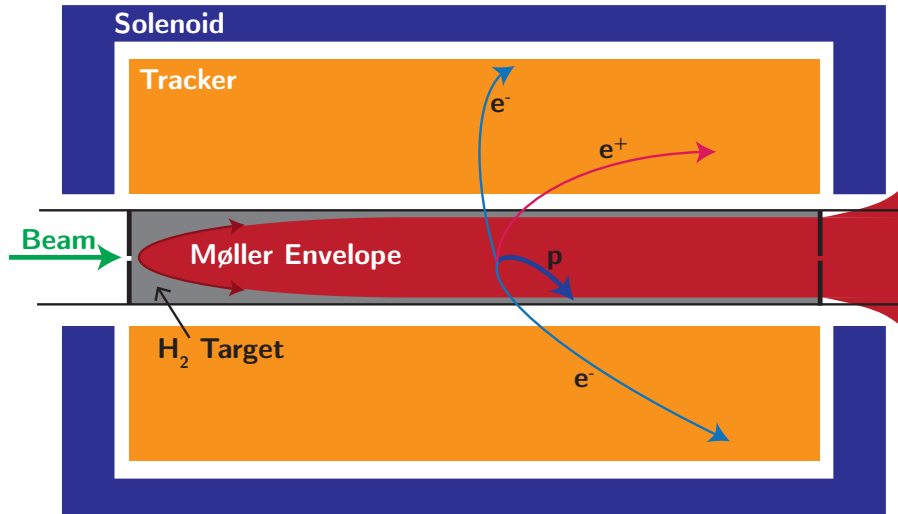


Figure 1-4: Schematic of the DarkLight experiment, showing the Møller envelope (the largest radius to which Møller electrons can bend within the solenoidal field).

of uncorrelated background. The DarkLight detector was designed to include a 0.5 T solenoid, whose purpose would not only provide momentum resolution, but focus the Møllers forward and out of the acceptance (Fig. 1-4). However, backgrounds still proved significant: as can be seen in Fig. 1-5, the Møllers exit the solenoid, defocus, and backscatter upon hitting the carbon dump. To better characterize the backgrounds, a radiative Møller generator was desired. This would help quantify the effects of not just electrons and their backgrounds, but prompt *photons* from internal bremsstrahlung.

Concurrently with DarkLight design process, data analysis of the OLYMPUS experiment was underway. The OLYMPUS experiment aimed to measure the ratio of positron-proton to electron-proton elastic scattering cross-sections in the effort to quantify the contribution of two-photon exchange. OLYMPUS acquired data with 2 GeV alternating electron and positron beams incident on a hydrogen target [9] at the DORIS storage ring at DESY. Møller/Bhabha calorimeters placed at the symmetric angle ($90^\circ_{\text{CM}} = 1.29^\circ_{\text{lab}}$) were intended as one of the luminosity monitors. Precise luminosity monitoring was important to normalize the separate electron and positron datasets and form the cross-section ratio. Since electron-electron and positron-electron scattering were the only processes in the experiment that are fully described by QED, they were the most suitable choices for normalization. A precise treatment of both Møller and Bhabha scattering, with equivalent theoretical methods, was thus desired.

As a result, it was decided to pursue the development of a Monte Carlo event

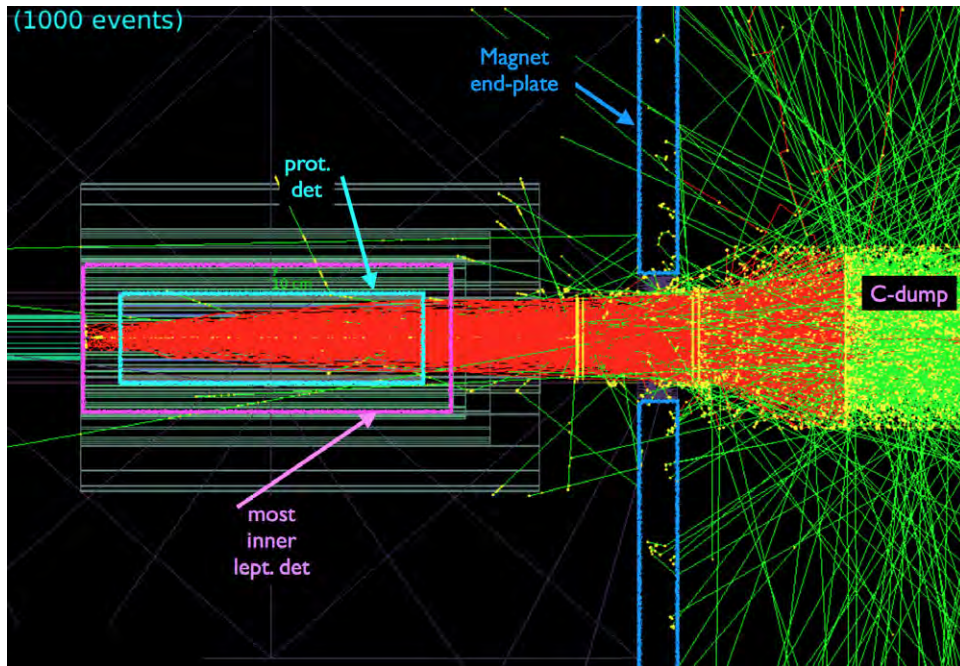


Figure 1-5: Geant4 simulation of Møller electrons in the DarkLight experiment. (J. Balewski)

generator for both Møller and Bhabha scattering, backed by calculations of the NLO radiative corrections and full bremsstrahlung. Generators existed for each, but with different underlying theoretical methods, rendering them useless as tools for precision relative normalization. In addition, it was discovered that most radiative corrections have historically neglected the electron mass. This is a prudent approximation for high-energy scattering experiments, but it catastrophically breaks down at DarkLight-scale energies.

The missing piece in the preparation of the generator was the complete, first-order bremsstrahlung for both processes. It became necessary to calculate this. After reevaluating the radiative Møller spectrum with the electron mass [10], we discovered a lack of data in the low-energy regions with which to compare our results. A plan was then developed to directly measure radiative Møller scattering in order to verify our work in this region, where the electron mass is important. The experiment eventually was installed at the Van de Graaff accelerator of the MIT High Voltage Research Laboratory (HVRL).

THIS PAGE INTENTIONALLY LEFT BLANK

Chapter 2

Radiative Corrections and the Event Generator

The OLYMPUS and DarkLight experiments demanded an improved understanding of Møller scattering, but in seemingly different regions of physics. The DarkLight design process required an understanding of the radiative photons: the Møller bremsstrahlung. The OLYMPUS analysis required a precise knowledge of the cross-sections, i.e. NLO loop-level and radiative effects. However, these processes are inextricably tied: one cannot be considered without the other.

The following sections closely trace our paper [10].

2.1 Approach to the Radiative Corrections

In modern experiments, a Monte Carlo approach is the preferred method of treating the radiative corrections. This approach stands in contrast with traditional soft-photon radiative corrections, which are typically included as a multiplicative factor to the Born cross section:

$$\left. \frac{d\sigma}{d\Omega} \right|_{\text{soft}} = (1 + \delta) \left. \frac{d\sigma}{d\Omega} \right|_{\text{Born}} \quad (2.1)$$

with $\delta = \delta(\Delta E, \Omega)$. This traditional method requires defining a cut-off ΔE : the maximum amount of energy a photon can carry away for which the event passes acceptance cuts. For an experiment having spectrometers with small, well-defined energy and angular acceptances, this formulation of the radiative corrections can be applied easily. However, for experiments with irregular acceptances, energy resolutions that may have a complex dependence on angle, or coincidence measurements, it is not feasible to quantify the radiative corrections solely by Ω and ΔE . An effective way to convolve the effects of radi-

ation with these constraints is to perform Monte Carlo simulation. There have already been Monte Carlo implementations of the radiative corrections such as MERADGEN (for Møller) [11] and BabaYaga@NLO (for Bhabha) [12, 13], but the two use different formalisms and we require a consistent treatment. Further, neither of these are flexible enough to meet the needs of OLYMPUS or DarkLight.

Previous radiative corrections to Møller and Bhabha scattering in the traditional approach [14, 15, 16, 17] have often made use of ultra-relativistic approximations in which the electron mass is assumed to be negligible relative to the momentum transfer. While this is sufficient for OLYMPUS where $Q^2 \sim 10^3 \text{ (MeV/c)}^2$ at the symmetric angle, it will not work for DarkLight. For the majority of the scattering solid-angle, the approximation $m_e^2 \ll Q^2$ does not hold, and the traditional soft-photon radiative corrections exhibit not only inaccurate, but unphysical behavior. Figure 2-1 illustrates this: a proper radiative correction factor $\delta(\Delta E, \Omega)$ should decrease as ΔE decreases, indicating the obvious conclusion that fewer events are expected in a smaller energy window.

However, when the electron mass is neglected in a region where it is important, this behavior flips: the radiative corrections *increase* with decreasing ΔE . This is unphysical and is one of the primary motivations for this work, which is required if we are to have any reliable analysis at DarkLight-scale energies. In particular, for DarkLight, $m_e^2/t > 0.1$ outside the lab-frame region of $0.93^\circ\text{--}31.98^\circ$, and the flip occurs at approximately 10° in the center-of-mass (CM) frame, which excludes the area outside approximately $0.5^\circ\text{--}49^\circ$ in the lab frame. Since for DarkLight we are interested in electrons at both very small and large angles, it is clearly crucial to include the electron mass. Nearly all existing formulations were intended for high energy scattering (e.g. [14, 17]), and only recently has there been attention to including the electron mass.

In a paper by N. Kaiser [18], the radiative corrections for soft-photon emission in both Møller and Bhabha scattering were performed in a consistent approach and without ultra-relativistic approximations. There has also been an additional recent treatment of the radiative corrections to Møller scattering beyond the ultra-relativistic limit [19]; however, we do not use it as there is no matching formulation for Bhabha scattering. In this work, we have extended the results of Kaiser with exact single hard-photon bremsstrahlung calculations. Since the energies of interest are quite low, only QED interactions have been included. The calculations, containing no ultra-relativistic approximations, permit a complete analysis of the next-to-leading-order radiative corrections for both Møller and Bhabha scattering in the low energy regions of interest.

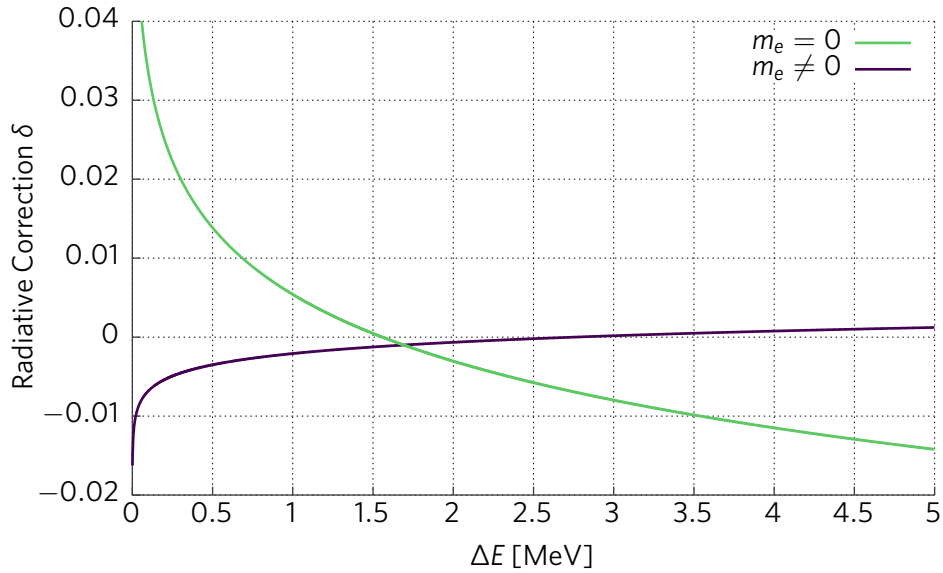


Figure 2-1: Comparison of the Møller radiative correction term, δ , for a 100 MeV DarkLight beam at 5° in the CM frame for different electron masses. With $m_e = 0$ (Tsai [14]), the downward-sloping behavior is unphysical; this is fixed when the electron mass is taken into account (Kaiser [18]).

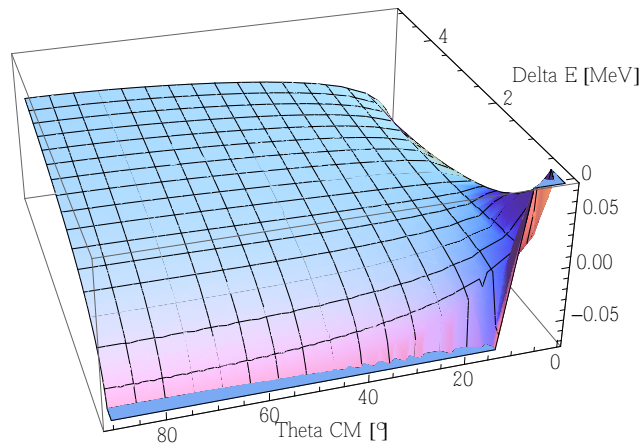


Figure 2-2: The Møller radiative correction term from Tsai [14], in the CM frame at an energy corresponding to a 100 MeV lab-frame beam. Note the unphysical change in sign of the slope.

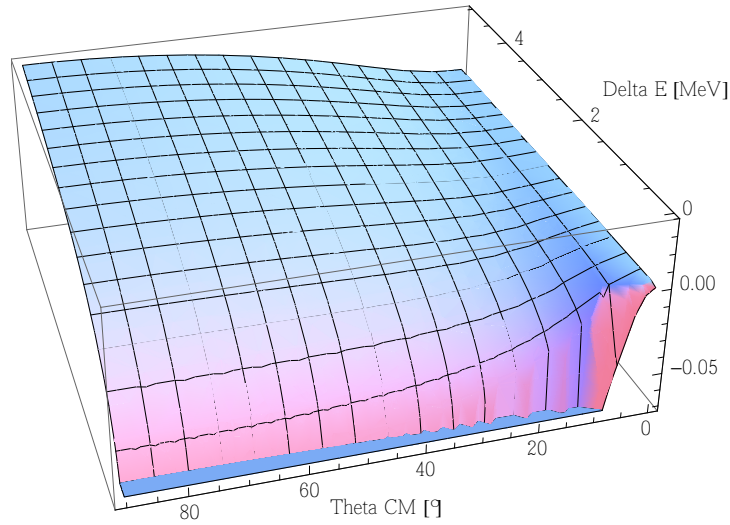


Figure 2-3: The Møller radiative correction term from Kaiser [18], in the CM frame at an energy corresponding to a 100 MeV lab-frame beam. The inclusion of the electron mass has eliminated the unphysical change in sign of the slope.

2.2 Treatment of the Radiative Corrections

Our treatment of the radiative corrections is to divide the events into two categories corresponding to the emission of photons with energy above or below a cutoff, ΔE , that separates the “soft” and “hard” regimes. In the soft regime, the events are described by elastic electron-electron kinematics with a cross-section that has been adjusted for the effects of soft-photon emission (Eq. 2.1). In the hard regime, they are described by single-photon bremsstrahlung events. The inclusion of both of these calculations allows the effects of photons of

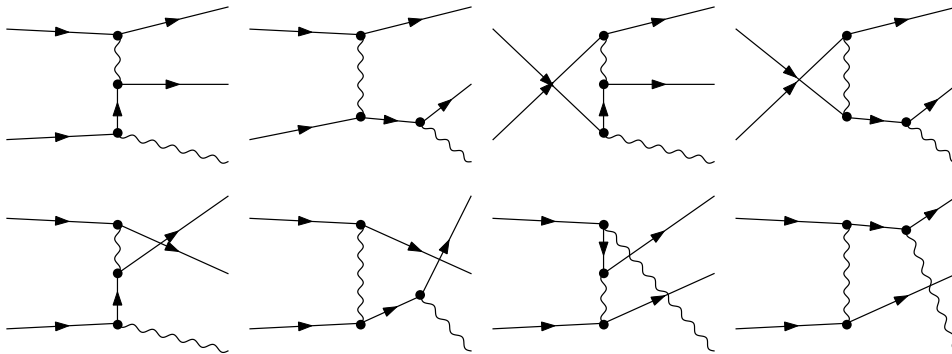


Figure 2-4: Feynman diagrams for radiative Møller scattering.

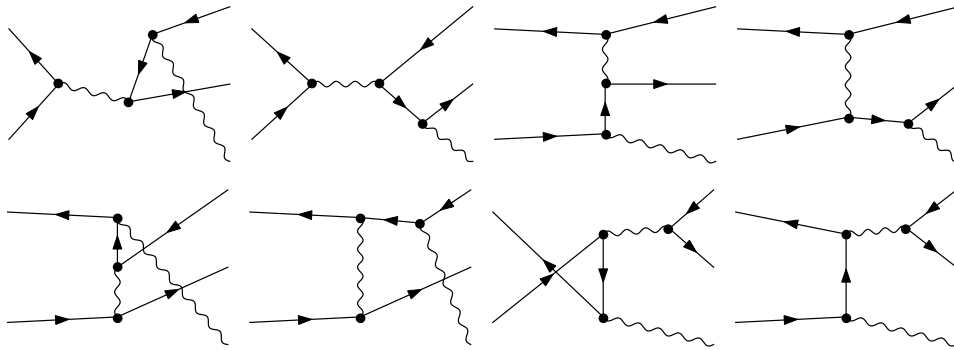


Figure 2-5: Feynman diagrams for radiative Bhabha scattering.

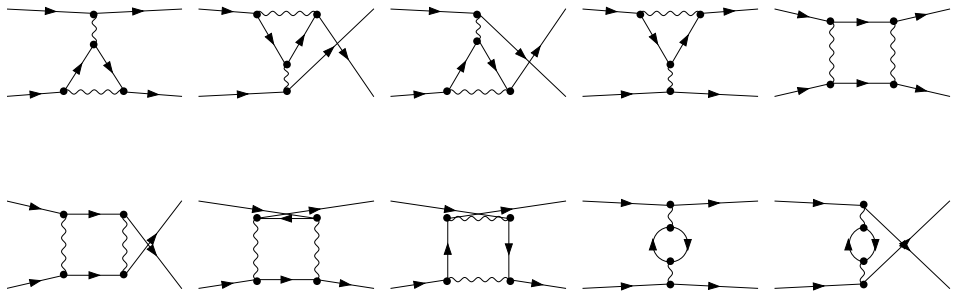


Figure 2-6: Single-loop Feynman diagrams for Møller scattering.

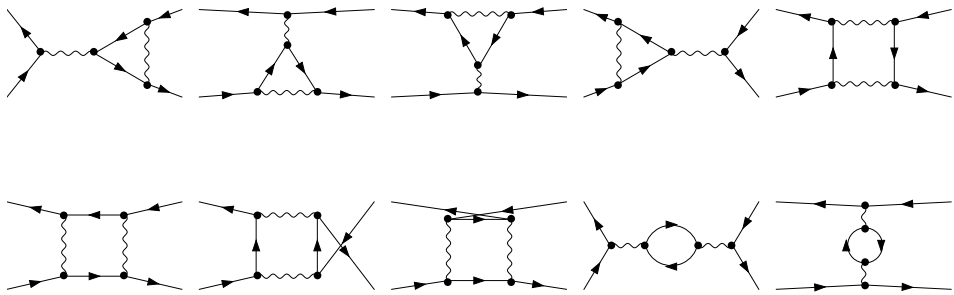


Figure 2-7: Single-loop Feynman diagrams for Bhabha scattering.

any energy to be considered. The calculations have been formulated in the center-of-mass frame to take advantage of the many kinematic simplifications.

2.2.1 Elastic Events with Soft-Photon Radiative Corrections

Events with photons below the ΔE threshold are described with elastic kinematics and a cross-section that has been adjusted from Born as in Eq. (2.1). The Born cross-section in the center-of-mass frame is given by

$$\left. \frac{d\sigma}{d\Omega_3} \right|_{\text{Born}} = \frac{\mathcal{S}\langle|M|^2\rangle}{64\pi^2s} \quad (2.2)$$

with the tree-level matrix element for Møller scattering reported earlier in Eq. (1.15). Again here, s , t , and u are the usual Mandelstam variables and Ω_3 refers to the solid-angle of a particular final-state lepton. The quantity \mathcal{S} is a symmetry factor typically equal to $\prod_j 1/n_j!$ for each n final-state identical particles of type j ¹. The matrix element for Bhabha scattering can easily be obtained from crossing symmetry by substituting $s \leftrightarrow u$.

Kaiser’s derivation of the δ radiative correction terms is presented in [18]. To produce these corrections, the cross-section for soft-photon emission is first integrated over all photon directions and energies up to ΔE . The result of this is expressed as a correction to the Born cross section; it is, however, infrared-divergent. An additional correction describing the interference between the tree-level and one-loop diagrams (Figs. 2-6, 2-7), however, contains an opposite infrared divergence [18]. Including both corrections thus produces a finite δ that can be used as in Eq. (2.1).

Equations (22) and (24) in [18] provide the terms corresponding to soft-photon emission in Møller and Bhabha scattering, respectively. While these terms contain the necessary cancellation of infrared divergences, they are incomplete because they do not describe the entirety of the effects from the one-loop diagrams. As the text indicates, additional terms must be included to achieve a complete description [18]. This remaining part of the radiative correction is provided by summing the remaining finite loop-level interference terms and dividing them by the Born terms (i.e. second line of Kaiser’s equation (2) divided by the first). The expressions needed to compute this are printed in full for Møller scattering, but the corresponding Bhabha expressions can easily be obtained by the substitution $s \leftrightarrow u$. The addition of these (ΔE -independent) loop-level terms to the soft-photon expressions completes the description

¹For real experiments measuring Møller scattering, care must be taken to properly account for both final-state electrons. When integrating over a non-trivial Ω_3 region, the symmetry factor \mathcal{S} may become a complicated function, especially for events with hard photons. See §2.4.3.

of the δ radiative correction factors for both Møller and Bhabha scattering. We also note that we have included the terms containing both electronic and muonic vacuum polarization, although the latter is negligible at the energies we are considering.

One should note that as ΔE approaches zero, the soft-photon radiative corrections diverge to negative infinity. This results from neglecting the effects of multiple soft-photon emission. The effect of multiple soft photons can be taken into account to all orders by exponentiating the correction term ($1 + \delta \rightarrow e^\delta$) [20]. However, since we consider only single hard-photon bremsstrahlung, this would give the total cross-section an artificial dependence on ΔE ; as a result, the exponentiation is not used. Our approach is self-consistent as long as ΔE is chosen to be large enough that the correction term remains small, but not so large that the soft-photon approximation becomes invalid. Later, some results will be shown with $\Delta E = 10^{-4} \sqrt{s}$, as it fulfills both of these conditions.

We note that while we do not consider them, higher-order and multiple-photon effects may not be negligible when $\mathcal{O}(0.1\%)$ absolute accuracy is desired. In the case of DarkLight, the single-photon model is sufficiently precise, as we are largely interested in the noise created by the interaction of Møller electrons/photons with the detector elements. For OLYMPUS, it is more important that the Møller and Bhabha processes be treated on equal footing, since the relevant quantity is the ratio of the cross-sections rather than the absolute value. The framework used here is not easily scalable to include higher-order effects and multiple photons in a precise manner. A different approach, such as a QED Parton Shower algorithm like that used in BabaYaga [12, 13], is better suited to analyzing multiple-photon events; however, neither method is perfect and both do require some level of approximation.

2.2.2 Hard Bremsstrahlung Events

Events with photons having energy greater than ΔE are described by an exact tree-level single-photon bremsstrahlung calculation. The spin-averaged matrix elements for

$$e_1^- + e_2^- \rightarrow e_3^- + e_4^- + \gamma$$

and

$$e_1^+ + e_2^- \rightarrow e_3^+ + e_4^- + \gamma,$$

as diagrammed in figures 2-4 and 2-5, were calculated exactly using the Mathematica plugins FeynArts and FormCalc [21]. No ultra-relativistic, soft-photon, or peaking approximations were made.

In formulating the center-of-mass phase-space parametrization for $2 \rightarrow 3$

body $ee \rightarrow ee\gamma$ scattering, we follow the approach of [22]. Combined with the matrix elements, the bremsstrahlung cross-section is then given by:

$$\frac{d^5\sigma}{dE_\gamma d\Omega_\gamma d\Omega_3} = \frac{S}{32m^2(2\pi)^5} \frac{E_\gamma}{2Ep\vartheta} \sum_\nu p_{3\nu}^2 \langle |M|^2 \rangle \quad (2.3)$$

with

$$\vartheta = \frac{1}{m} \sqrt{4E^2(E - E_\gamma)^2/m^2 - (2E - E_\gamma)^2 + E_\gamma^2 \cos^2 \alpha}, \quad (2.4)$$

where α is the angle between lepton 3 and the photon, E and p are the center-of-mass frame energy/momentum of either initial-state particle, and m is the electron mass.

The energy of lepton 3 is then given by [22]:

$$E_3 = \frac{2E(E - E_\gamma)(2E - E_\gamma) \mp m^2 E_\gamma \vartheta \cos \alpha}{(2E - E_\gamma)^2 - E_\gamma^2 \cos^2 \alpha}. \quad (2.5)$$

If the photon energy is below

$$E_{\gamma_0} = 2E(E - m)/(2E - m), \quad (2.6)$$

then only the upper sign in Eq. (2.5) is allowed. If it is above E_{γ_0} , both are allowed, and there is an additional constraint that

$$\cos \alpha < -\frac{1}{E_\gamma} \sqrt{(2E - E_\gamma)^2 - 4E^2(E - E_\gamma)^2/m^2}. \quad (2.7)$$

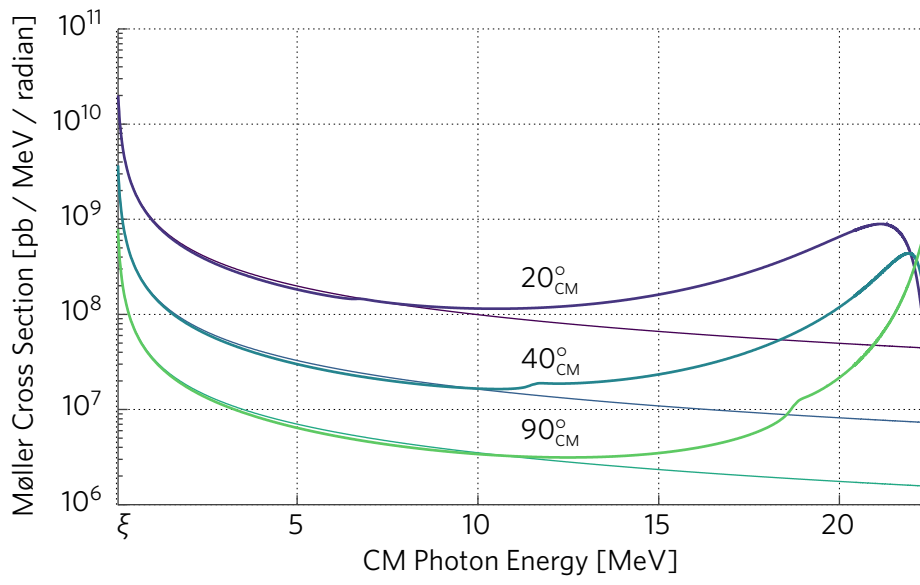
The summation in Eq. (2.3) indicates that both possible values, i.e. both signs in Eq. (2.5) should be included in the case that $E_\gamma > E_{\gamma_0}$ where both are valid. This cutoff, E_{γ_0} , is purely an artifact of this choice of variables; however, these variables are necessary in order to properly match the soft-photon and hard-photon parts of the cross-section, by defining hard photons as those with $E_\gamma > \Delta E$. We also note that the highest possible photon energy is equal to

$$E_{\gamma_{\max}} = p^2/E = E - m^2/E, \quad (2.8)$$

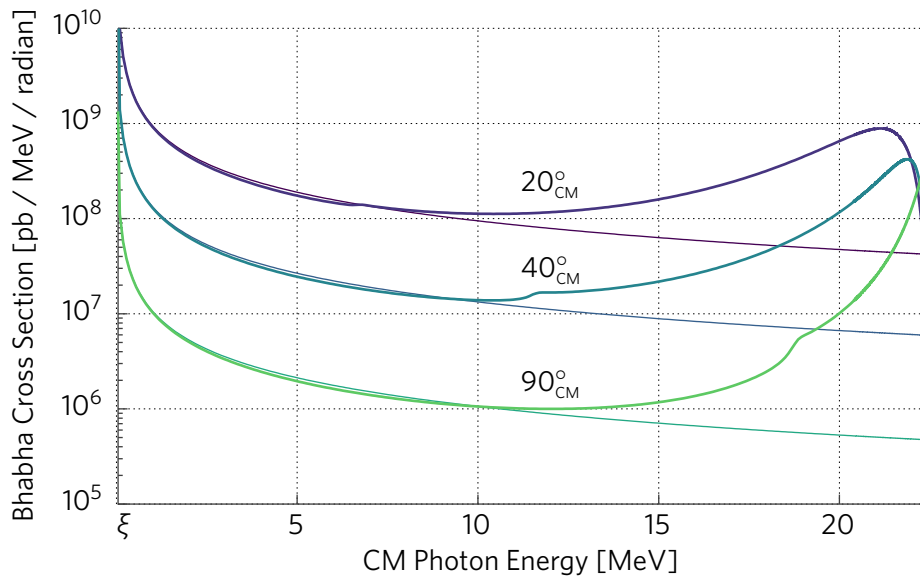
which occurs when the two outgoing leptons are emitted collinearly opposite the photon, each carrying half its momentum.

2.3 Results of the Calculation

In the following section, we present some results at a center-of-mass energy of $\sqrt{s} = 45.3$ MeV, corresponding to OLYMPUS kinematics of a 2.01 GeV beam

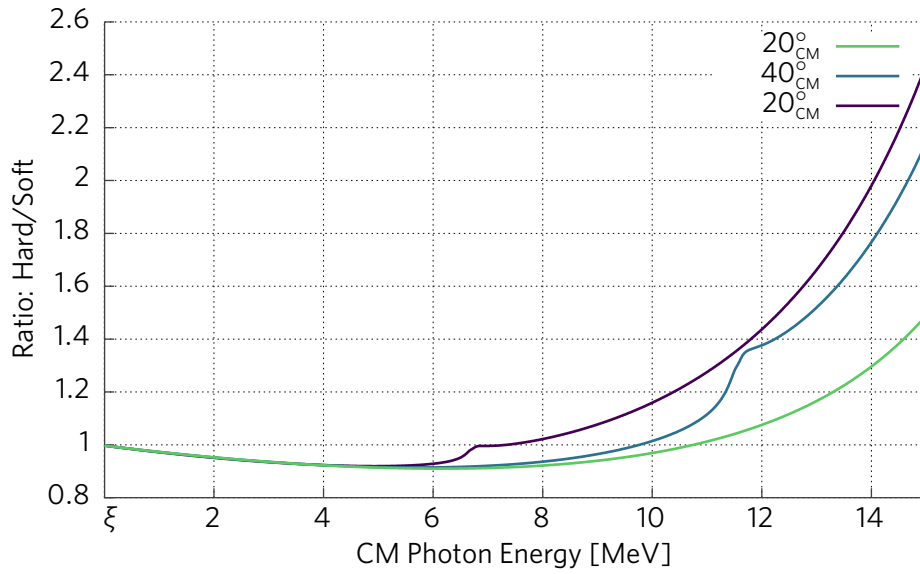


(a) Møller Scattering

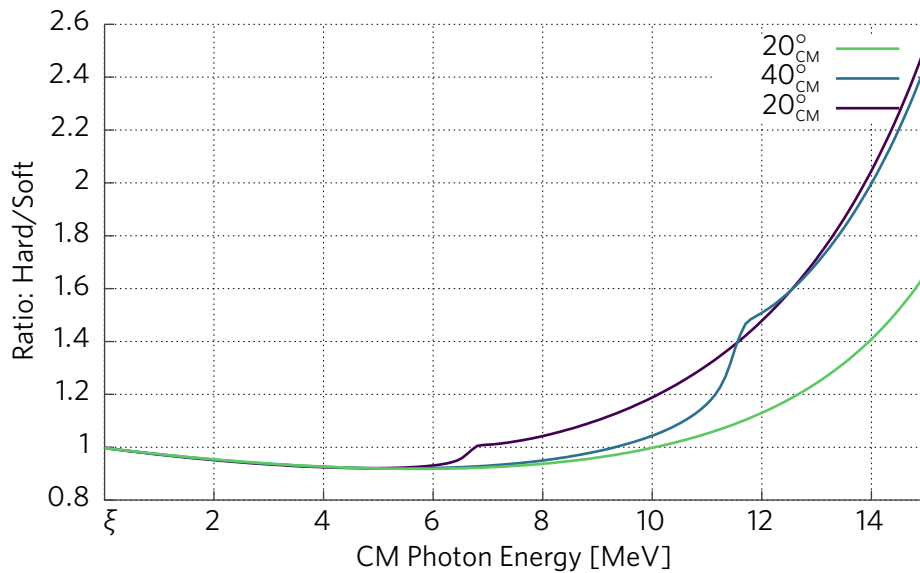


(b) Bhabha Scattering

Figure 2-8: Cross-sections for hard bremsstrahlung (thick lines) compared with soft-photon corrections (thin lines [18]) at various center-of-mass frame lepton angles for Møller and Bhabha Scattering, for the range $\xi < E_\gamma < E_{\gamma_0}$.

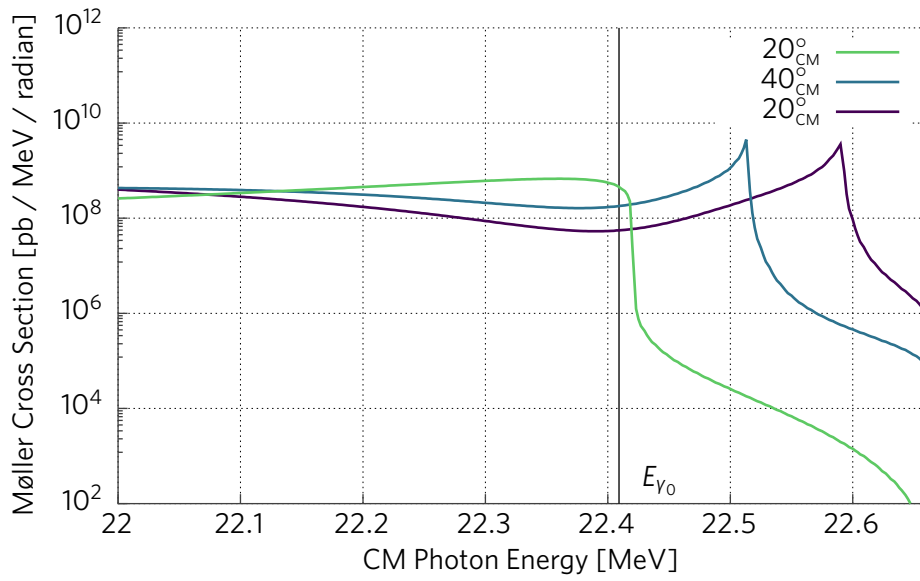


(a) Møller Scattering

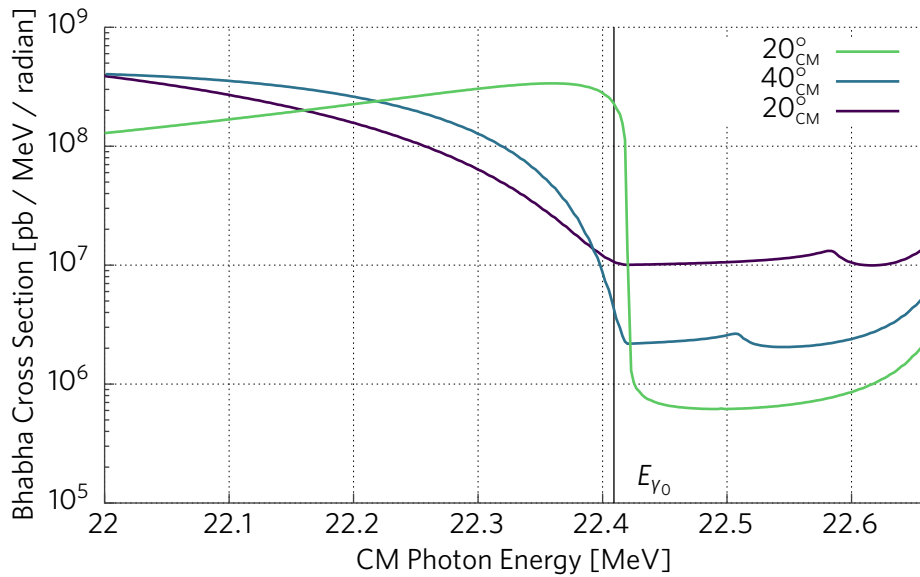


(b) Bhabha Scattering

Figure 2-9: Ratio of hard bremsstrahlung (Eq. 2.10) to the soft-photon corrections (Eq. 2.9). The agreement as $E_\gamma \rightarrow \xi$ indicates the bremsstrahlung behaves as expected. Deviations from unity are expected as the soft-photon approximation breaks down.



(a) Møller Scattering



(b) Bhabha Scattering

Figure 2-10: Bremsstrahlung cross-section at various center-of-mass frame lepton angles for Møller and Bhabha Scattering, plotted at the highest-allowable photon energies.

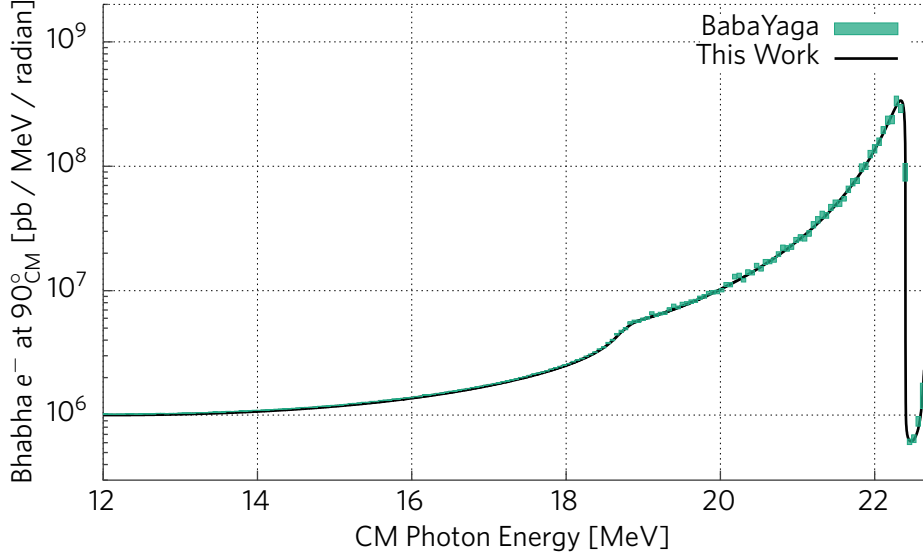


Figure 2-11: This work (line) compared with BabaYaga@NLO at order alpha (boxes), for detecting an electron at 90° in the CM frame, as a function of photon energy. Box height (not visible at lower photon energies) indicates statistical Monte Carlo error.

incident on a fixed target. These results have been calculated with $\Delta E = 10^{-4} \sqrt{s} \approx 4.5$ keV; we will refer to this particular cut-off value as ξ . In Fig. 2-8, a comparison between the hard-photon bremsstrahlung cross-section and the soft-photon-corrected cross-section is presented at three specific lepton angles for $\xi < E_\gamma < E_{\gamma_0}$. The bremsstrahlung cross-section has been numerically integrated over all photon directions, and is plotted as a function of photon energy. The soft-photon-corrected cross section has been differentiated with respect to ΔE to obtain a cross-section as a function of photon energy. This formulation produces two quantities that can be directly compared:

$$\text{Soft: } \frac{d^3\sigma}{d\Omega_3 dE_\gamma} = \frac{d}{d\Delta E} [\delta(\Omega_3, \Delta E)] \times \left. \frac{d\sigma}{d\Omega_3} \right|_{\text{Born}} \quad (2.9)$$

$$\text{Hard: } \frac{d^3\sigma}{d\Omega_3 dE_\gamma} = \int_{4\pi} \frac{d^5\sigma}{d\Omega_3 dE_\gamma d\Omega_\gamma} d\Omega_\gamma. \quad (2.10)$$

These Møller (Bhabha) cross-sections represent the probability for detecting an electron (positron) at the specified angle as a function of the energy of the emitted photon. At low photon energies, the close agreement is a validation of our code and is a reflection that the calculations properly reduce to existing soft-photon calculations at $E_\gamma = \xi$. Figure 2-9 shows a ratio of these quantities;

here, the agreement can be clearly seen by the ratio becoming unity as $E_\gamma \rightarrow \xi$.

The soft-photon cross-section (Eq. 2.9) has been plotted to photon energies that are clearly outside its range of validity in order to demonstrate its limitations. At these higher photon energies, a relative rise of the hard-photon bremsstrahlung cross-section is seen, corresponding to an increase of the cross-section resulting from initial-state radiation. Figure 2-10 shows the hard cross-sections plotted at the highest photon energies. We also note that the Møller cross-sections presented in figures 2-8(a) and 2-10(a) are that for detecting *any* electron, and may exceed other formulations by a factor of two.

In many of these plots, features such as kinks and cusps are visible, especially in the region where $E_\gamma > E_{\gamma_0}$. However, we note that in this scenario with a very high-energy photon, final-state leptons are emitted nearly collinearly (in the CM frame), and in this region the single-photon bremsstrahlung model may break down. Contributions from multiple-photon exchange/emission, final-state interactions, and atomic effects may become important in this regime. We are able to reproduce these features for the Møller case with the matrix element presented in [22]. In addition, excellent agreement with the widely-used code BabaYaga@NLO [13] (which includes the electron mass) is observed when run at order alpha (NLO). Figure 2-11 shows a comparison between our work and BabaYaga, in which the interesting features line up precisely. There is an approximately 1% deviation between our work and BabaYaga in the mid-photon-energy region (~ 12 MeV), but this is only at the lowest point of the cross-section, and likewise it contributes negligibly to the total cross-section. This may result from approaching the same physics with contrasting methods.

It should be noted that the bremsstrahlung cross-section described in these plots is divergent: it becomes infinite as the photon energy tends towards zero, motivating the plots beginning at $E_\gamma = \xi$. This illustrates the necessity of combining the bremsstrahlung calculation with soft-photon corrections, which account for effects in the region where $0 < E_\gamma < \Delta E$. The parameter ΔE sets the point at which the transition from the soft-photon corrections to full bremsstrahlung is made.

2.4 Description of the Generator

A Monte Carlo event generator was developed, based on the new calculations of Møller and Bhabha scattering. It is written in C++ using ROOT classes, and is designed for integration with existing Geant4 simulations. It can be used as a standalone event-generating executable or as a class framework that can be included in existing software. The generator performs all calculations in

the center-of-mass system. This avoids a number of kinematic complications that arise in the lab frame. However, it can easily provide properly-boosted lab frame vectors.

2.4.1 Considerations for Weighted Event Generation

The generator operates using weights: kinematic configurations are drawn randomly from pre-specified distributions, and are importance-weighted to represent the cross-section for such kinematics. An event's weight \mathcal{W} is given by

$$\mathcal{W} = \frac{d^n \sigma}{d\vec{\chi}_n}(\vec{\chi}_n) / P(\vec{\chi}_n), \quad (2.11)$$

where $\vec{\chi}_n$ represents the n independent parameters of the differential cross-section. The numerator is the differential cross-section for such parameters, and the denominator represents the probability of drawing them from the distributions.

Using weights allows analysis of all regions of phase-space with satisfactory statistical precision. For highly non-uniform distributions, such as cross-sections that are peaked in the forward direction, it can be difficult to produce a sufficient statistical analysis at all angles with an unweighted generator because far more events will be generated in the peaking regions. A weighted generator allows a more even coverage of the phase space, but the calculation of the statistical error is more complex. For weights that are similar in magnitude, the variance of the sum of the weights is well-approximated by the sum of the squared weights. However, the summation may be slow to converge on the correct value if the weights vary significantly within a bin. For this reason, it is important to draw event kinematics from a distribution that leads to each bin in the analysis receiving events with similar weight. This is strongly dependent on the specific analysis: we find that for our purposes, uniform sampling of the lepton angles provides even coverage with satisfactory convergence. However, the statistical error is significantly reduced by prior sampling of the photon angular and energy distributions.

First, an ultimately unsuccessful method was developed for rapid numerical sampling of the photon direction. This was based on sampling both the photon θ and ϕ over a small number of points (10–20 each), and performing trapezoidal integration to arrive at a cumulative distribution function for inversion sampling. An associated weight was assigned to make up the difference between the approximate trapezoidal function and the actual cross-section. The initial computation phase was quite short (~ 1 minute), and subsequent drawing from

the computed distributions was not significantly slower than uniform sampling. An array of such 2D sampling objects was created at generator initialization, one for each of a set of possible photon energies and lepton angles, and the appropriate one was accessed during generation. The result was a significant reduction in the variance of the weights without a significant slowdown.

However, this method was ultimately unsuccessful when applied to a broad range of kinematics. Inversion sampling relies on the ability to calculate a cumulative distribution function, and then invert it. This failed when the difference between the lowest and highest points in the cross-section exceeded double precision. As a result, an accurate cumulative distribution function could not be calculated, because a large number of points were not contributing to the total cross-section. This caused inaccurate event generation.

Ultimately, an adaptive Monte Carlo algorithm, known as “foam” integration, was adopted. The implementation was provided with the ROOT package as the TFOam class, and is based on [23]. This method works by dividing up the cross-section into an adaptively-shaped grid of cells having approximately the same integral. A cell is chosen, and then rejection sampling is performed within it. This circumvents the issue of numerical precision, and is much more efficient than standard rejection sampling. Additionally, the particular implementation allows functions of any dimension to be sampled.

In the end, it was decided the best option was to create an array of TFOam objects, spread evenly across electron angles. Once an electron angle was chosen (uniformly), the nearest TFOam was used to draw the photon energy and angles. This allowed us to keep sampling the electron angle uniformly, while using the TFOam integrators to choose an associated, lightly-weighted set of photon kinematics.

2.4.2 Notes on Running the Generator

In standalone mode, the generator can be completely controlled via the command line and outputs events in either tab-delimited-text or ROOT TNtuple format. All random numbers used in event generation originate from a single instance of a custom random number generator class that is then provided to the generator upon instantiation. This class must be implemented by the user as derived from the base RandGen class. In the standalone generator, an implementation is provided which draws random numbers from a ROOT TRandom3 instance.

Additionally, the user must specify the generator mode (Møller or Bhabha), the center-of-mass θ and ϕ cuts on the primary final-state lepton, and any desired modification from the default ΔE . The number of cells in the TFOams

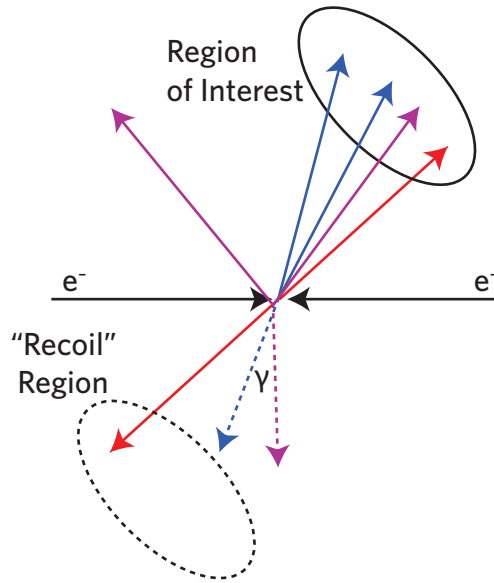


Figure 2-12: Three possible kinematic scenarios for Møller events (CM frame with incoming beams).

in which the photon angles/energies are sampled can also be specified, as well as the number of times this is performed along the range of lepton angles.

Upon generating an event, either two or three instances of `TLorentzVector` are calculated, corresponding to elastic or bremsstrahlung events. Pointers to the `TLorentzVector` instances are returned via associated class methods. The user can determine which type the event was by calling `GetElasticFlag()` which returns 1 if the event was radiative, and 0 if elastic.

2.4.3 Proper Counting of Møller Electrons

The Møller and Bhabha cross-sections are defined for a particular final state lepton to scatter into $\Delta\Omega$. In this event generator, $\Delta\Omega$ is the center-of-mass θ and ϕ region specified by the user. For Møller scattering, there is an ambiguity over which electron is chosen, since it is impossible to assign which electron was scattered and which recoiled. As a result, to obtain the physical cross-section for *all* electrons scattering into $\Delta\Omega$, the differential cross-section must be integrated over both the region of interest, and the complementary space for which the second electron enters this region. For events with two-body elastic kinematics, this is a simple task, since the complementary region is easy to define.

However, for radiative events with inelastic kinematics, the problem is somewhat more subtle. Since a photon can carry away energy and momentum,

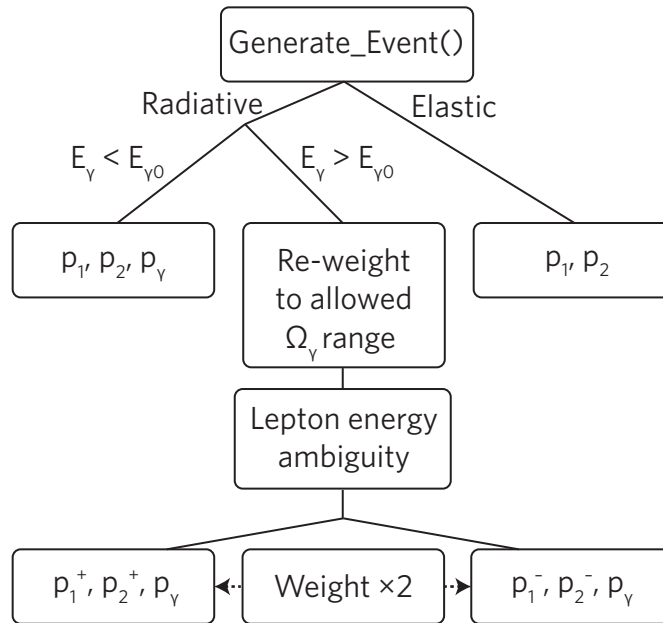


Figure 2-13: The event generation decision tree.

the complementary region is no longer simply defined (Fig. 2-12). Regardless of the choice of angular region over which the solid angle of the primary electron is integrated, there may be improper counting. If the secondary electron falls into this region as well, a corresponding kinematic configuration in which the electrons are swapped will be counted, leading to correct integration over both the primary and complementary regions. However, there may also be events where the secondary electron is emitted outside of the region of interest, and thus the swapped configuration will not be counted.

As a result, events for which only one electron enters the region of interest require an additional factor of two relative to those for which both electrons do. The generator automatically checks each Møller event for such a redundancy and adjusts the weight accordingly. The result is that the generator’s output will represent the cross-section for *all* events for which *at least one* electron falls into the angular region of interest.

2.5 Event Generation Algorithm

The generation algorithm decision tree can be seen in Fig. 2-13. When an event is requested by `Generate_Event()`, a random number is drawn to determine if it is “radiative” (hard-photon) or “elastic” (soft-photon). If the event is elastic, kinematics are drawn and the final-state vectors returned. If the event

is radiative, the process is more complex. As described in §2.2.2, there is a photon cutoff value above which two photon energies are valid, and there is a restriction on their solid angle. In the “simple” case below this cutoff, the kinematics are drawn from the relevant T Foam instance, and the vectors returned. In the more complicated case, one of the possible energies is chosen at random, and the phase-space re-weighted first to reflect the restricted angular range, and then by a factor of two for the energy ambiguity.

2.6 Radiative Pair Annihilation Generator

Notably, the scattering of low-energy positrons off atomic electrons allows an additional final-state: annihilation to two or more photons. This process is important to OLYMPUS since the Møller/Bhabha calorimeters cannot distinguish electrons, positrons, and photons. A generator was developed for this process using a similar framework to that of the Møller/Bhabha generator. In the soft-photon region, corrections were applied to the $e^+e^- \rightarrow \gamma\gamma$ cross-section [24]. In the hard-photon region, the full $e^+e^- \rightarrow 3\gamma$ cross-section was used. However, the 3γ phase-space can be parameterized in such a way that there is no kinematic ambiguity, simplifying the issue. In addition, we used the T Foam class even more extensively, to produce largely-unweighted events.

Chapter 3

The HVRL eBeam Facility

The MIT High Voltage Research Laboratory (HVRL), administered by the MIT RLE, is home to a 3 megavolt Van de Graaff electron accelerator. The HVRL is an ideal location for a measurement of radiative Møller scattering. First, it can routinely provide an electron beam up to 2.5 MeV in kinetic energy, and of $1\ \mu\text{A}$ in current. Second, the nature of the facility has allowed the experiment to be run as an ongoing operation, rather than a scheduled installation. The electron beam facility is run and maintained by Chathan Cooke. The following sections regarding its construction draw from our personal communications.

3.1 Main Structure of the Accelerator

The accelerator is housed in a large tank (Fig. 3-1). The tank is filled with approximately 95% N_2 , 5% SF_6 . It is held at a pressure of about 10 atm. During periods of frequent service, it was opened once or twice per year. However, with recent operation being largely stable, it was last opened over a year prior to our installation. Shortly after our data acquisition runs, the tank needed to be re-opened to repair a faulty beam current control relay. When the tank is opened, the gas is stored in an auxiliary tank and then re-used.

3.1.1 Setting the voltage and current

A Generating Voltmeter (GVM) reads out the terminal voltage. Its output is used in a feedback loop that sets how much current is put on the belt. The current supply is located in the main control panel. Note that this differs from some systems that use a corona discharge to remove charge from the belt. This was chosen in order to circumvent the complexity of matching two feedback systems.

The main Van de Graaff belt is turned by a motor at the bottom of the tank.



Figure 3-1: The main accelerator tank.

The belt then turns a secondary generator located at the top. This generator provides an AC current to power the thermionic source. The frequency of this AC current is thus related to the belt frequency, and its amplitude is not adjusted. The generator also powers a DC power supply that controls the extraction voltage, which ranges from about -80 V to $+15\text{ V}$. This extraction voltage, rather than the AC heating current, is used to set the beam current.

3.2 Components Inside the Tank

Figures 3-2 and 3-3 schematically show the inside of the tank. In Fig. 3-2, the letters correspond to:

A Filament

The filament is shaped like the letter “S”. The “S” curve lies in the horizontal plane. The filament is made from tungsten wire, with a diameter of about $0.25\text{--}0.5\text{ mm}$. Its approximate dimensions are $1\text{ mm} \times 2\text{ mm}$.

B Extraction plate

This is approximately hemispherical with a diameter of $\sim 4''$. It is set to a voltage ranging from -80 V to $+15\text{ V}$. Varying this voltage adjusts the current of the beam.

C First initial acceleration stage

This accelerates the electrons to $\sim 30\text{--}40\text{ kV}$. The first two electrodes are connected electrically. As in all of the acceleration sections, the electrodes are $\sim 1\text{ mm}$ thick and are spaced approximately $1''$ apart.

D Second initial acceleration stage

This accelerates the electrons to $\sim 30\text{--}50\text{ kV}$.

E Main acceleration column

This stage completes the acceleration of the electrons to their maximum energy. The electrode voltage in this section scales up linearly. Dotted lines are used here to indicate the presence of many electrode stacks.

F Base plate

This separates the acceleration column from the solenoid.

G Solenoid

An approximately $10''$ tall solenoid, with an outer diameter of roughly $8\text{--}9''$ and an inner diameter of approximately $3\text{--}4''$.

H Accelerator base

Approximately $4''$ of steel.

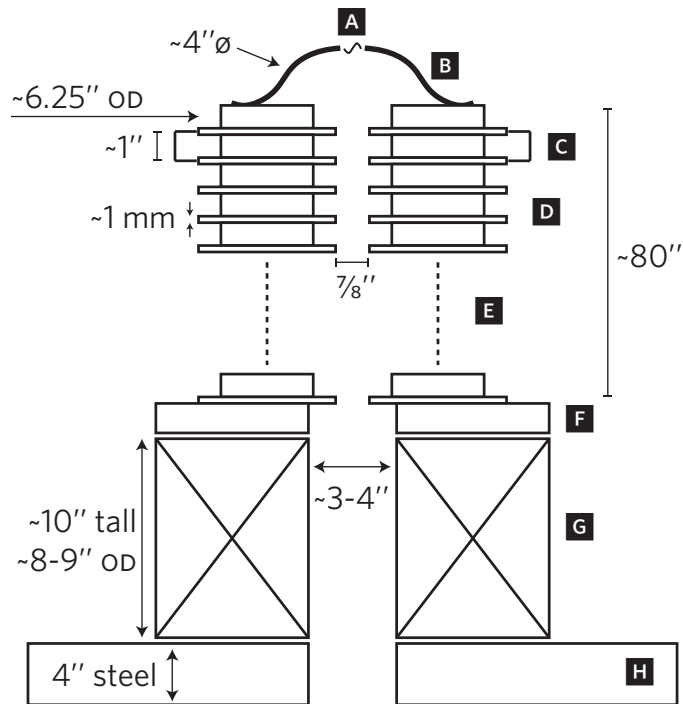


Figure 3-2: Side view of the acceleration column. In this image, the beam travels downward. Not to scale.

In Fig. 3-3, the letters correspond to:

I Beam pipe

The main beam pipe. It is roughly 6" off the center axis.

J Resistor ladder

This carries the current generated by the Van de Graaff, and sets up voltages on the inner and outer field electrodes.

K Motor and belt

The approximate location of the belt and motor. The belt is made of fabric infused with rubber.

L Outer field rings

These set up the voltage gradient in the pressurized portion of the tank. They are complementary to those inside the acceleration column.

Figure 3-5 shows a picture of the accelerator column within the tank. Figure 3-6 shows a picture of the top of the acceleration column with the cover removed; the belt is visible on the right side, and on the left, the beam tube (with red filament leads).

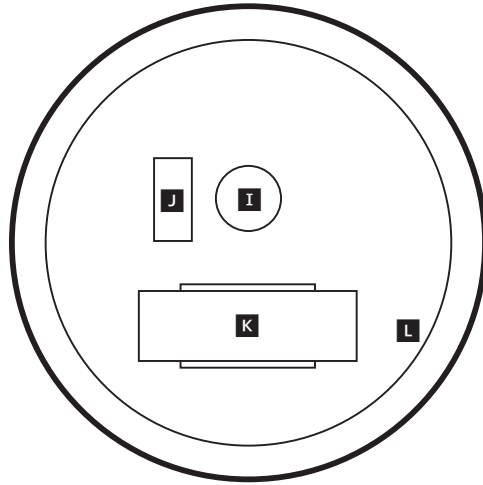


Figure 3-3: Top view schematic of the tank. Note: the accelerating electrodes and solenoid are not shown. Not to scale.



Figure 3-4: A set of electrodes similar to those inside the tank. This particular set is optimized for ion beams and contains curved electrodes. Those used for electron beams are flat.



Figure 3-5: The acceleration column inside the tank.



Figure 3-6: The top of the acceleration column, with the cover removed.

3.3 Control Panel Components

Figures (3-7) and (3-8) show the main accelerator controls. In the left panel:

0 ADC/DAC backplane

These provide digital I/O for many of the control panel's functions. These are read out in the LabView slow control system.

1 90° bend power supply

This powers the downstairs 90° bending magnet.

2 Focusing solenoid power supply

This powers the focusing solenoid inside the tank.

3 Main current supply

This power supply feeds current onto the Van de Graaff belt. The knobs control the feedback system and are not typically adjusted.

In the right panel:

4 Steering coil power supply

This powers the set of N-S and E-W steering coils located just outside the tank.

5 Digital GVM readout

This displays half the terminal voltage: the number shown must be multiplied by two to get the voltage, in MV.

6 Raw GVM readout

This shows the raw GVM current readout. This number is scaled to provide the above digital readout.

7 Current control

This controls the machine current.

8 Spray voltage

This controls how much voltage is available to the feedback system putting current on the belt.

9 Terminal voltage control

This sets the terminal voltage.

3.4 Typical Operating Conditions

According to C. Cooke, in typical operation, spot sizes of ~ 0.1 mm upstairs, and ~ 1 mm downstairs were common. Table 3.1 shows the solenoid currents that

Table 3.1: Solenoid currents used to achieve the minimum beam spot size at various beam energies. Shown for when the spot is optimized at both the upstairs and downstairs beam locations.

	Terminal Voltage (MV)	Solenoid Current (A)
Upstairs	1.5	0.67
	2.0	0.85
	2.5	1.05
	2.6	1.05
	3.0	1.15
Downstairs	0.5	0.30
	1.0	0.45
	1.5	0.55
	2.0	0.70
	2.5	0.79
	3.0	0.95

were required to achieve this. The beam diameter was measured by using it to melt a hole in scotch tape.

Vacuum gauges are located in both the upstairs and downstairs experimental areas. Upstairs, the pressure is in the vicinity of 9×10^{-8} torr. However, the downstairs gauge has recently been reaching approximately 2×10^{-5} torr. This is well above the typical scale of $\sim 1 \times 10^{-6}$ torr. This increased contamination has caused more-frequent accelerator conditioning to be necessary. The jump in pressure seems to be the result of a leak in the 90° bending magnet.

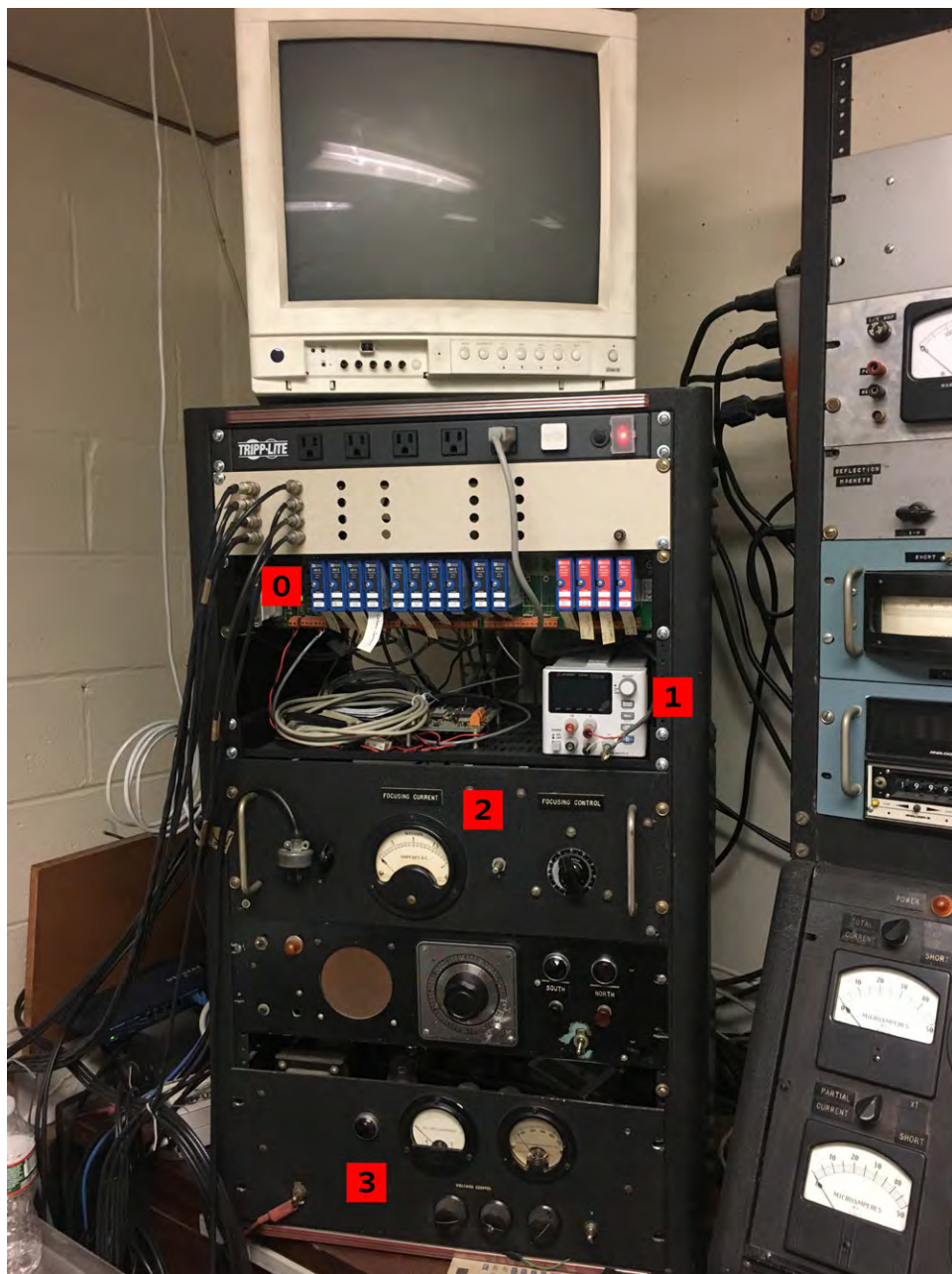


Figure 3-7: Left accelerator control panel.

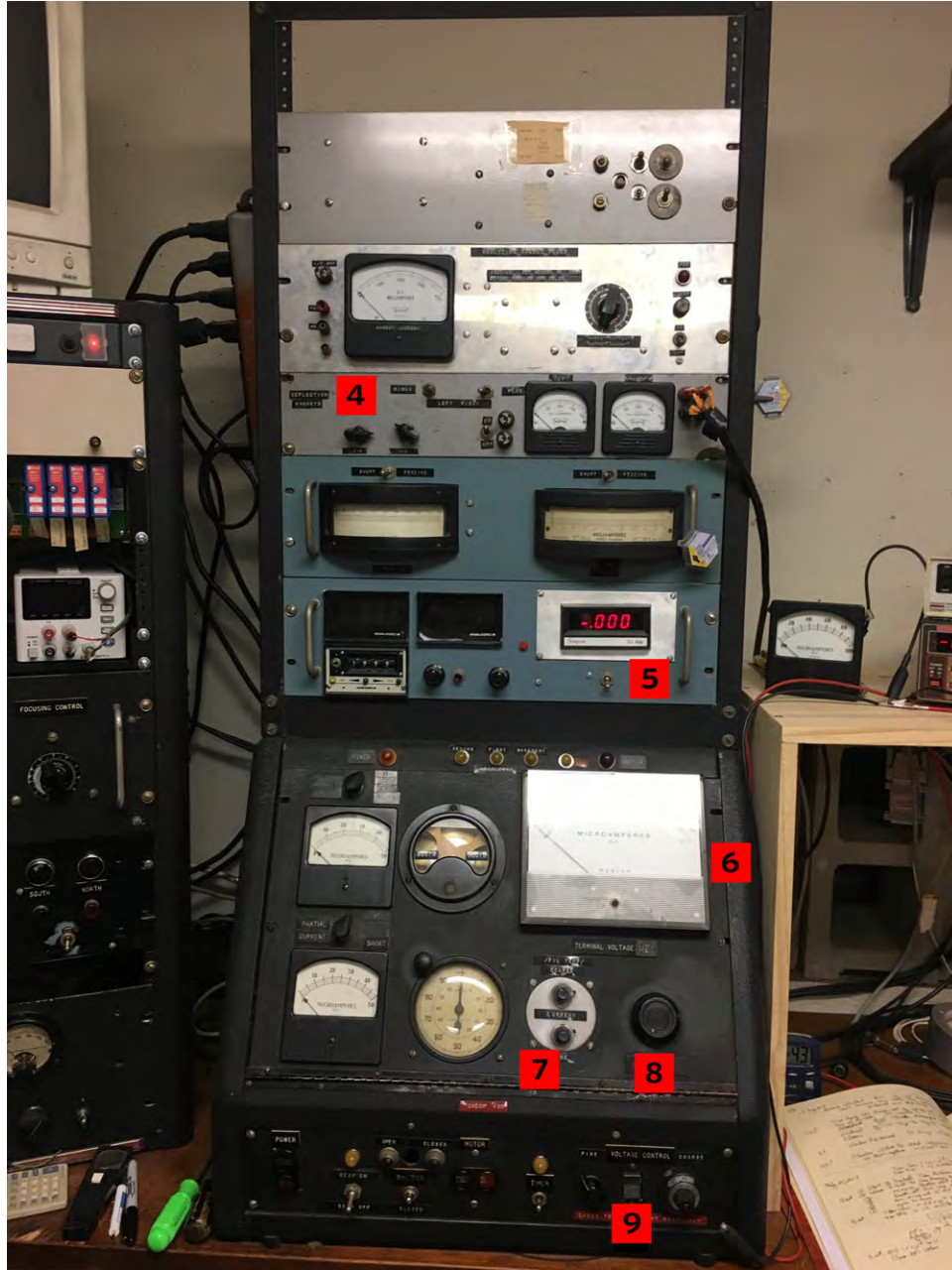


Figure 3-8: Right accelerator control panel.

THIS PAGE INTENTIONALLY LEFT BLANK

Chapter 4

Design and Commissioning of the Radiative Møller Experiment

The Radiative Møller experiment was designed, primarily, to measure the scattered-electron momentum spectrum at several different angles. In the following chapter, the experimental design and rationale are detailed.

4.1 Development of an Experiment at the HVRL

The primary goal of the experiment was to verify the new calculation of radiative Møller scattering with the electron mass. Therefore, the experiment should take place at low energy, in the region where the electron mass is important. Additionally, a layout with magnetic spectrometers is an obvious choice for an electron energy measurement. A schematic of the initially-conceived layout is shown in Fig. 4-1. There were many decisions that had to be made, in the interest of designing a realistic experiment.

4.1.1 Design of a Focusing Spectrometer

A high-precision measurement of the absolute Møller cross-section is quite difficult. This requires exceptional knowledge of the luminosity and detector acceptance. The former, especially, is particularly difficult. This informs our choice of which coordinates to investigate: the angular distribution of the near-elastic electrons, or the electron momentum spectrum at fixed angles. In the end, some knowledge of both of these is desired. However, it was chosen to primarily investigate the momentum spectrum: the shape of the radiative tail. This is a better choice in part because shape of the radiative tail is a direct probe of the radiative corrections. Furthermore, at high precision ($<1\%$), its shape can provide information into the validity of different models of radiative

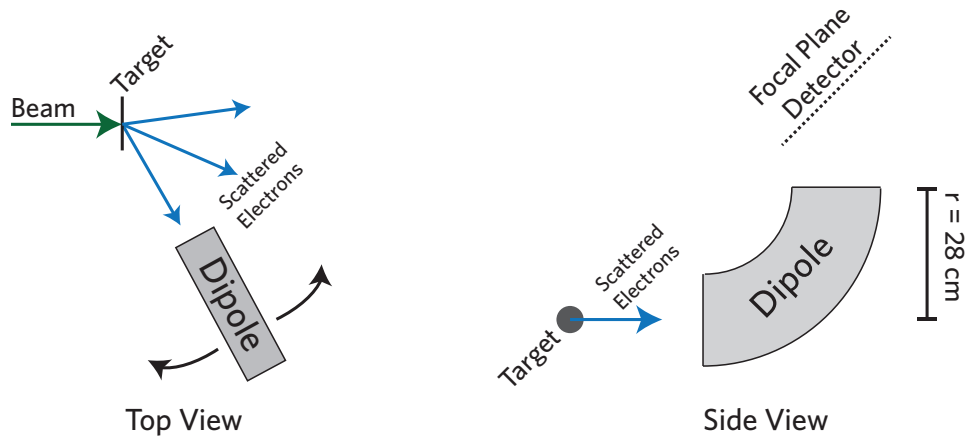


Figure 4-1: Initial schematic of the experiment layout.

corrections: exponentiated versus non-exponentiated, for example.

A focusing magnetic spectrometer is an effective way to measure a momentum spectrum. Table 4.1 shows the initial goals that were set out when designing the spectrometer. The main functions of the spectrometer are to provide dispersion in momentum, and to focus point-to-point in angle. The focal plane denotes the location at which the momentum dispersion is approximately linear, and to which the electron ϕ -coordinate is focused. Figure 4-2 shows a schematic of the ϕ -angle focusing and momentum dispersion in the spectrometer. The position of the focal plane, h and α can be calculated to first-order by the expressions [25]:

$$h = \frac{r^2}{d} \quad (4.1)$$

$$\alpha = \arctan \left(1 + \frac{d-r}{2r} \right).$$

This is, of course, an approximation. A complete field simulation was performed in Ansys Maxwell and later incorporated into a Geant4 simulation in order to more-precisely quantify the dispersion. In the end, the hit pattern at the focal plane draws out a two-dimensional rectangle, with coordinates of electron momentum and θ (scattering angle). The detector is placed at this location, in order to record this.

4.1.2 Considerations for Luminosity Monitoring

An attempt to directly measure Møller scattering, a standard luminosity-monitoring process, leads to an interesting dilemma. An absolute measurement of the cross-

Table 4.1: Initial Detector Design Goals

Detectors	One dipole spectrometer + readout at focal plane
Dipole radius	28 cm
Dipole angle	90°
Radial distance to detector	60 cm
Momentum acceptance	$\Delta p/p \sim 10\%$
Momentum resolution	$\delta p/p \sim 10^{-3}$
θ acceptance	$\pm 0.5^\circ$
ϕ acceptance	1°
Signal Angles	25° to 45° (in 5° steps)
Signal electron momentum	0.9–2.1 MeV/c
Signal detector field	100–250 Gauss

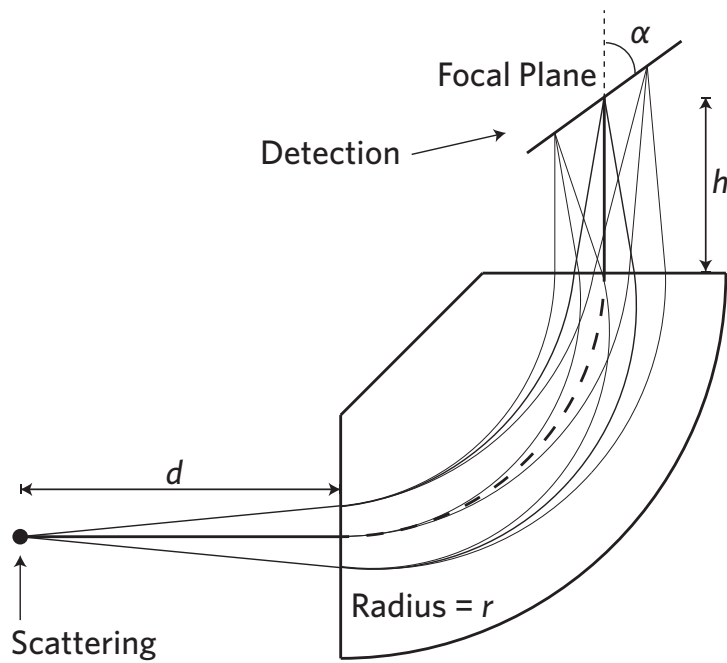


Figure 4-2: Schematic of distances and angles in the focusing spectrometer.

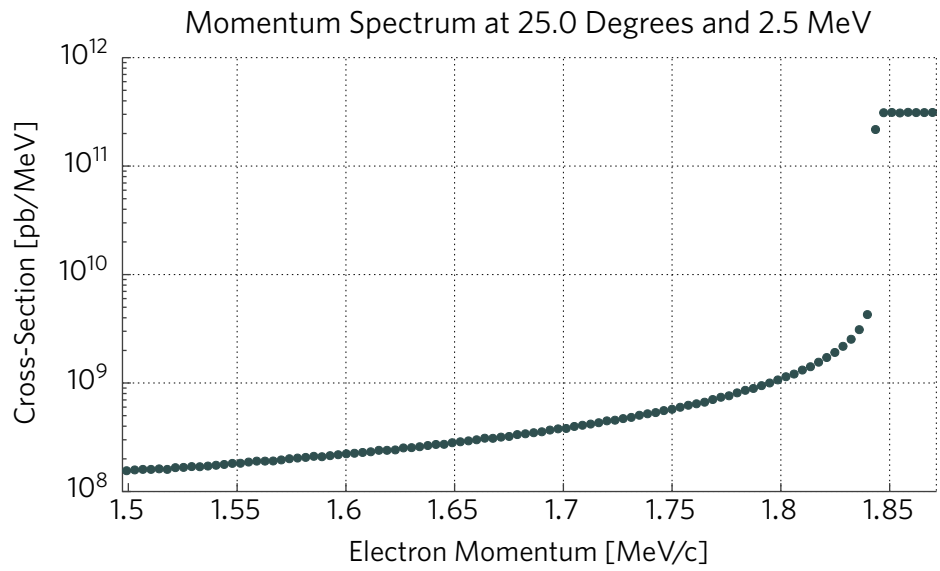


Figure 4-3: Raw Møller momentum spectrum at 25°, integrated over ±0.5°, for a 2.5 MeV beam.

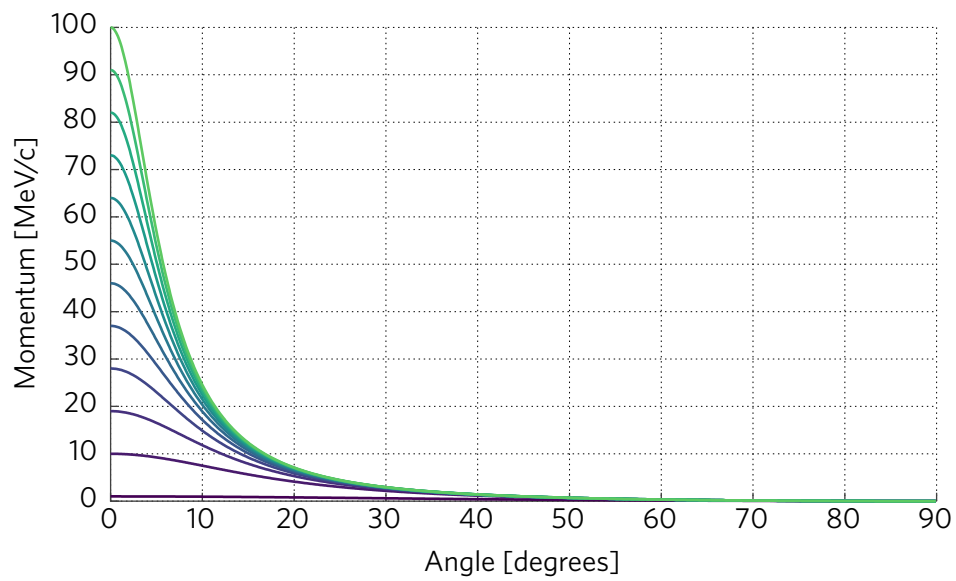


Figure 4-4: Scattered Møller electron energy as a function of angle, for beam energies ranging from 1–100 MeV.

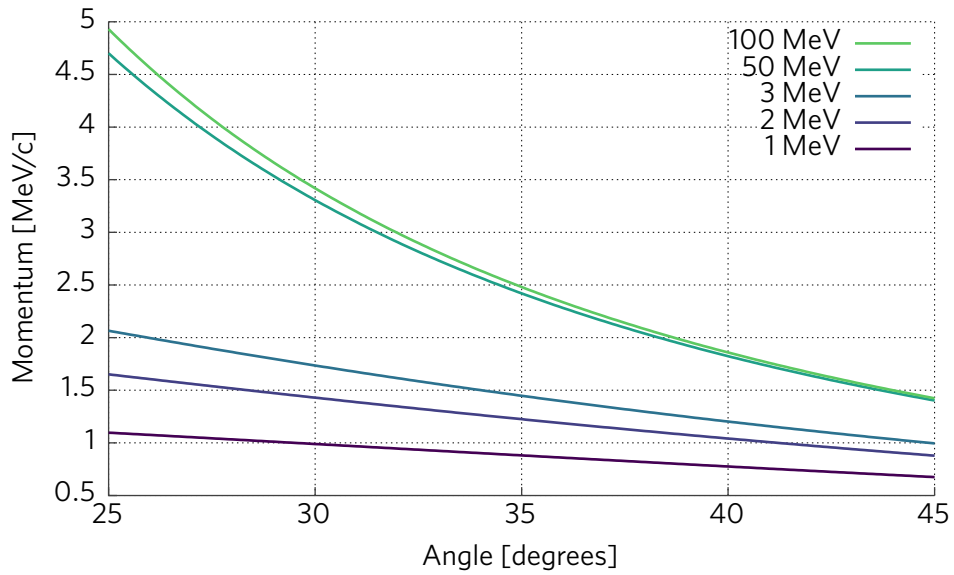


Figure 4-5: Scattered Møller electron momentum as a function of angle (in the spectrometer’s range), for selected beam energies.

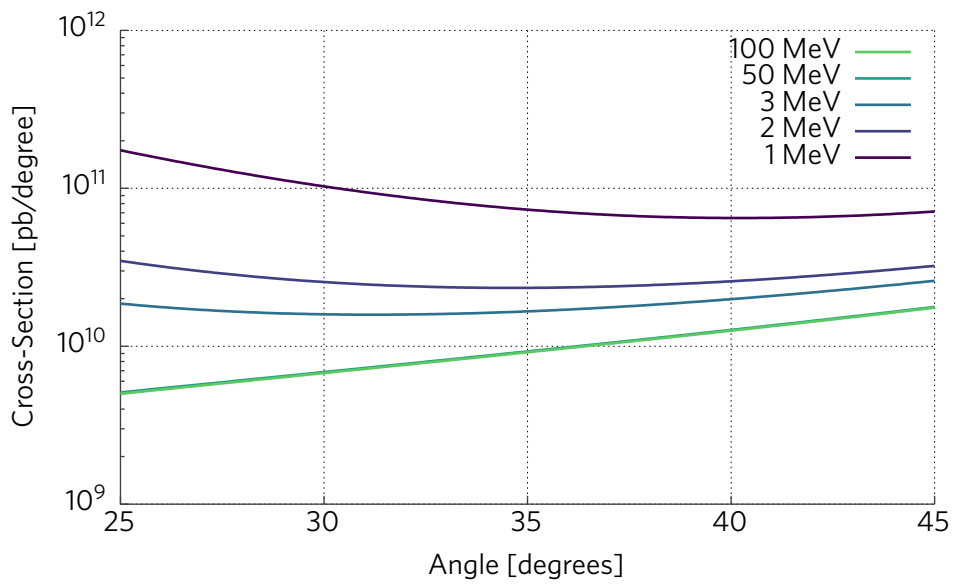


Figure 4-6: Differential Møller cross-section as a function of angle (in the spectrometer’s range), for selected beam energies.

section will be limited, in part, by knowledge of the luminosity. Given that Møller scattering is typically the best-known process in a detector to begin with, this becomes an issue: the remaining normalization processes are all less well-understood. Additionally, many existing experiments measuring these processes have used Møller scattering for normalization, rendering their results unhelpful.

An effective way to combat this is to design an experiment that normalizes one part of the radiative Møller spectrum to another, thus reducing the importance of knowing the precise luminosity. There are two main methods of achieving this. One is to sweep the detector's acceptance across the interesting region very slowly so that consecutive windows cover an overlapping region of parameter-space. The other is to use a relative luminosity monitor, with the requirement that it be exactly the same for every setting. A second spectrometer was initially planned for this; however in the end, a Faraday Cup was used (§4.8.1).

4.1.3 Continuous versus Discrete Angles

The main spectrometer must be capable of analyzing different scattering angles. However, a choice had to be made as to whether it should be able to measure a continuous range of angles, or a set of discrete ones. In the end it was decided to place the spectrometer on an arc-shaped track, with pins to lock it at different positions.

The decision to pursue discrete angles over continuous ones stemmed from the desire to know the scattering angle to $\sim 0.1^\circ$. It is difficult and time-consuming to repeatedly survey a continuously-rotating spectrometer to high precision. However, with locking positions, the spectrometer can be moved between specified angles with extremely good repeatability (differences undetectable with optical equipment sensitive to $\sim 10 \mu\text{m}$). This allows the setup to be precisely surveyed once in place, and then the detector can easily be set in any position to take more data.

Additionally, a primary experimental goal was identified as measuring as much of the radiative tail to as high a precision as possible. Therefore, it was less of a priority to measure a large range of angles, and more important to characterize the momentum spectrum. The locking rotation mount was thus an important simplification with little experimental cost.

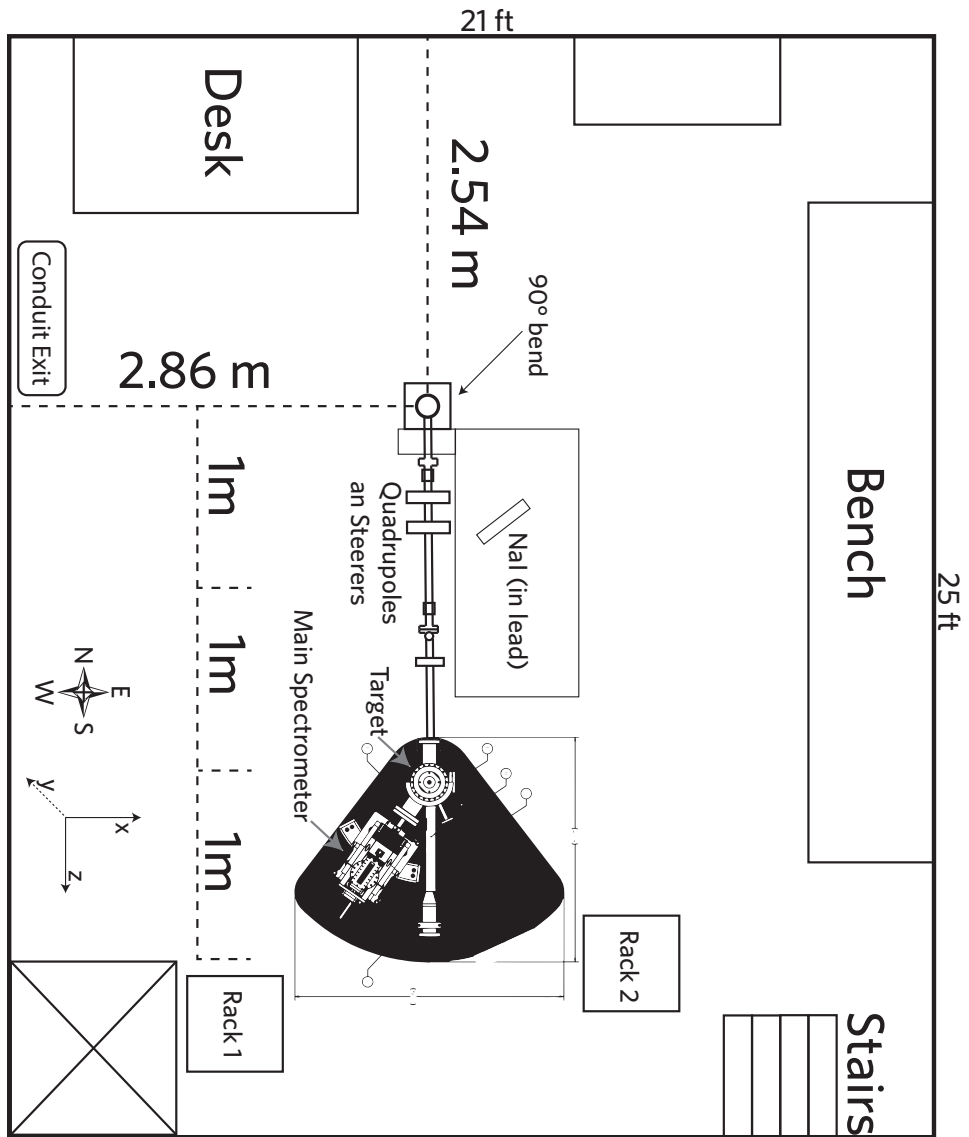


Figure 4-7: Layout of the installation at the HVRL.

4.2 Experimental Design

The experimental apparatus was designed and fabricated at the MIT Bates Research and Engineering Center. The design consists of two spectrometer arms; however, only the moving arm was used at the HVRL (Fig. 4-7). The moving arm consists of a 28 cm 90° bending dipole magnet and a scintillating tile focal-plane detector (Figs. 4-22, 4-13, 4-23). A tungsten collimator defines a square 1° × 1° acceptance (Fig. 4-8). The magnet moves along a track (Fig. 4-15), and locks into place at nine positions between 25° and 45° (Fig. 4-14). When the experiment was run, however, the spectrometer was kept in the range of 30° to 40° degrees to avoid placing undue stress on the bellows.

The entire system is held under vacuum in order to minimize multiple scattering of the low-energy electrons. A flexible bellows facilitates this (Figs. 4-9, 4-10, 4-11). The electrons exit the internal vacuum chamber (Fig. 4-21) through a Kapton window a few centimeters from the focal plane (Figs. 4-12, 4-19). The main spectrometer magnet is a “C”-magnet design, with an additional Kapton window at the back of the magnet. This allows higher-energy elastics to escape the system during Møller measurements, without producing too much background (Figs. 4-20, 4-16),

The available targets are 2 μm and 5 μm diamond-like carbon foils from MicroMatter. These are mounted on a ladder which re-uses the positioning mechanism of the DarkLight 2012 beam test [26] (Fig. 4-17). MicroMatter produces the foils by laser plasma ablation deposition. A laser evaporates carbon from a sputter target, creating nanoparticles which are deposited onto a substrate [27]. A 1 μm foil was initially mounted, but it disintegrated during installation.

4.3 Estimation of Target Foil Heating

It is important that the electron beam does not heat up the carbon foil to the point where it burns a hole. Here, this heating is estimated. It is assumed that the foil is in vacuum, and therefore only radiative heat losses are calculated. In reality, there will be additional heat transfer out through the metal fitting holding the foil, so these figures are an overestimate of the resulting temperature. In the end, a foil temperature distribution is sought as a function of radius. We also assume the beam is Gaussian distributed according to: $\exp(-r^2/r_0^2)$ (nominal $r_0 = 0.1$ mm).

The method consists of dividing each foil up into circular shells (Fig. 4-24). Each shell receives energy from:

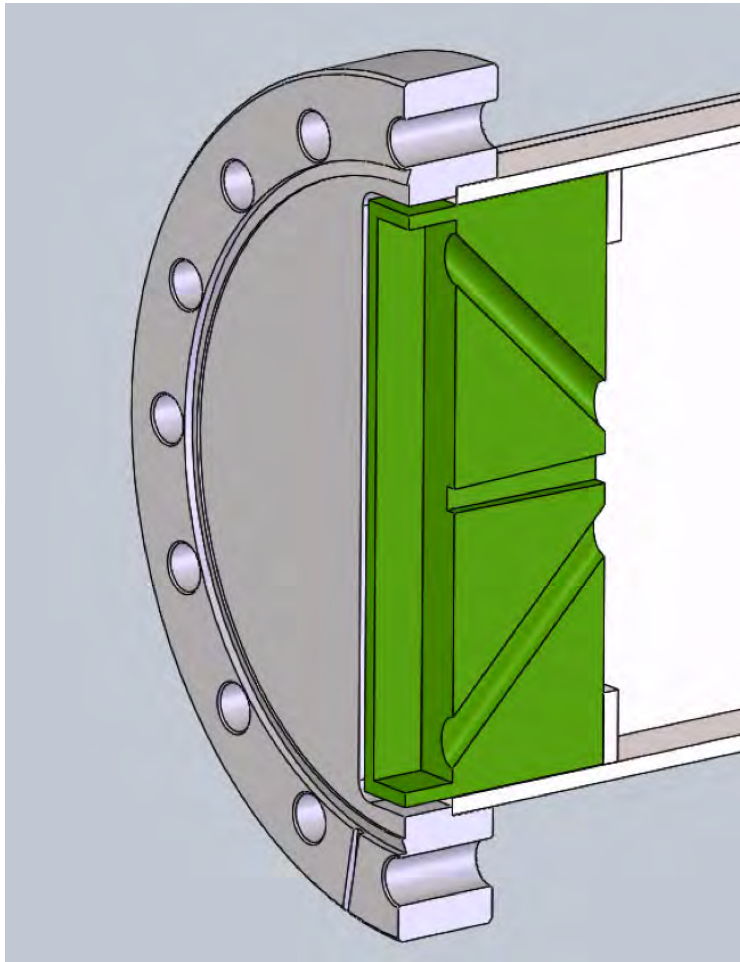


Figure 4-8: Cutaway view of the tungsten collimator. The center rectangular aperture defines the acceptance, and the two rotated holes provide additional conductance to allow the vacuum to equalize.

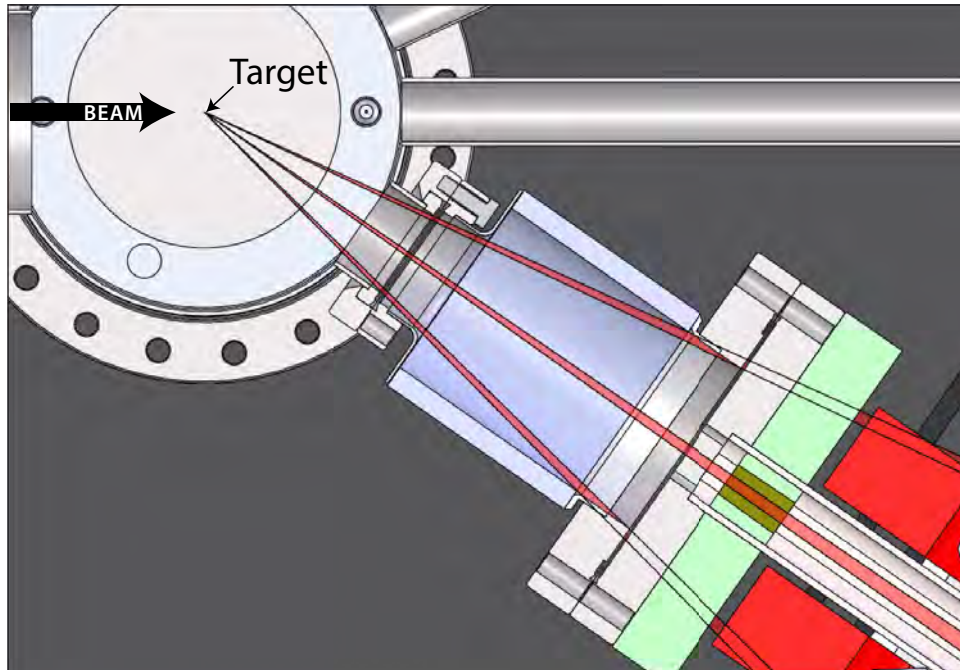


Figure 4-9: Bellows at the nominal 35° angle.

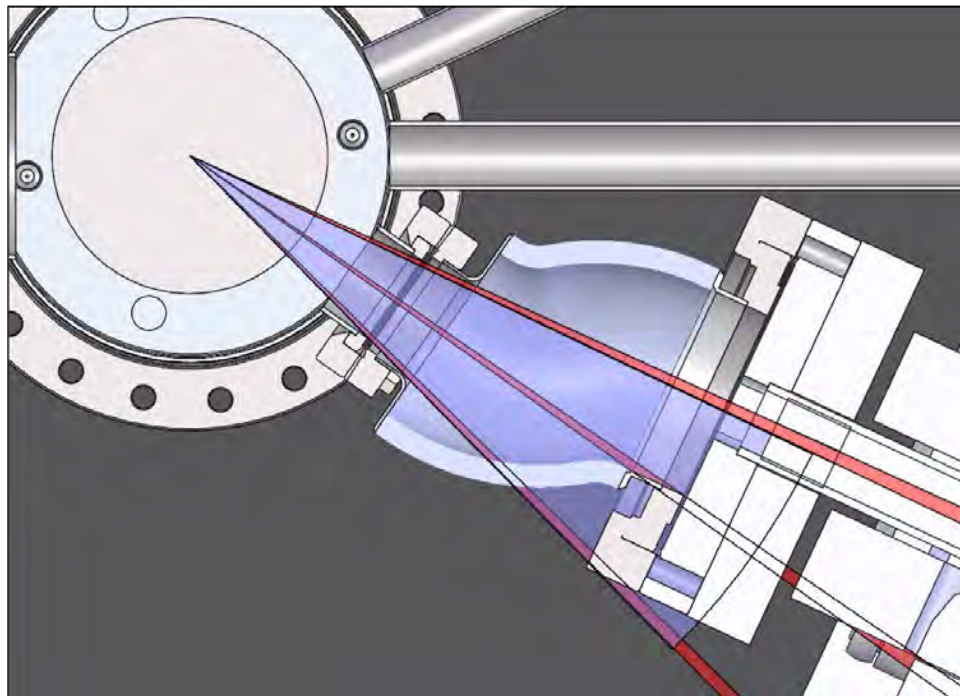


Figure 4-10: Bellows when the spectrometer is moved to 25°.

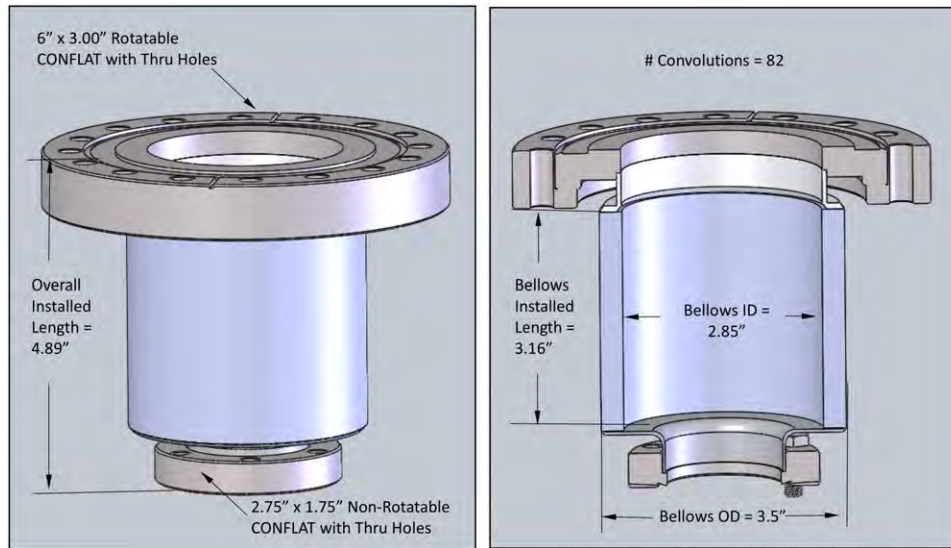


Figure 4-11: Drawing of the bellows, including dimensions.

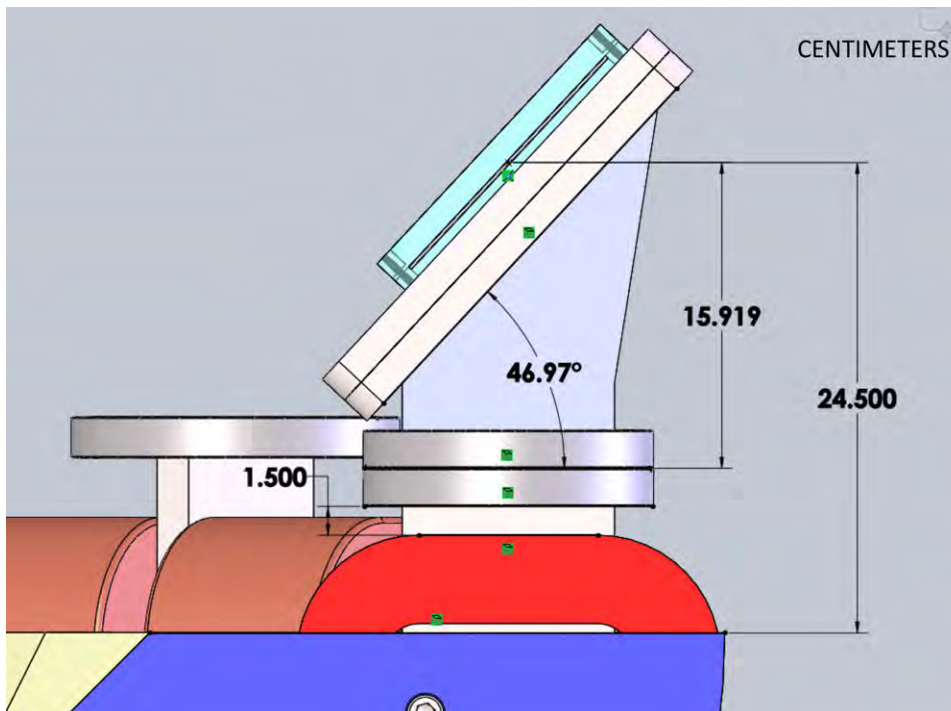


Figure 4-12: Angle and position of the focal-plane exit window.

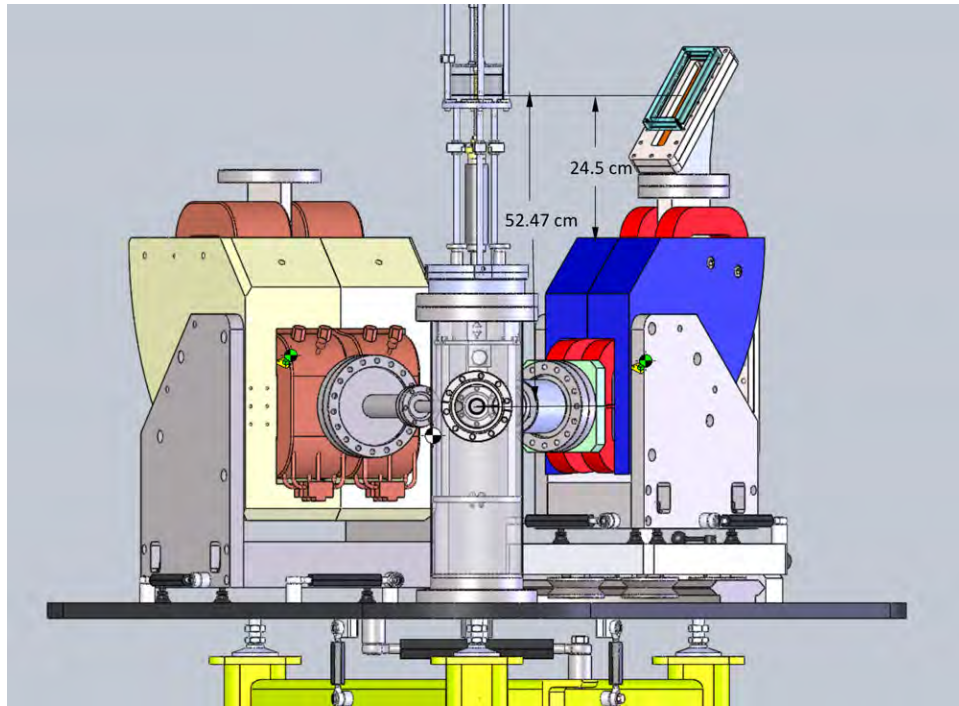


Figure 4-13: Front view of the experiment apparatus.

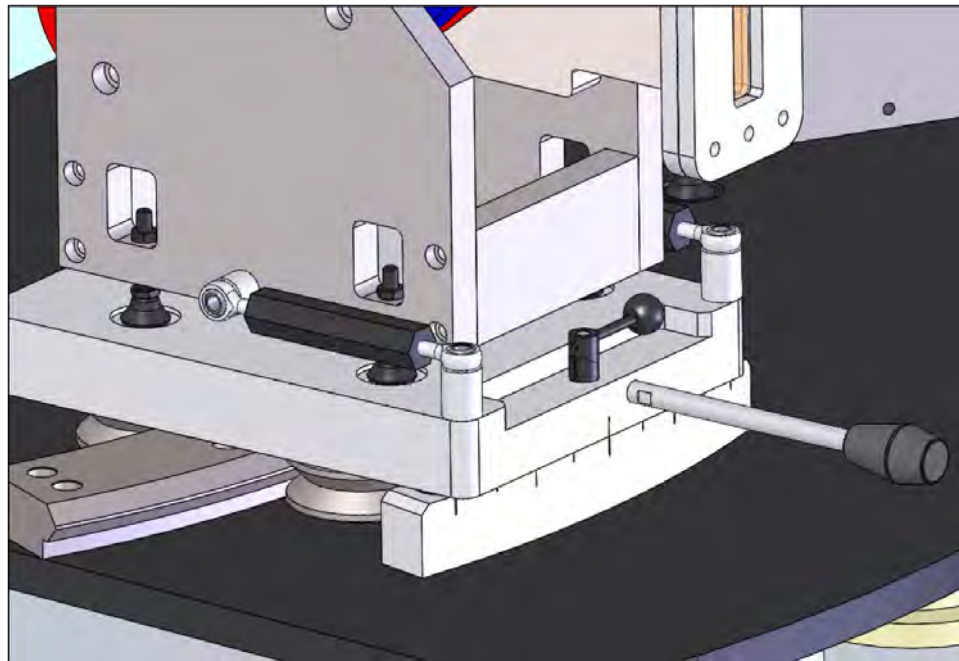


Figure 4-14: Locking pin system used to select the spectrometer angle.

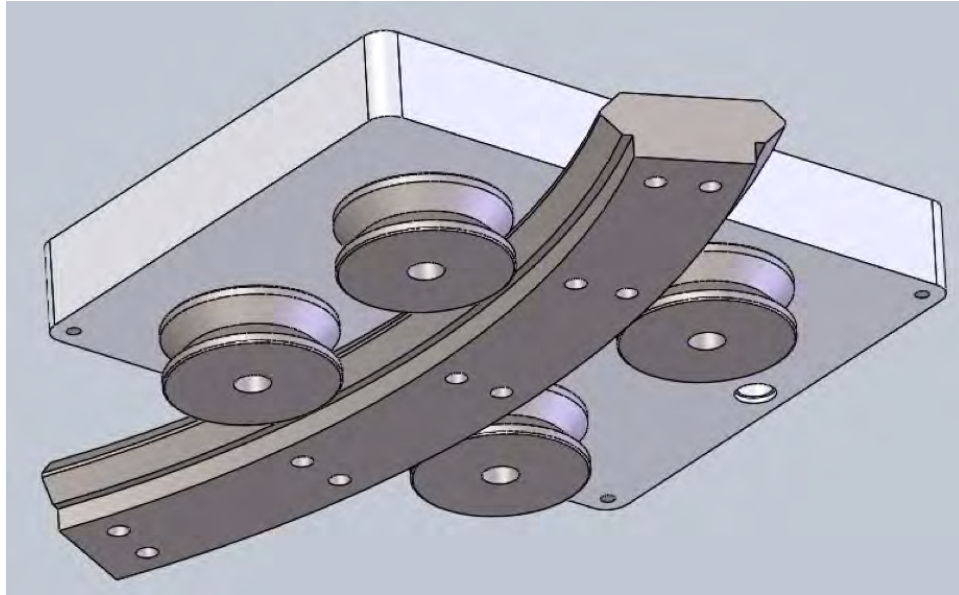


Figure 4-15: The rolling apparatus used to allow movement of the main spectrometer (view from below).

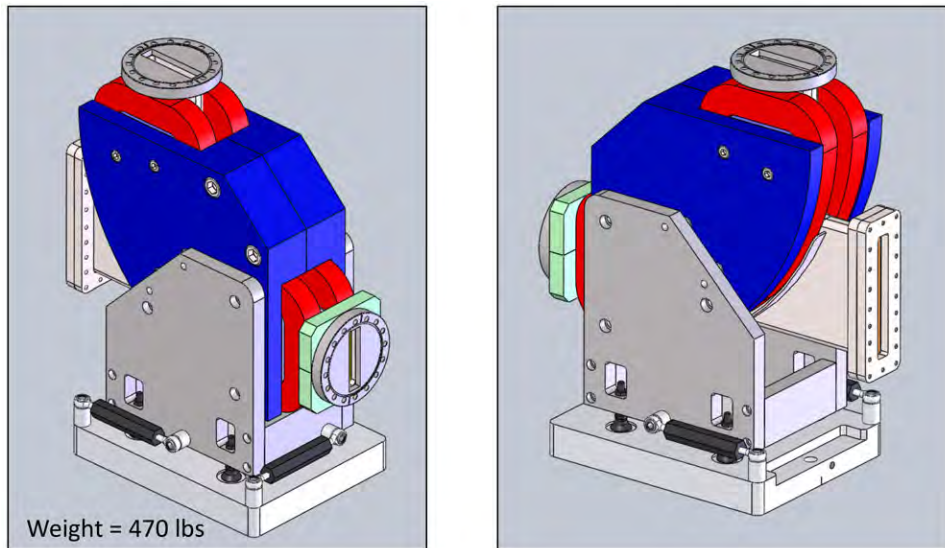


Figure 4-16: Drawing of the full spectrometer apparatus.

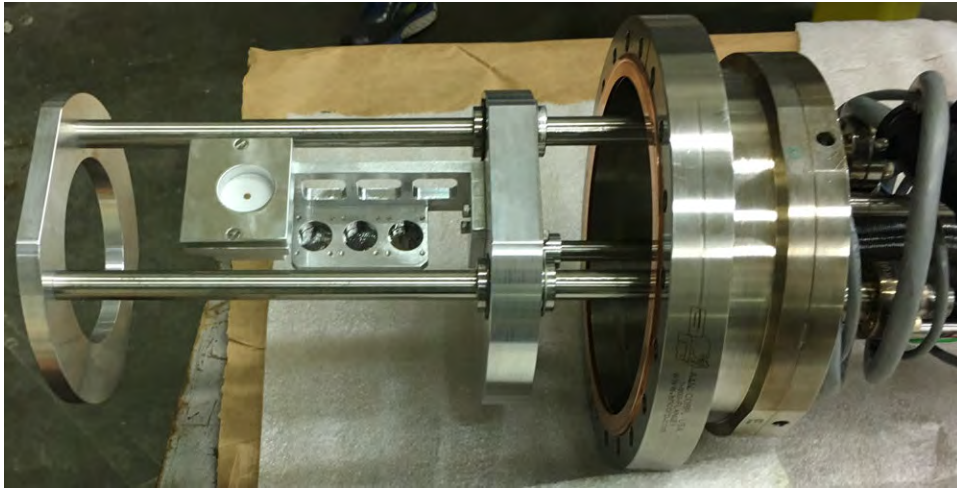


Figure 4-17: The target ladder apparatus.

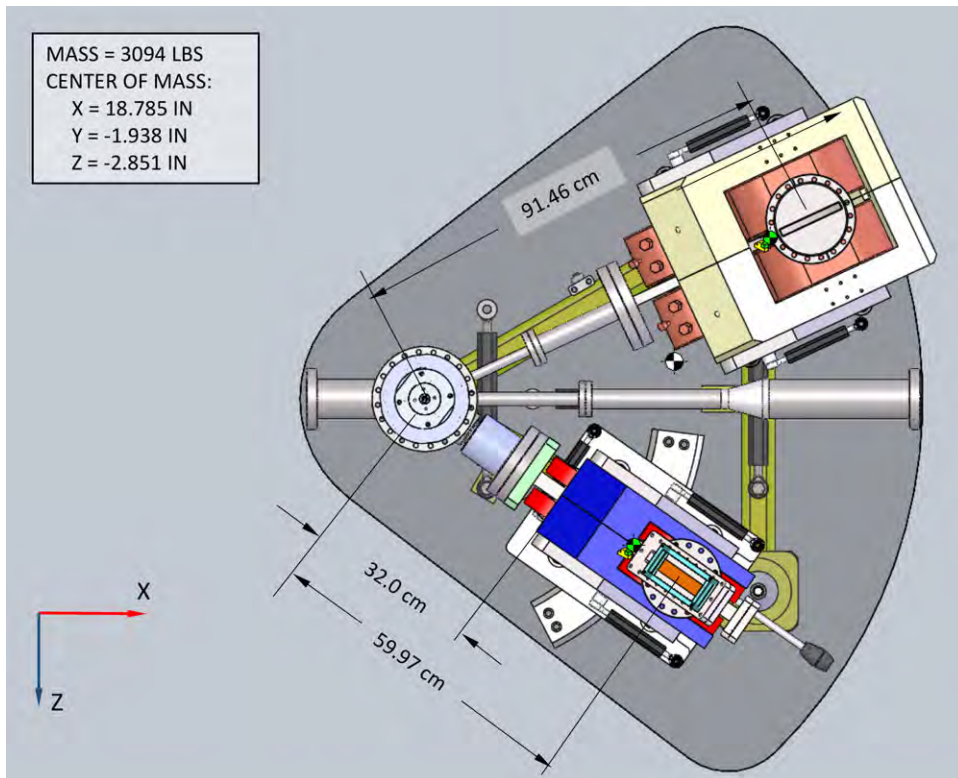


Figure 4-18: Top view drawing of the apparatus

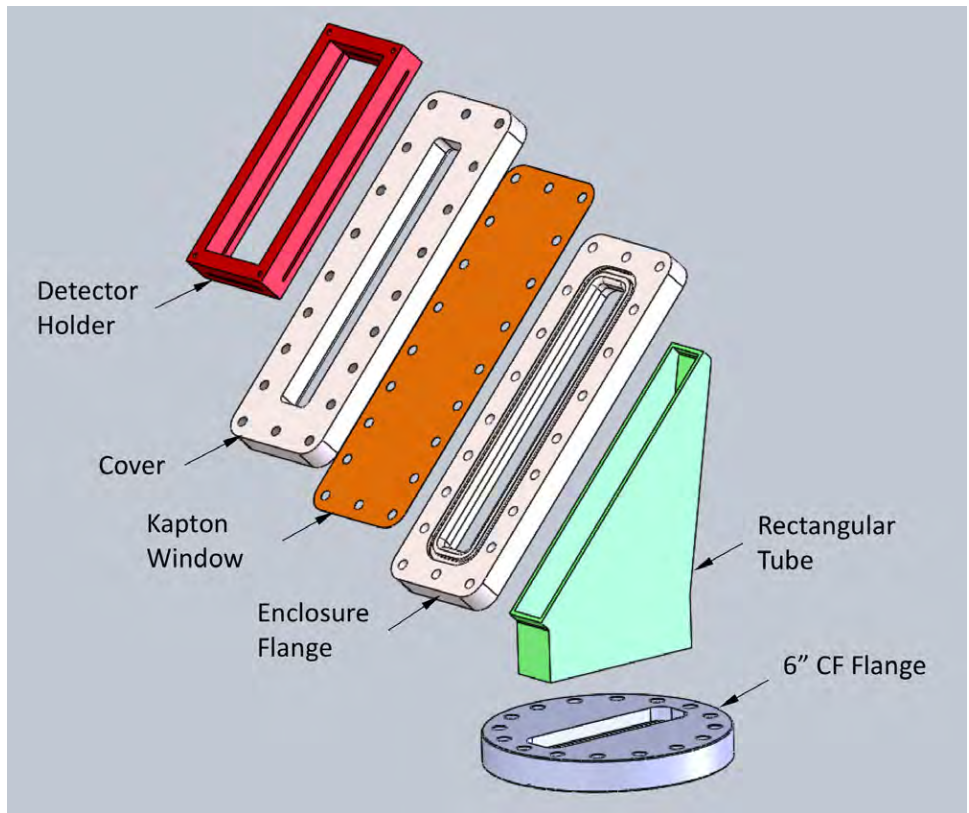


Figure 4-19: Kapton window assembly adjacent to the focal plane.

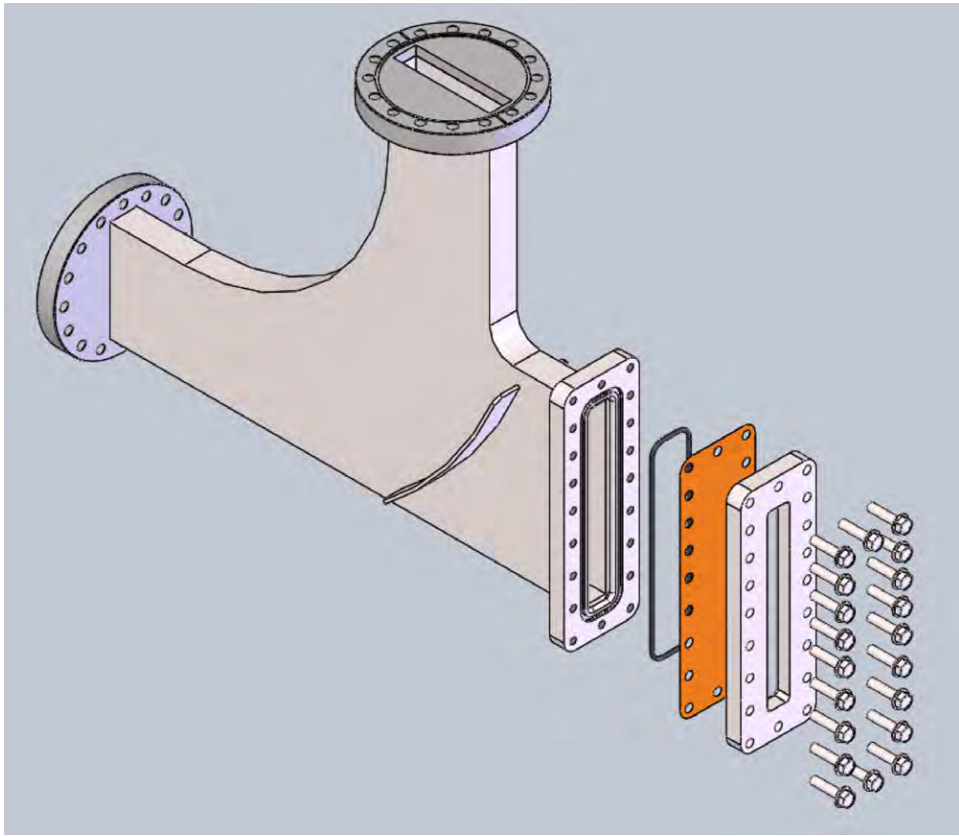


Figure 4-20: Kapton window assembly at the rear of the spectrometer.

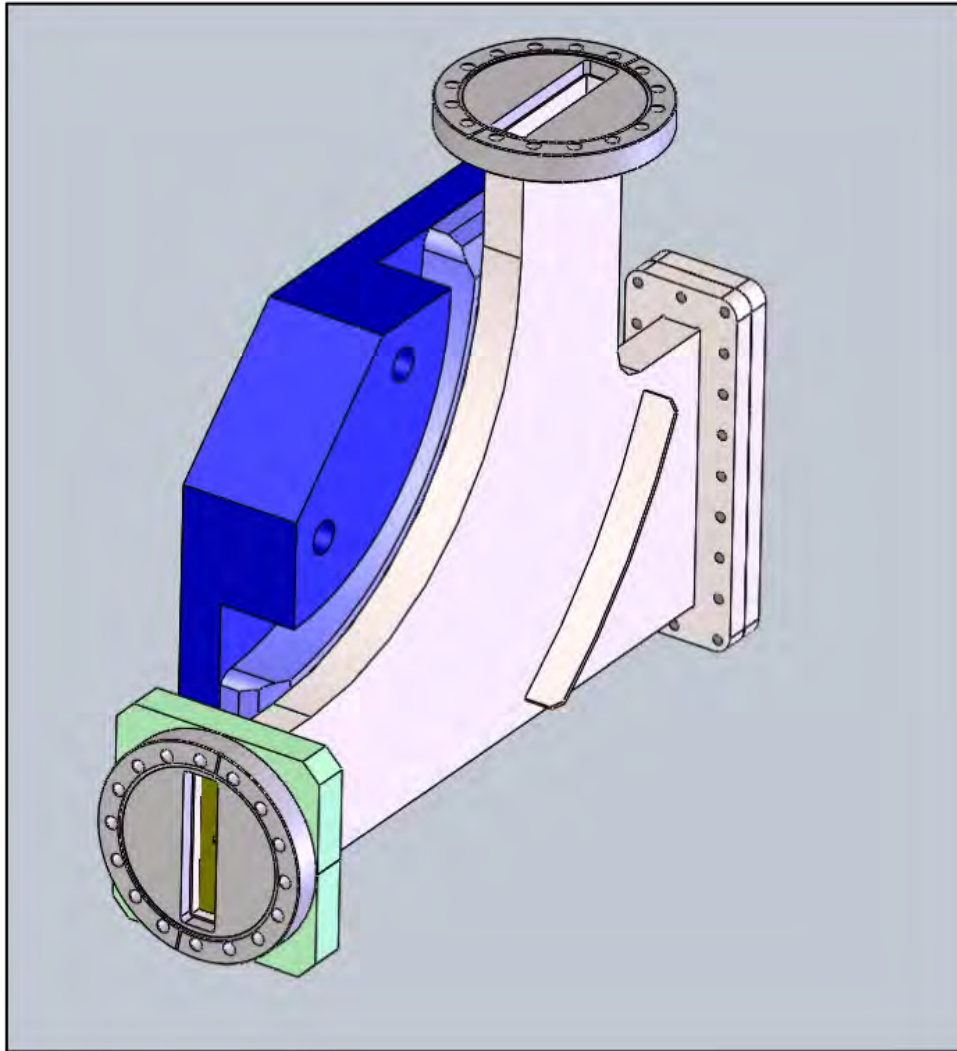


Figure 4-21: Cutaway view of the spectrometer magnet, showing the internal vacuum chamber.

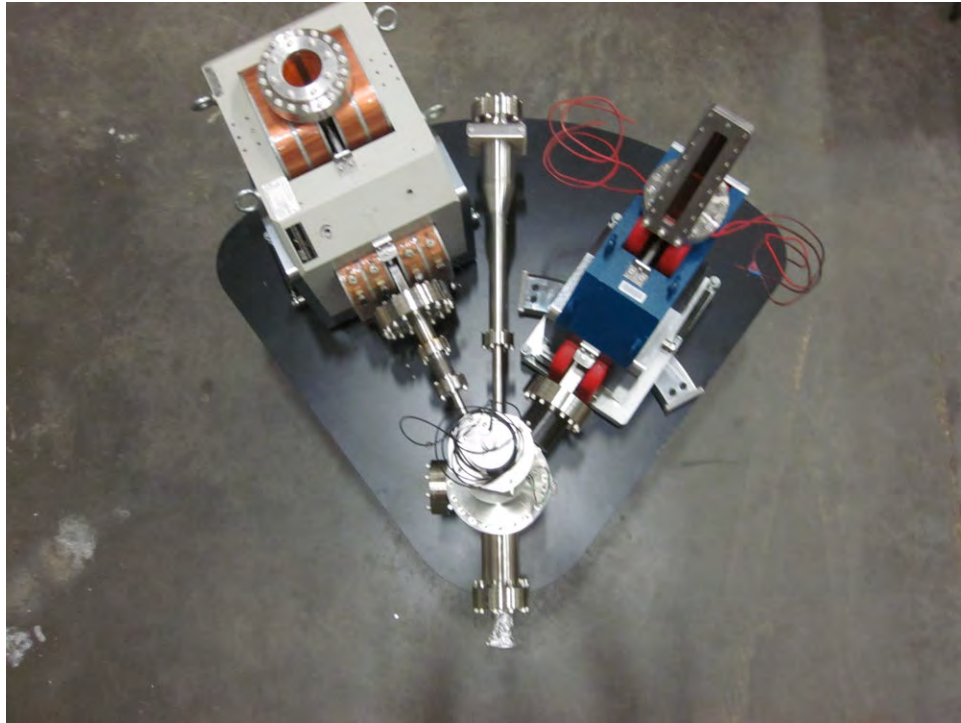


Figure 4-22: Top view of the apparatus, including the original fixed luminosity arm (left).

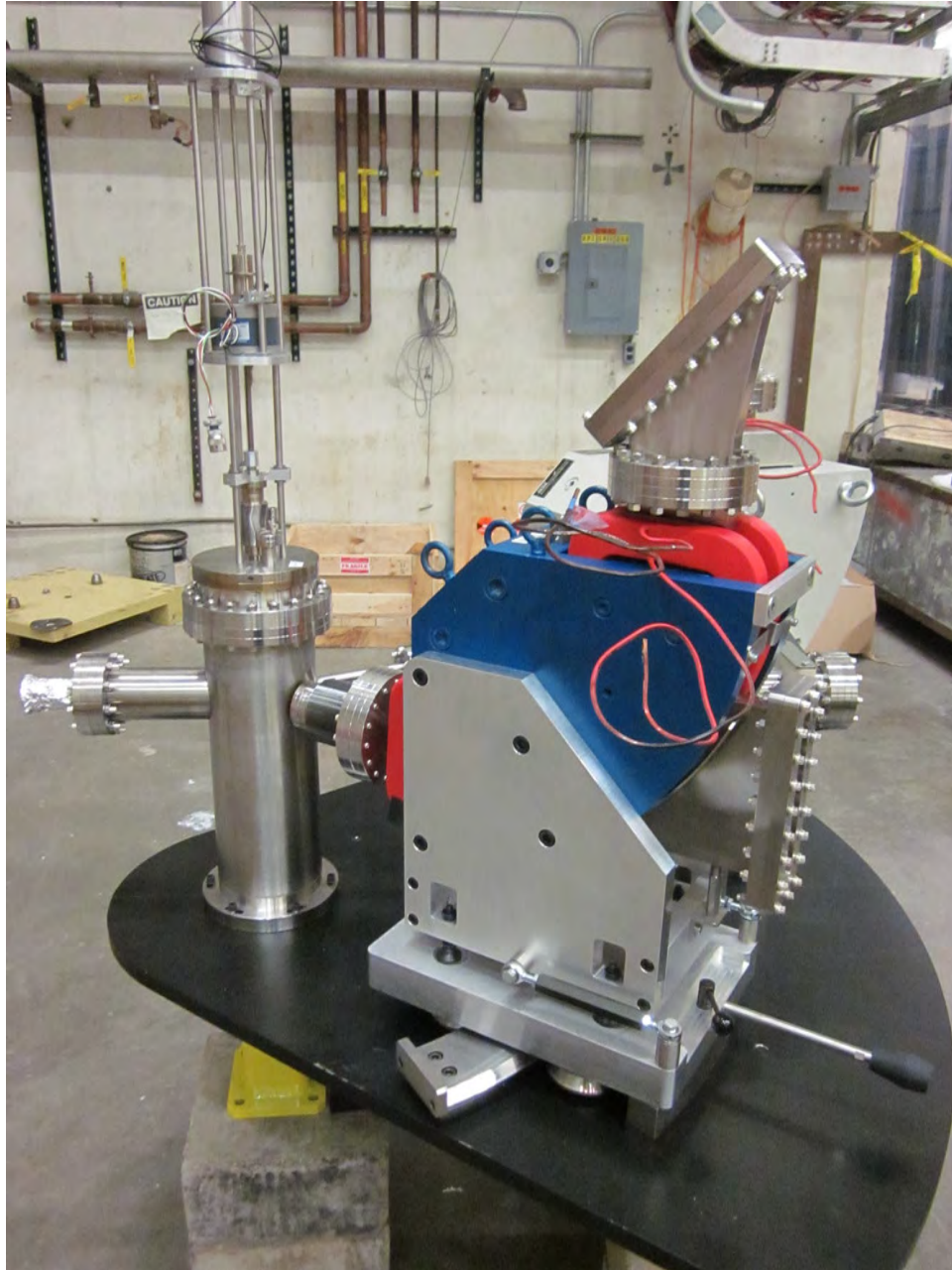


Figure 4-23: The moving spectrometer arm.

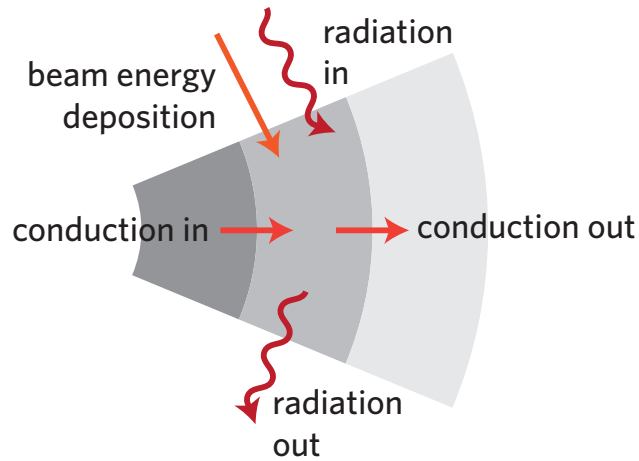


Figure 4-24: Diagram of heat transfer in the foil.

- Power conducted in from last shell
- Power deposited from beam
- Ambient radiation absorbed

The shells lose energy via thermal radiation, and by conducting power to the next shell. In equilibrium, the total absorbed power equals the total radiated power. Considering power transfer from one shell to the next gives ΔT :

$$P = 2\pi\lambda t \frac{\Delta T}{\ln r_2/r_1}.$$

Conserving energy yields the radiation, which then provides an absolute T .

The environment is approximated as a 300 K blackbody. At the center of a spherical 300 K blackbody, the radiant flux $P/A = \sigma T_{env}^4$. Therefore the energy absorbed in a differential area element of the foil is

$$dP = \epsilon_c \sigma T_{env}^4 dA,$$

and conversely, the re-radiated energy is

$$dP = \epsilon_c \sigma T_c^4 dA.$$

As indicated by NIST ESTAR [28], the stopping powers in carbon for a 3 MeV electron and a 100 MeV electron, respectively are 1.648 MeV cm²/g and 3.984 MeV cm²/g.

The results of the calculation are shown in the following figures. Here, temperature distributions are shown for a 5 μ m target in a 1.0 μ A 3 MeV beam

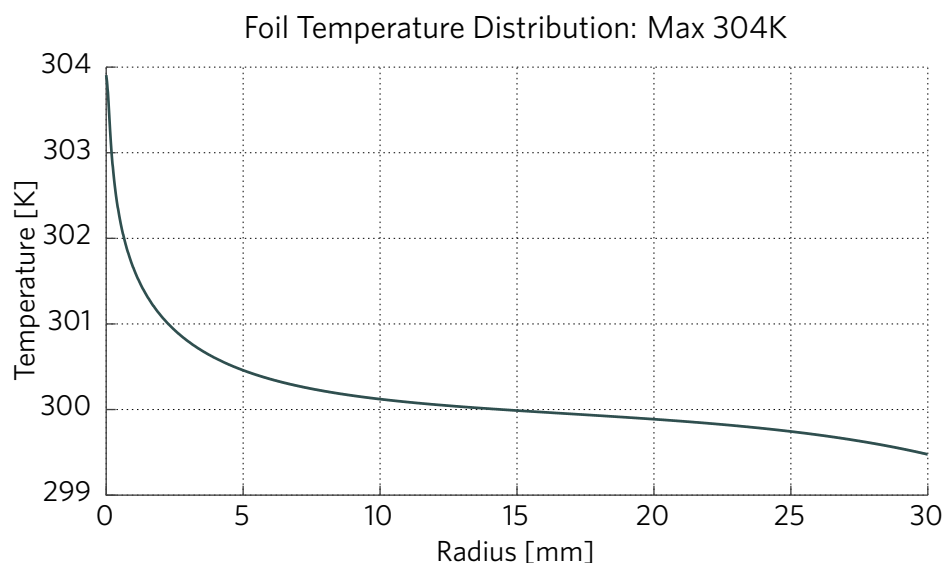


Figure 4-25: 5 μm target, 3 MeV, 1.0 μA beam with 0.1 mm radius.

(Fig. 4-25), a 10.0 μA 3 MeV beam (Fig. 4-26), a 1.0 μA 100 MeV beam (Fig. 4-27), and a 10.0 μA 100 MeV beam (Fig. 4-28). For a 3 MeV beam, the hottest point at 10.0 μA is 339 K, only 39° above the specified room temperature. This indicates that foil heating should not be a significant problem.

4.4 Considerations on Overall Precision

In an ideal world, with very low beam emittance and no multiple scattering effects, a precision measurement of the shape of the radiative tail can be made. However, as was later seen, this is not an accurate description of the environment at the HVRL. Prior to this realization, a study was performed in order to understand how well the beam energy and scattering angle must be known, if a one-percent measurement were to be made in an ideal world. The following sections describe the results of this study.

To this end, the radiative generator was used to calculate the Møller electron momentum spectrum at various settings near 25° and 2.5 MeV. The nominal spectrum is shown in Fig. 4-3. This, and all other radiative spectra shown here, are integrated over 1°, e.g. from 24.5° to 25.5°. This mimics the spectrometer's acceptance. The error bars on the plots in this section represent Monte Carlo simulation uncertainties.

Slight perturbations in this spectrum are hard to see, so ratios are plotted instead. For these ratios, the x -axes of the spectra are first aligned, with the

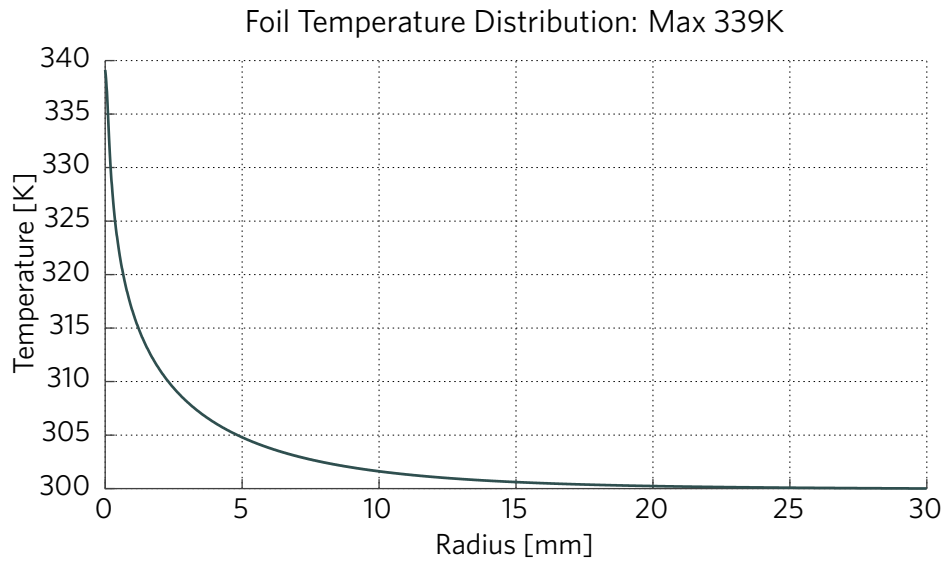


Figure 4-26: 5 μm target, 3 MeV, 10.0 μA beam with 0.1 mm radius.

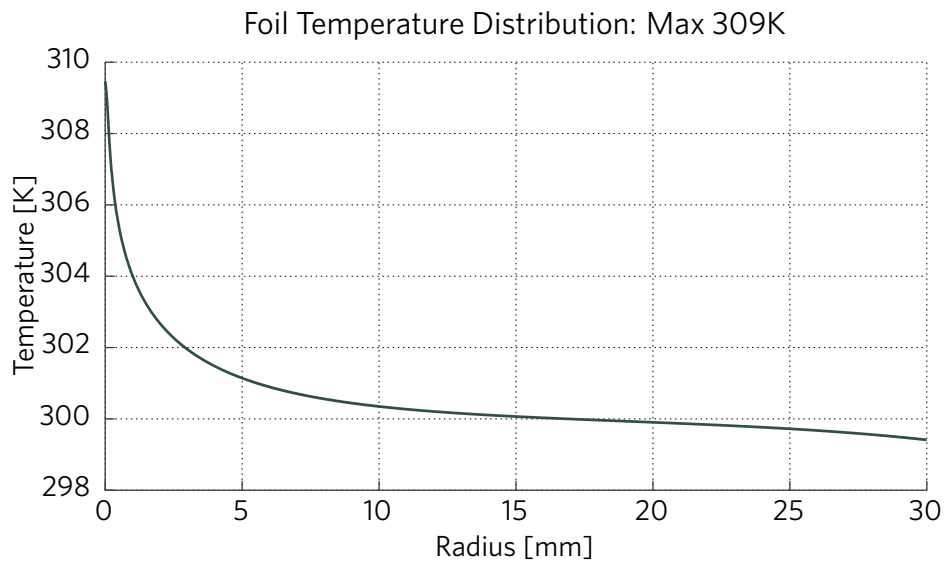


Figure 4-27: 5 μm target, 100 MeV, 1.0 μA beam with 0.1 mm radius.

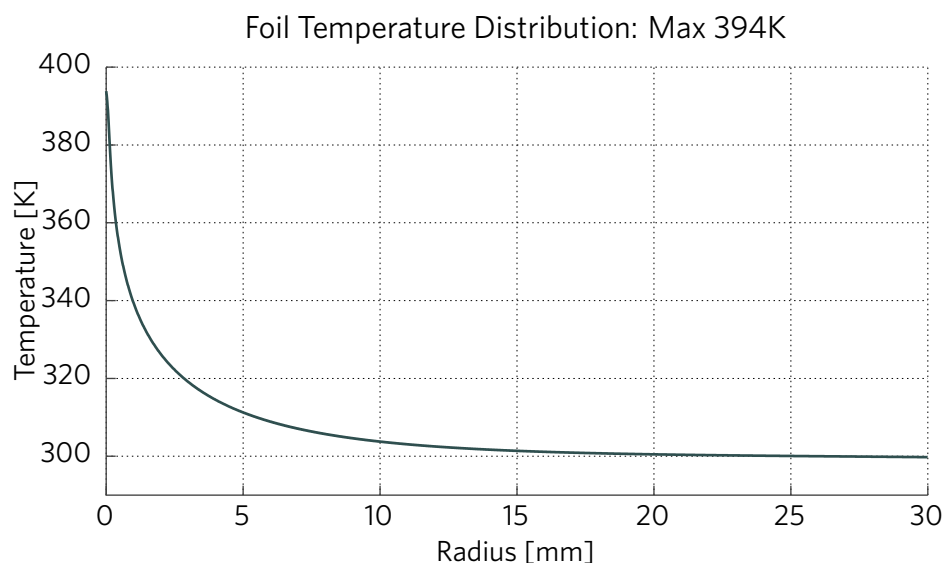


Figure 4-28: 5 μm target, 100 MeV, 10.0 μA beam with 0.1 mm radius.

electron momentum now represented as a percentage of the non-radiative momentum. This approximates what would happen in a measurement if the actual momentum were unknown, and the spectra were scaled to the closest simulation.

Figure 4-29 shows the effects of changing the beam kinetic energy by ± 100 keV. The lower (2.4 MeV) and upper (2.6 MeV) parameters are simulated separately, and their ratio to the nominal spectrum (2.5 MeV) is shown. Here, an approximately 5–10% effect is seen. For a $\sim 1\%$ measurement, it follows that the beam energy should be known to 10–20 keV. Figure 4-31 confirms the expected behavior when the beam is varied by only 10 keV.

Figure 4-30 shows the effects of changing the scattering angle by $\pm 0.1^\circ$. The lower (24.9°) and upper (25.1°) parameters are simulated separately, and their ratio to the nominal spectrum (25.0°) is shown. Here, a few-percent effect is seen.

4.5 Possible Measurement of the Beam Energy

The energy of 2.5 MeV electrons elastically-scattered off carbon is essentially independent of angle: to within tens of eV, it is equivalent to the beam energy. This facilitates an indirect measurement of the beam energy using the moving spectrometer. In addition, knowledge of the beam energy allows an absolute calibration of the magnet.

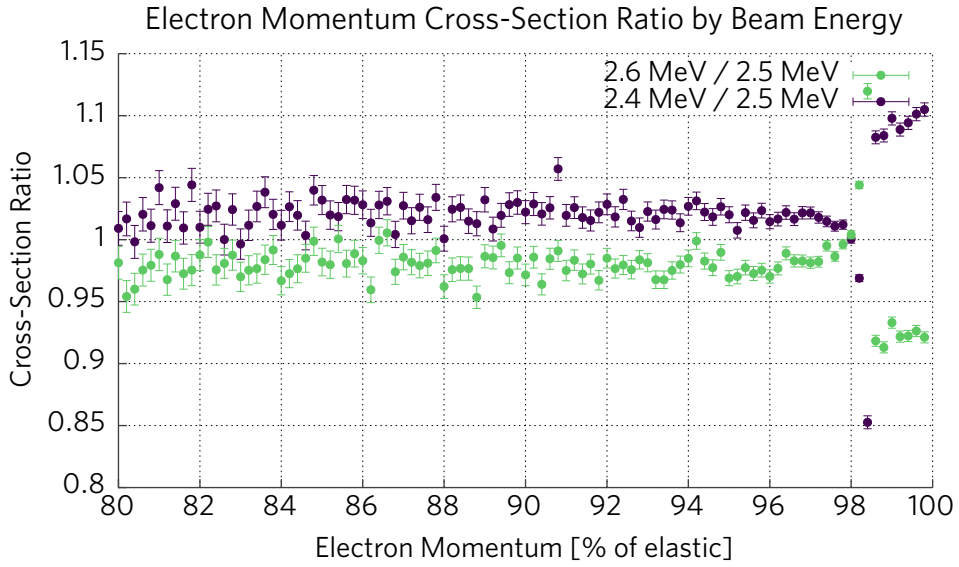


Figure 4-29: The radiative Møller spectrum for beam energies of 2.6 MeV and 2.4 MeV, divided by the spectrum at 2.5 MeV. This is for scattering at 25°. Note the approximately 10% effect in the near-elastic region.

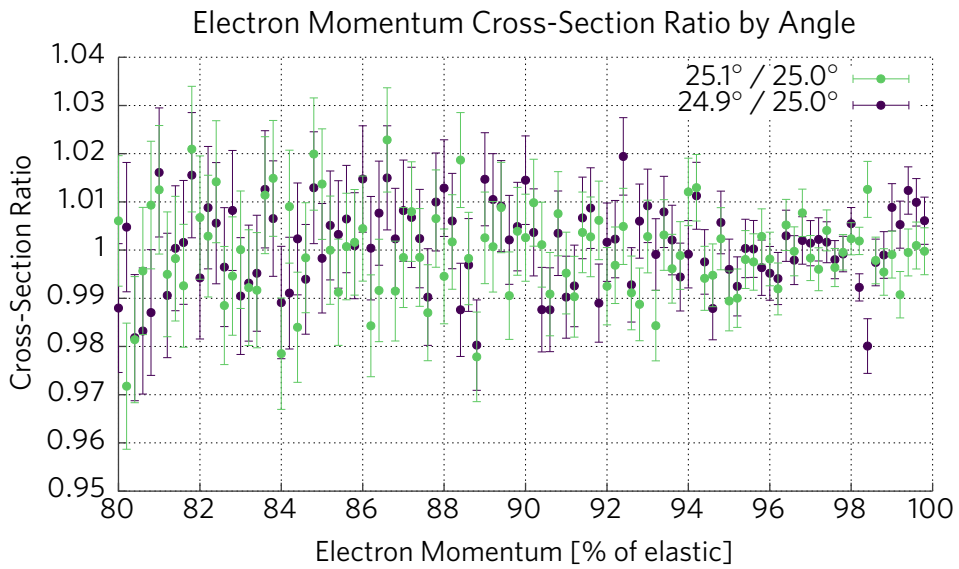


Figure 4-30: The radiative Møller spectrum at 25.1° and 24.9°, divided by the spectrum at 25.0°. This is for a 2.5 MeV beam.

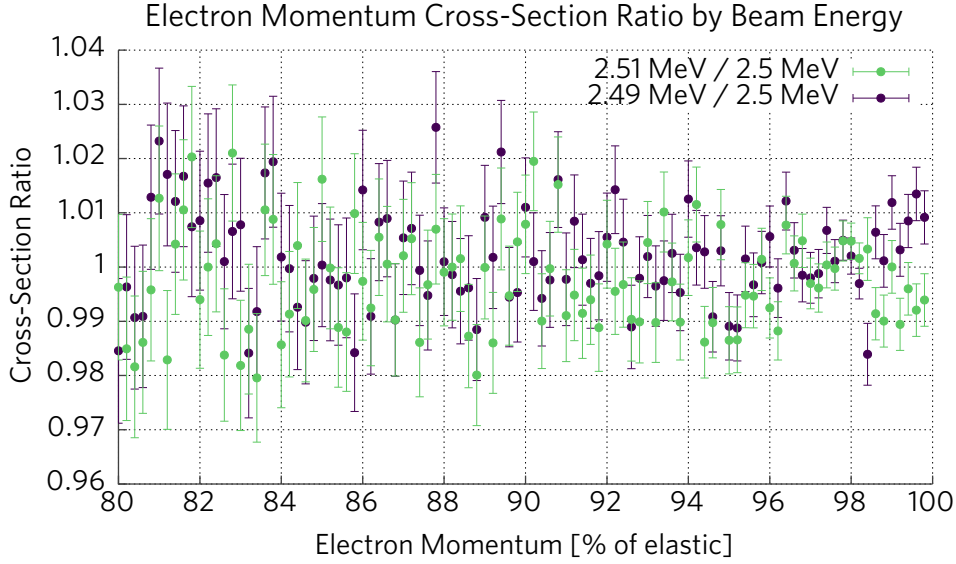


Figure 4-31: The radiative Møller spectrum for beam energies of 2.51 MeV and 2.49 MeV, divided by the spectrum at 2.5 MeV. This is for scattering at 25°.

Since the exact mapping of the magnet is not known, the best way to make this measurement is with a ratio. To illustrate this, we first define the magnet current that places the electron-carbon elastic line on the central trajectory as I_{eC} , and the Møller elastic line as I_{mol} . These are measurable quantities. Since the magnet current should be proportional to the momentum of the central trajectory, we can write:

$$\frac{I_{mol}}{I_{eC}} = \frac{P_{mol}}{P_{eC}}. \quad (4.2)$$

Then, since $P_{eC} \cong P_{beam}$,

$$\frac{I_{mol}}{I_{eC}} = \frac{P_{mol}}{P_{beam}} \equiv R \quad (4.3)$$

where we define the measured current ratio as R . Figure 4-32 shows this as a function of P_{beam} . We also note that $P_{mol} = P_{mol}(P_{beam}, \theta)$. Figure 4-34 shows this as a function of θ , and Fig. 4-36 as a function of beam energy.

The derivatives of the above quantities are shown in Figs. 4-33, 4-35, and 4-37, illustrating the high sensitivity of the Møller electron momentum to both the scattering angle and beam momentum. Clearly, inverting these to make an accurate measurement of P_{beam} requires precisely measuring both R and θ .

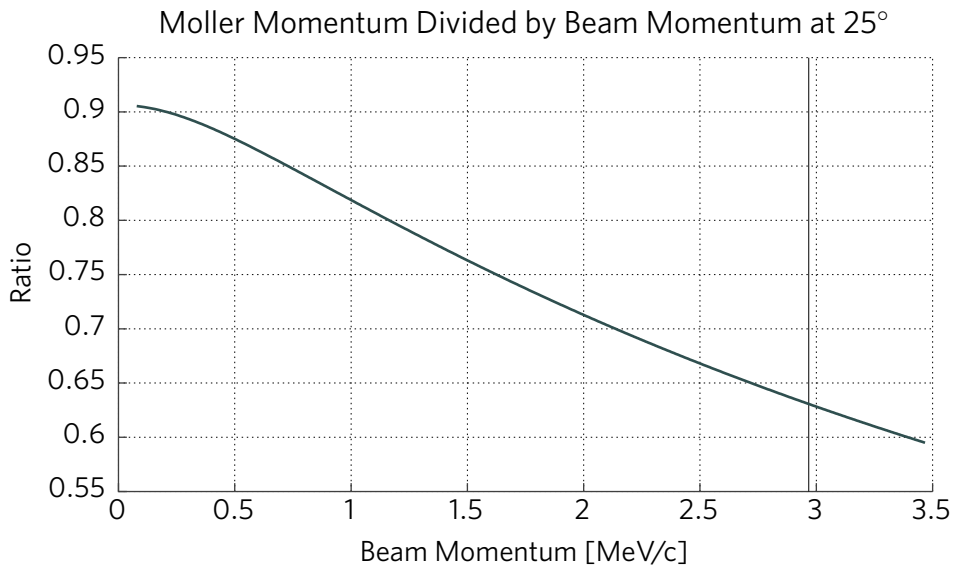


Figure 4-32: The ratio $P_{\text{mol}}/P_{\text{beam}}$ as a function of beam momentum. The beam momentum corresponding to $E_{\text{kinetic}} = 2.5$ MeV is marked.

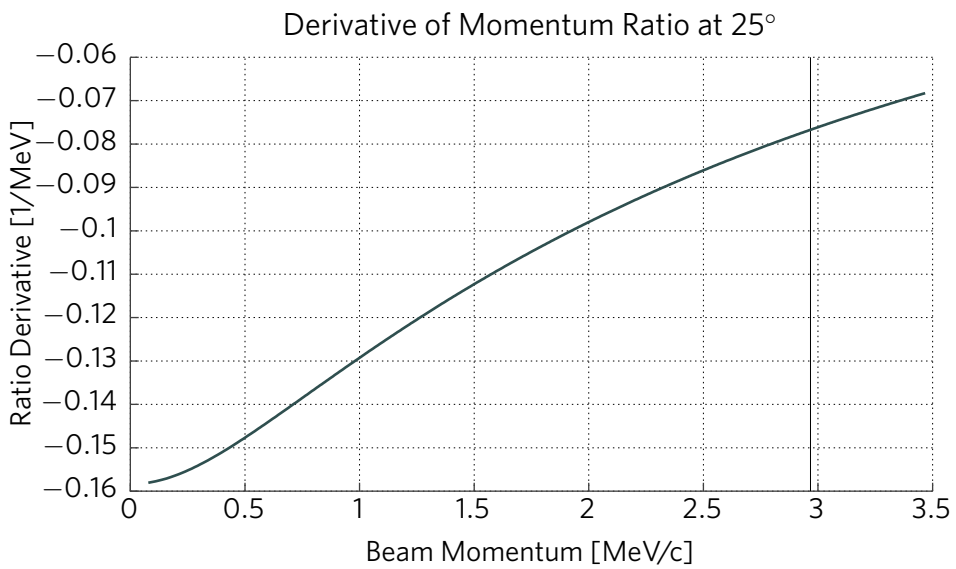


Figure 4-33: Derivative $\partial R/\partial P_{\text{beam}}$ as a function of P_{beam} . The beam momentum corresponding to $E_{\text{kinetic}} = 2.5$ MeV is marked.

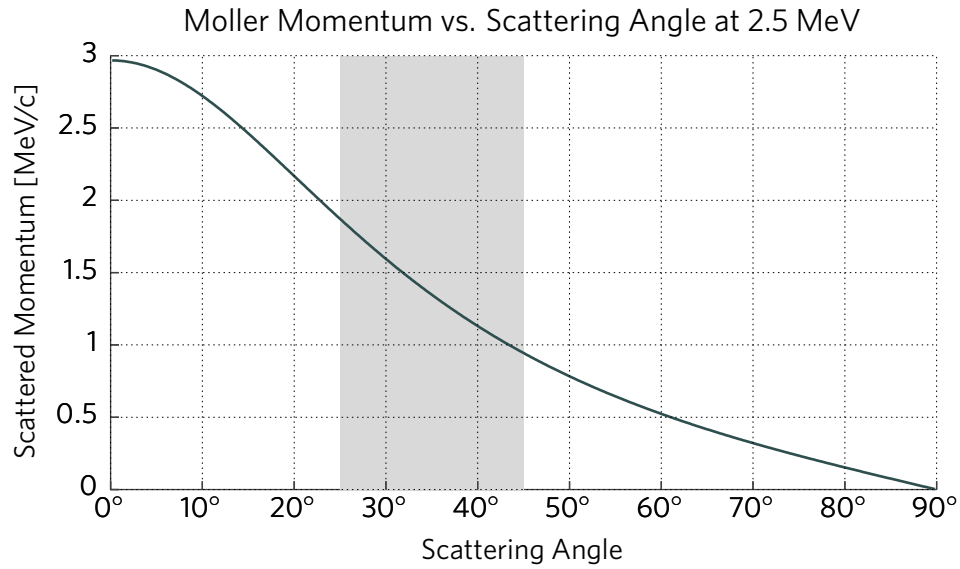


Figure 4-34: Møller electron momentum as a function of scattering angle, for a beam kinetic energy of 2.5 MeV. The spectrometer's 25°–45° acceptance is marked.

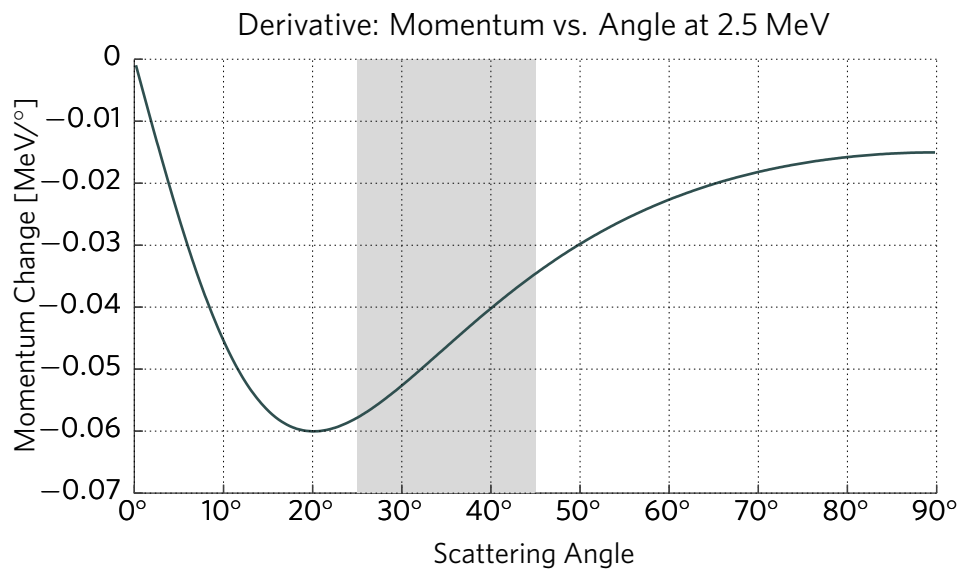


Figure 4-35: Derivative $\partial P_{\text{mol}}/\partial\theta$, as a function of θ . The spectrometer's 25°–45° acceptance is marked.

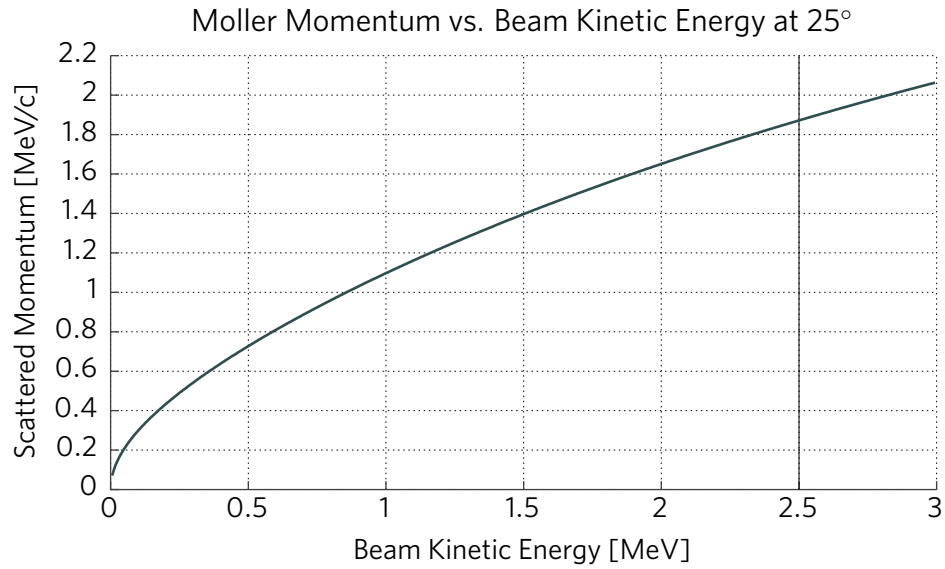


Figure 4-36: Møller momentum as a function of the beam kinetic energy, at a scattering angle of 25°. The nominal beam kinetic energy of 2.5 MeV is marked.

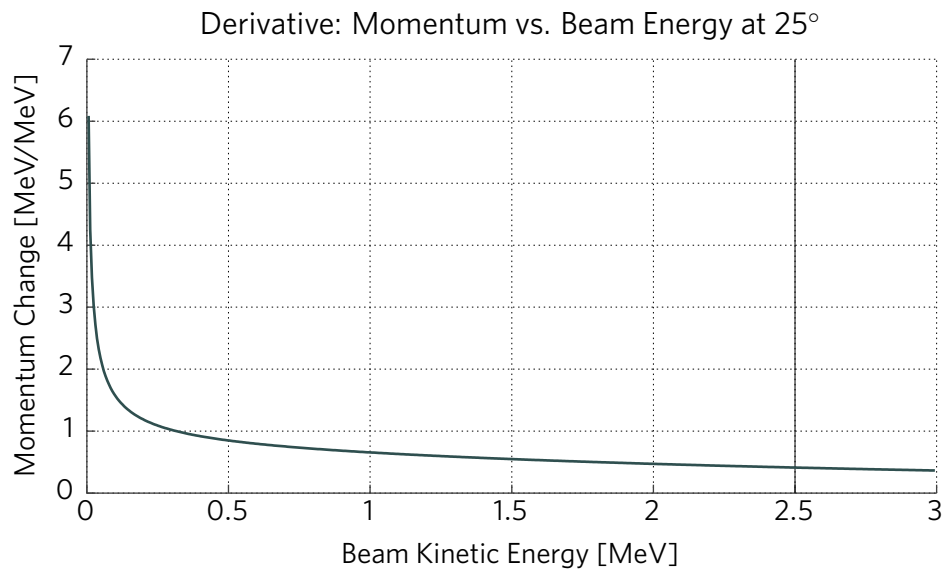


Figure 4-37: Derivative $\partial P_{\text{mol}}/\partial T_{\text{beam}}$. The nominal beam kinetic energy of 2.5 MeV is marked.

4.5.1 Direct Calculation of the Uncertainty

It is useful to directly calculate the contributions to the uncertainty on P_{beam} from the errors on the measurements of the scattering angle and the current ratio R . For lab-frame kinematics, we find that

$$P_{\text{mol}} = \frac{2mP_{\text{beam}} \cos \theta (E_{\text{beam}} + m)}{(E_{\text{beam}} + m)^2 - P_{\text{beam}}^2 \cos^2 \theta}. \quad (4.4)$$

This can be rearranged to show that

$$P_{\text{beam}} = \frac{2m \sqrt{\cos \theta (R - \cos \theta) (R \cos \theta - 1)}}{R \sin^2 \theta}. \quad (4.5)$$

From here, it is easy to calculate the contributions to the error on P_{beam} from both δR and $\delta \theta$. For the nominal $\theta = 25^\circ$ and $R = 0.631$, the total error on P_{beam} is represented by

$$\delta P_{\text{beam}}^2 = (13.2276 \delta R)^2 + (14.7708 \delta \theta)^2 \quad (4.6)$$

where $\delta \theta$ is measured in radians. Converting to a fractional error $\delta R/R \equiv \overline{\delta R}$, and expressing $\delta \theta$ in degrees, this becomes

$$\delta P_{\text{beam}}^2 = 69.61 \cdot \overline{\delta R}^2 + 0.0665 \cdot \delta \theta^2. \quad (4.7)$$

For $\overline{\delta R} = 0.1\%$ and $\delta \theta = 0.1^\circ$, this gives $\delta P_{\text{beam}} \approx 27$ keV. For $\overline{\delta R} = 0.1\%$ and $\delta \theta = 0.05^\circ$, we find $\delta P_{\text{beam}} \approx 15$ keV. Figures 4-38 and 4-39 show the individual contributions from $\overline{\delta R}$ and $\delta \theta$.

4.5.2 Surveying and Current Measurement Precision

In order to make a percent-level measurement, we have found that the scattering angle must be known to at least 0.1° , and the beam energy to about 15 keV. To measure the latter, the scattering angle must again be known to $<0.1^\circ$, and the current ratio $R = I_{\text{mol}}/I_{\text{eC}}$ must be known to about 0.1%.

Surveying the Angle of the Spectrometer

The angle of the spectrometer can be surveyed using a theodolite by harnessing the parallax effect. A baseline is drawn on the face of the spectrometer, with two marked points. Another baseline is marked on the floor, also with two marked points. At each point on the floor, the theodolite is used to measure the angles between the other three points. Figure 4-40 shows a schematic of what angles are measured. The angle between the baselines can then be calculated.

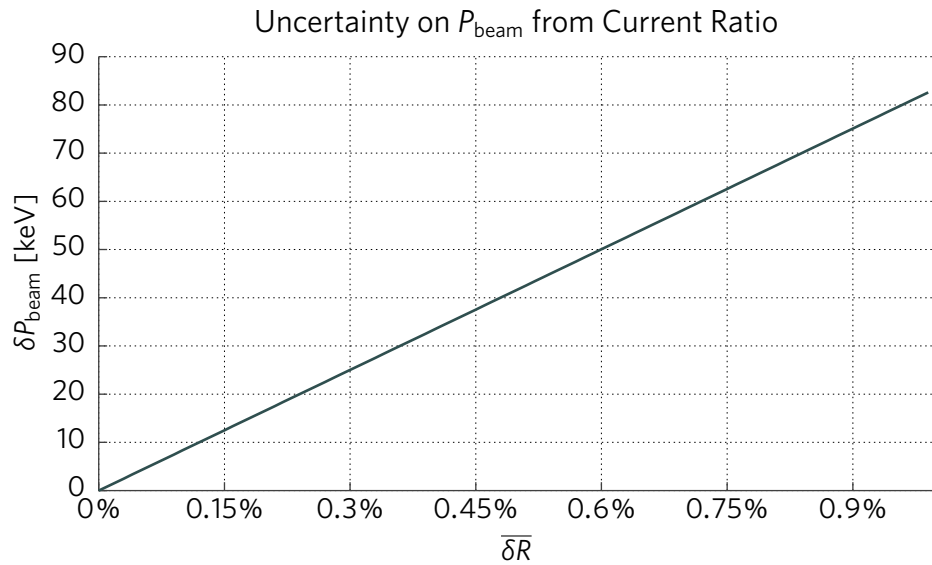


Figure 4-38: Uncertainty on the beam momentum δP_{beam} resulting from the error on the measurement of the current ratio. The error on the angle measurement is held at zero.

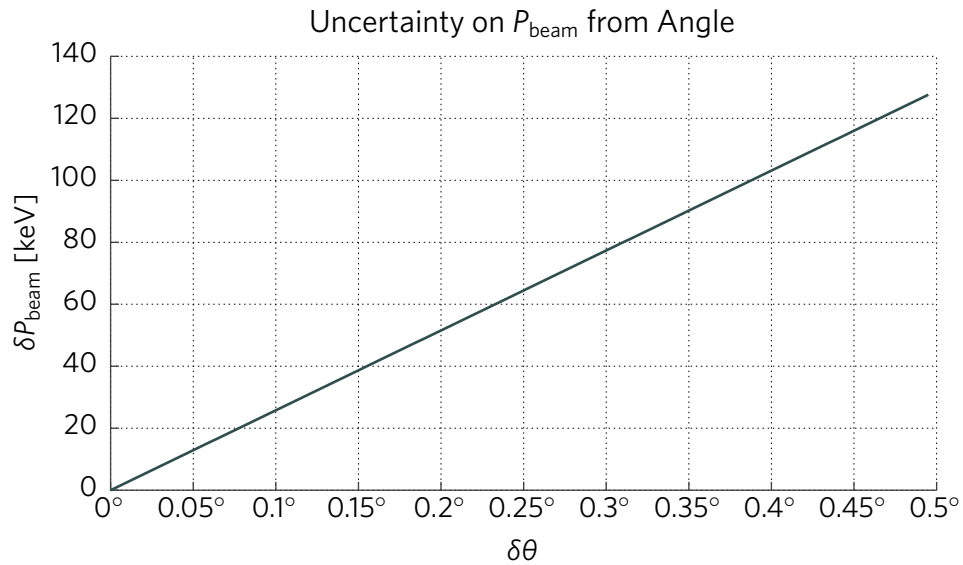


Figure 4-39: Uncertainty on the beam momentum δP_{beam} resulting from the error on the measurement of the angle. The error from the current ratio is held at zero.

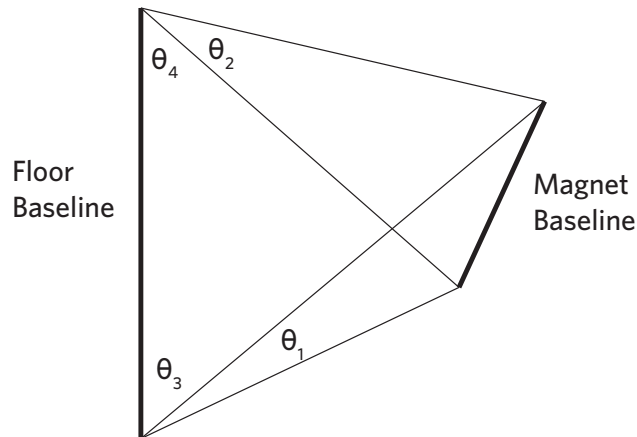


Figure 4-40: Schematic of the survey layout, with the four measured angles.

If the line on the floor is not parallel to the beam axis, the measurement can be repeated to calculate the offset.

The theodolites are precise to about 1 mgon (about 0.0009°). Distances can be measured routinely to approximately 1 mm. With toy angle values of $\theta_1 = 20^\circ$, $\theta_2 = 30^\circ$, $\theta_3 = 60^\circ$, and $\theta_4 = 30^\circ$, the angle between the baselines is $32.937^\circ \pm 0.079^\circ$. This is sufficiently precise for a 1% measurement.

Measuring the Current Ratio

Measuring the current ratio requires adjusting the magnet current so that the electron-carbon or Møller lines sit on the central trajectory. Doing this accurately depends on the detector precision, and how well the current is known. The detector has 60 tiles in a roughly 10% momentum window, reaching to a precision of approximately 0.2%. The magnet power supply has a built-in meter that is accurate to approximately 1%. An additional, more accurate ammeter may be necessary for this.

Knowledge of the Beam Angle

The angle of the HVRL beam relative to the central line of the assembly must also be known to approximately 0.1° . However, the beam angle is not currently known to high precision. A method of measuring and/or adjusting the angle of the beam will be important for a future 1% measurement.

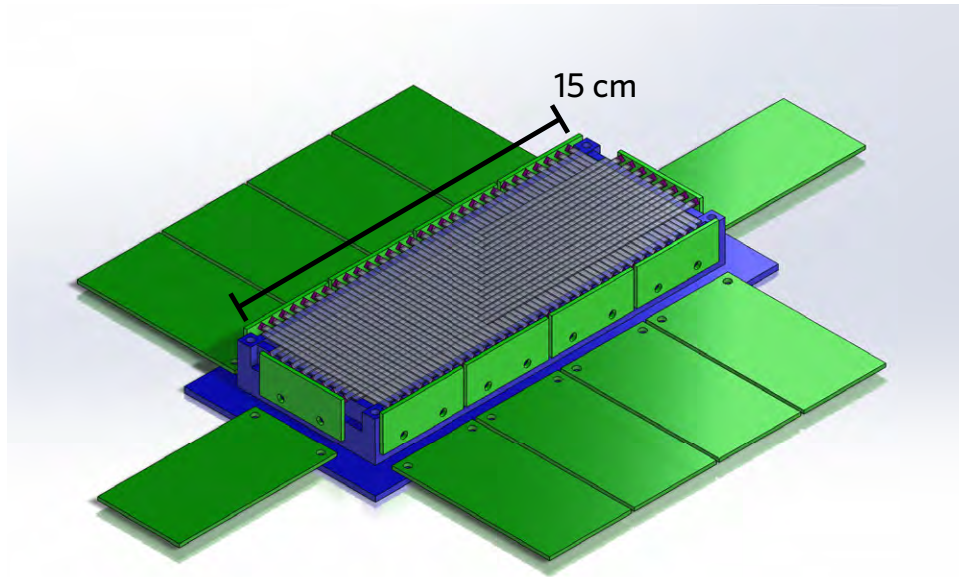


Figure 4-41: Layout of the detector, including scintillating tiles, SiPMs (and boards), amplifier boards, and a frame. The image is “upside-down”; electrons travel upward from the magnet and strike this shown side first.

4.6 Focal Plane Detector

The focal plane detector consists of a two-layer array of scintillating tiles (Fig. 4-41). The tiles are 2.5 mm wide and 0.5 mm thick, and were made in two lengths: 60 mm and 160 mm. These were made to our specifications by Eljen Technology and were diamond-milled in order to have optically-clear edges (Fig. 4-42). The material is their EJ-212, which is based on a combination of polyvinyltoluene and fluors, and is similar to Saint-Gobain’s BC-400. The intended active area is 4 cm × 15 cm, corresponding to 16 tiles (angle) by 60 tiles (momentum).

4.6.1 SiPMs and Readout Electronics

The SiPMs are 2 mm Hamamatsu MPPC S13360-2050VE. These have a physical pitch of 2.4 mm. The SiPMs were purchased in a large batch, and then sorted by breakdown voltage. Seventy-six SiPMs were chosen with extremely similar voltages, having a mean of 53.980 ± 0.026 V (0.05%). This allows a single high-voltage supply to provide a suitable bias to all of the SiPMs.

To align with the 2.5 mm tiles, the SiPMs are rotated at an angle of 45° (Fig. 4-44). The tiles are read out alternately on the left and right sides, to allow the SiPMs to be spaced 5 mm apart rather than constricting them to 2.5 mm.

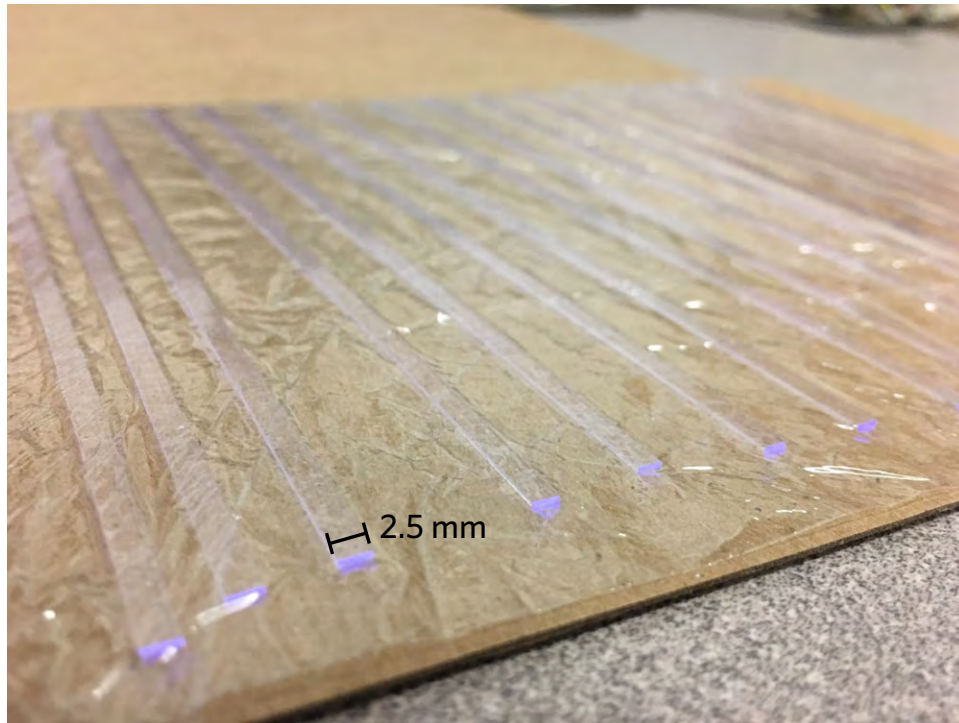


Figure 4-42: The scintillating tiles, in their packaging.

They are installed on eight-channel boards that mount directly to the side of the detector.

The amplifiers (Fig. 4-43) are intended to have both high gain and a fast rise-time. Each board contains eight channels, to facilitate a 1:1 connection between SiPM boards and amplifier boards. They contain an on-board discriminator based around an LTC6754 comparator. An onboard eight-channel digital-to-analog converter (DAC) outputs voltages to the comparators, which use them to evaluate pulses from the SiPMs. Upon positively identifying a pulse, the comparator then outputs a digital LVDS signal directly to the TDC. Each of the DAC's output voltages can be set individually using a serial interface. Individual timing offsets for each pair of channels were determined at the analysis stage, by histogramming the hit time separations. A 5 ns window was chosen to define coincidences, consistent with both the histograms and the intrinsic pulse rise time.

In a polyvinyltoluene-based scintillator, a 1 MeV electron is expected to have an energy loss of $1.824 \text{ MeV cm}^2/\text{g}$ [28]. This equates to approximately 93 keV in 0.5 mm. The scintillator emits approximately 10,000 photons per MeV [29], indicating that approximately 930 photons are emitted. A rectangular fiber traps approximately 4% of emitted photons [30] (further attenuation

notwithstanding), indicating that approximately 37 reach the SiPM. The SiPM has a detection efficiency of approximately 40% [31], indicating that roughly 15 photons will be detected on a typical event. A precise conversion between number of photons and pulse voltage is not known; however a threshold of approximately 650 mV was used by the discriminator, as this was the lowest possible that could sufficiently reject background noise.

Figure 4-43 illustrates the layout of an amplifier board. The components are labeled as such:

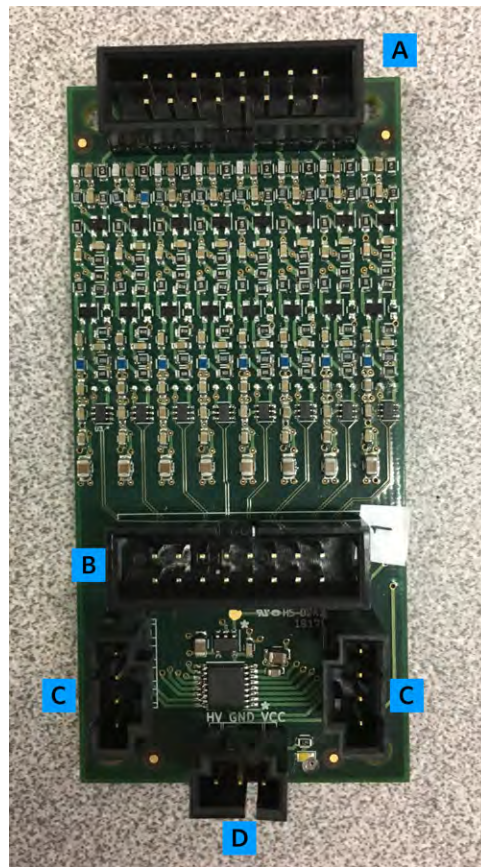


Figure 4-43: An amplifier board with connectors labeled.

- A** Input from SiPM board
- B** LVDS data output
- C** Slow control input, and daisy-chain output
- D** Power

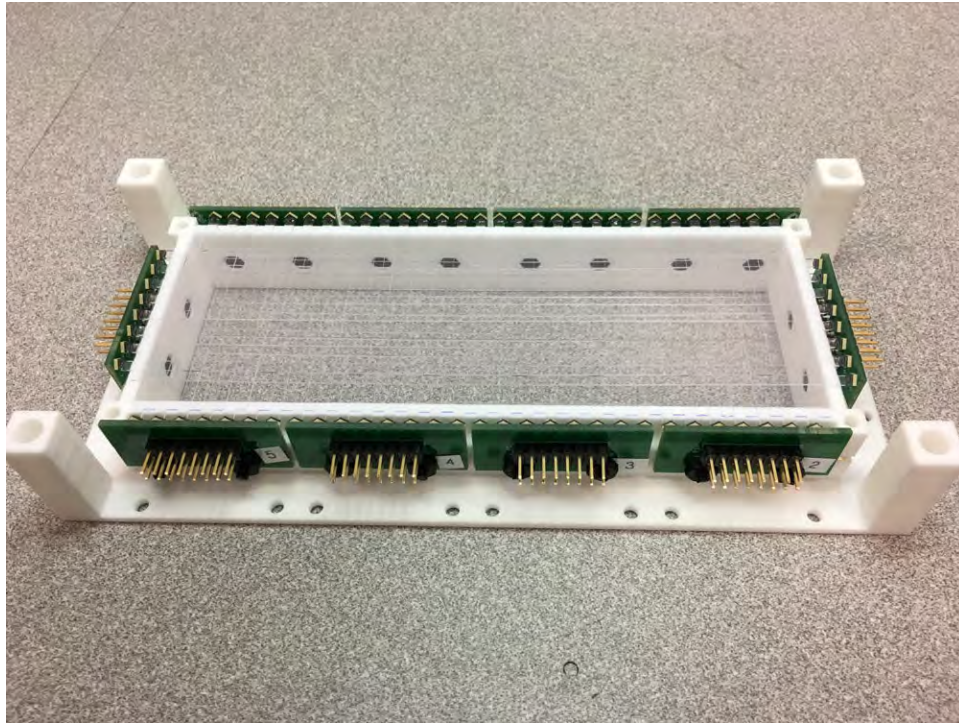


Figure 4-44: The partially-assembled focal plane detector, showing 2 mm SiPMs oriented at an angle.



Figure 4-45: Closeup of the focal plane detector support structure.

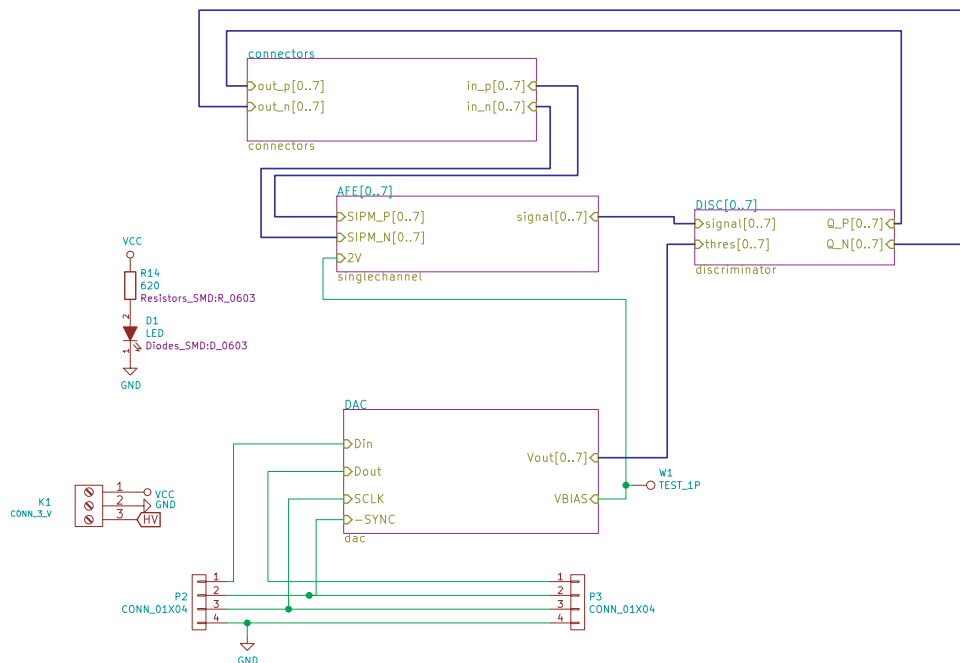


Figure 4-46: Overall amplifier/discriminator board schematic. (J. Bernauer)

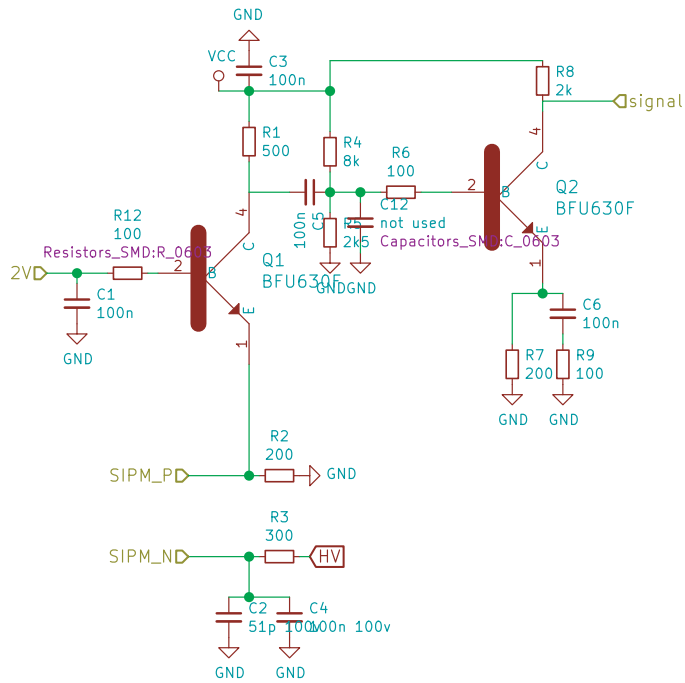


Figure 4-47: Circuit diagram for a single channel. (J. Bernauer)

4.6.2 Detector Construction

The detector frame was 3D printed from nylon via a selective laser sintering process. This allowed complicated shapes to be implemented. For example, hexagonal countersinks are located on the inside of the detector, to hold nylon bolts connecting the SiPM boards. The detector frame is visible in Fig. 4-44. The frame is mounted on a support designed and constructed at Bates (Fig. 4-51). The support is composed of a red G20 piece that sits on the focal plane flange, and a stainless piece that holds the amplifier boards in place. These pieces clamp together around the detector frame. The amplifier boards are mounted at a 45° flare-out in order to maximize access while still keeping them close to the SiPM boards.

4.6.3 Initial Idealized Simulations

Figure 4-52 shows a simulated hit map on the focal plane detector. This was produced using a Geant4 simulation of the entire apparatus under idealized conditions, with the magnet positioned at 25°. Events were defined as having at least one hit above threshold in each of the two planes. The X Fiber maps to momentum, and the Y Fiber maps to scattering angle.

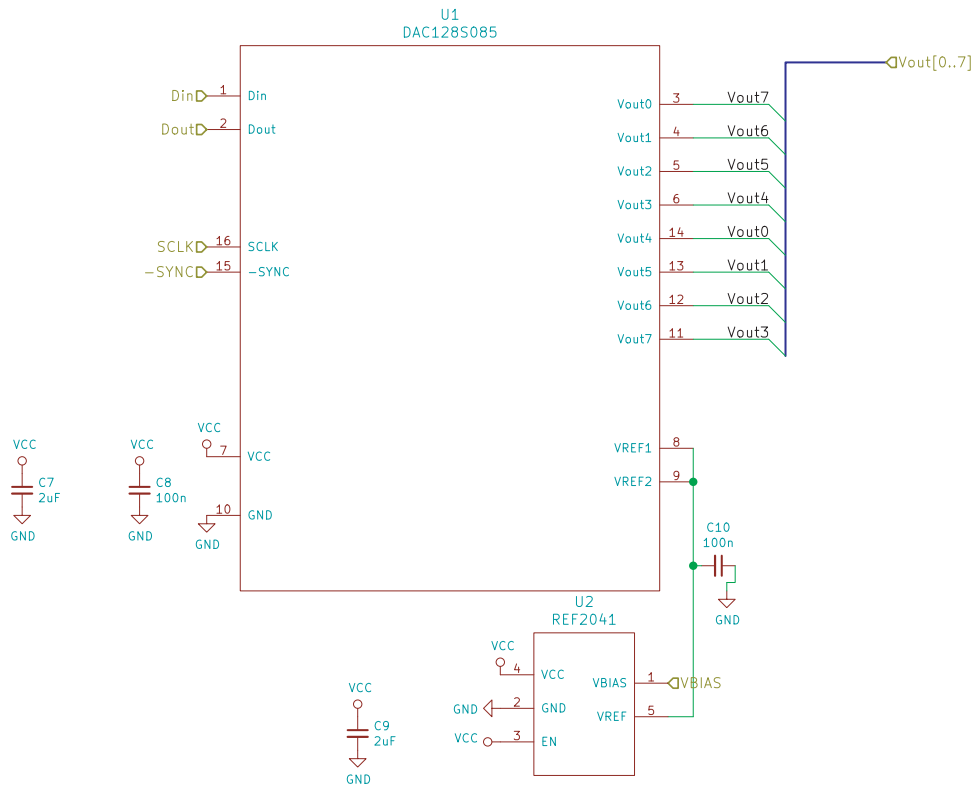


Figure 4-48: Circuit diagram for the DAC component. (J. Bernauer)

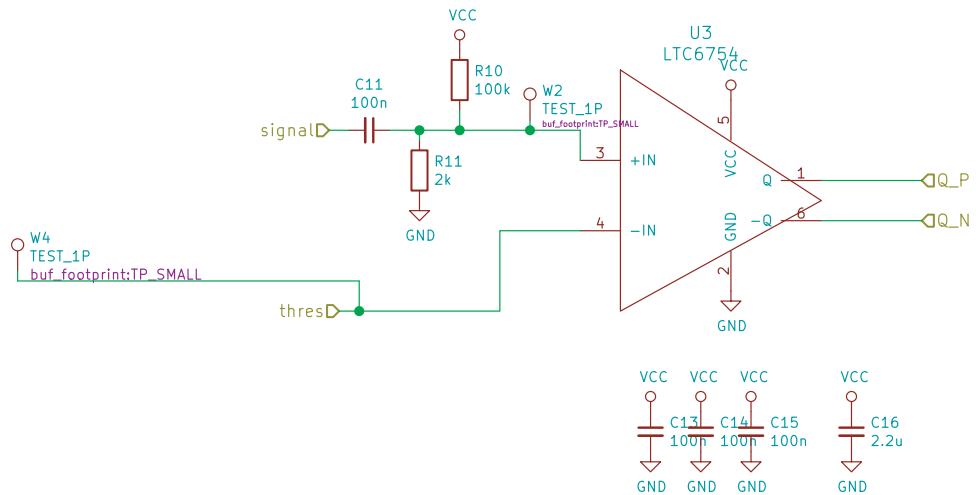


Figure 4-49: Circuit diagram for the discriminator section, including the comparator. (J. Bernauer)

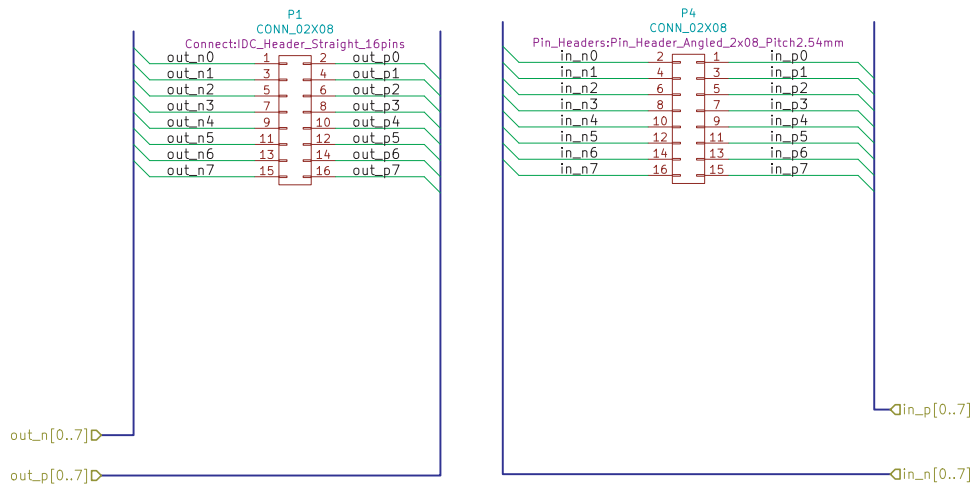


Figure 4-50: Diagram of the connector inputs/outputs. (J. Bernauer)

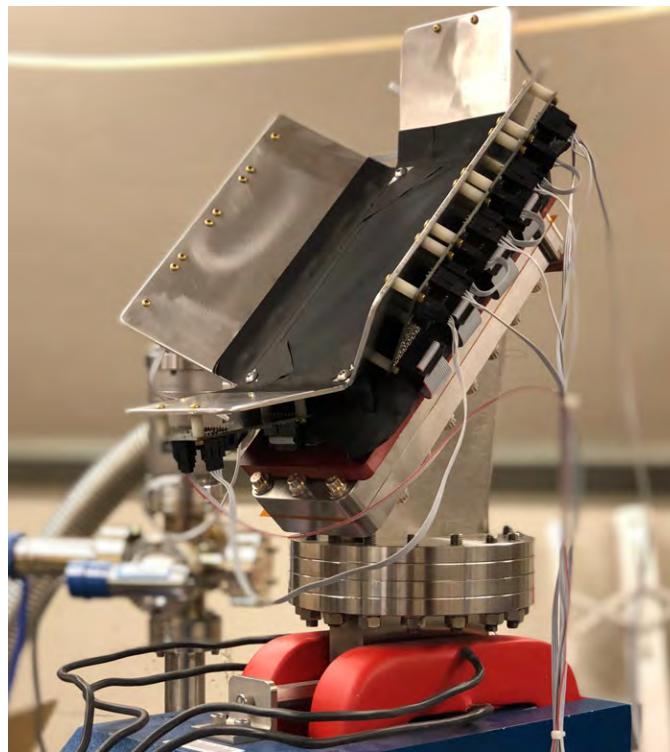


Figure 4-51: The focal plane detector, mounted to the spectrometer. Data cables are not shown.

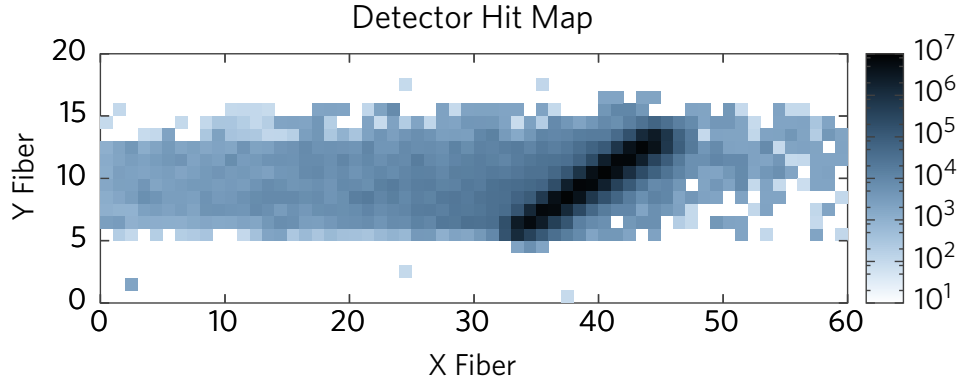


Figure 4-52: Idealized simulated hit map on the focal plane detector for a 2.5 MeV beam at 25°. *X Fiber* corresponds to momentum (lowest left), and *Y Fiber* scattering angle (lowest top).

4.7 Commissioning Run

A reduced detector was installed at the HVRL for the main purpose of visualizing the beam (see image in Fig. 4-53). This detector consisted of:

- The movable target ladder with two carbon targets and the beryllium oxide screen.
- A single camera, to view the BeO screen through the target chamber port.
- Both spectrometer ports blanked off with aluminum.
- Beam exit flange blanked off with aluminum.
- No power to the spectrometer magnet.

The camera recorded video of the BeO screen for the entirety of the run. It was read out on a computer located in the upstairs control room. This allowed the video to be watched in real time, while tuning the beam. The target ladder, and later the quadrupole magnet, were also read out and controlled from upstairs.

4.7.1 Beam Delivery and Focus

A 2.5 MeV electron beam of approximately 1 μA was delivered to the Radiative Møller experiment. According to the GVM readout, the beam energy was approximately 2.502–2.504 MeV, and this was held stable throughout the course of the run. The downward-going beam was bent into the horizontal plane, and then traveled a distance of approximately 2 meters to the target (Fig. 4-54). The beam spot was visualized on a Beryllium Oxide screen. The screen is



Figure 4-53: The commissioning run apparatus.

approximately 1.375" tall, and has a 1/8"-diameter hole at the center. Several hours of optimization were required to find the settings that would put the beam on target.

Using the existing equipment, the beam could not be focused to better than approximately 0.75" in diameter (Fig. 4-55). This is not sufficient. A single quadrupole was installed approximately 28.5" from the 90° bend, for exploratory purposes (Fig. 4-57). It was used to focus the beam into a horizontal line approximately 1/16" tall (Fig. 4-56). A current of approximately 0.3 A (voltage of 0.7 V) was required to focus the beam; this corresponds to fields of roughly 50 Gauss. The opposite polarity was checked, to vertically focus the beam, but not thoroughly tested due to the difficulty of positioning the line.

4.7.2 Target Scan

While the beam was focused into a line, the target ladder was swept down and up. This directed the 2.5 MeV electrons onto the carbon foil targets. No damage to the targets was observed.

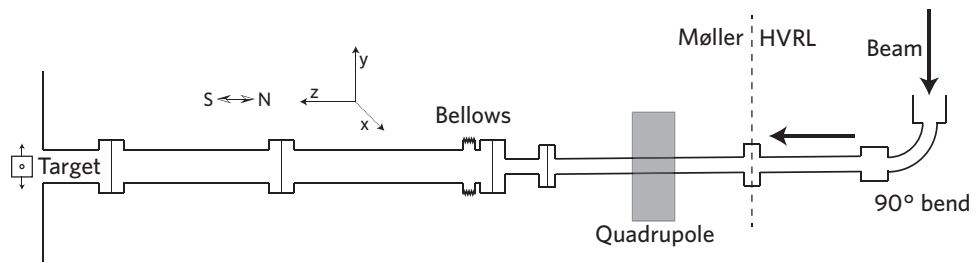


Figure 4-54: The commissioning run beamline configuration. The dashed line indicates the nominal border between the accelerator and the Radiative Møller apparatus.

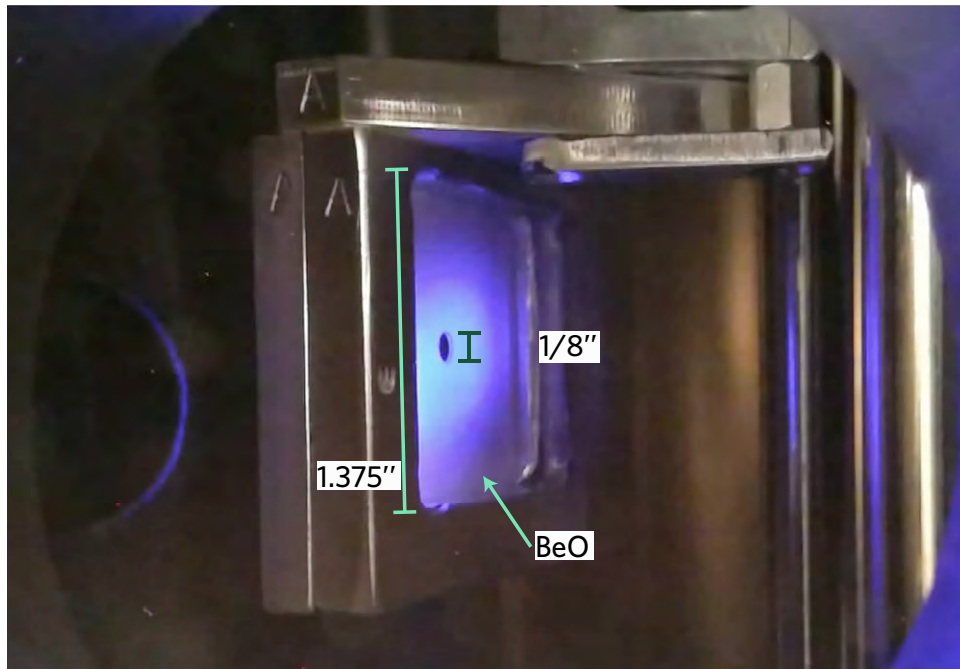


Figure 4-55: The beam profile, without focusing.

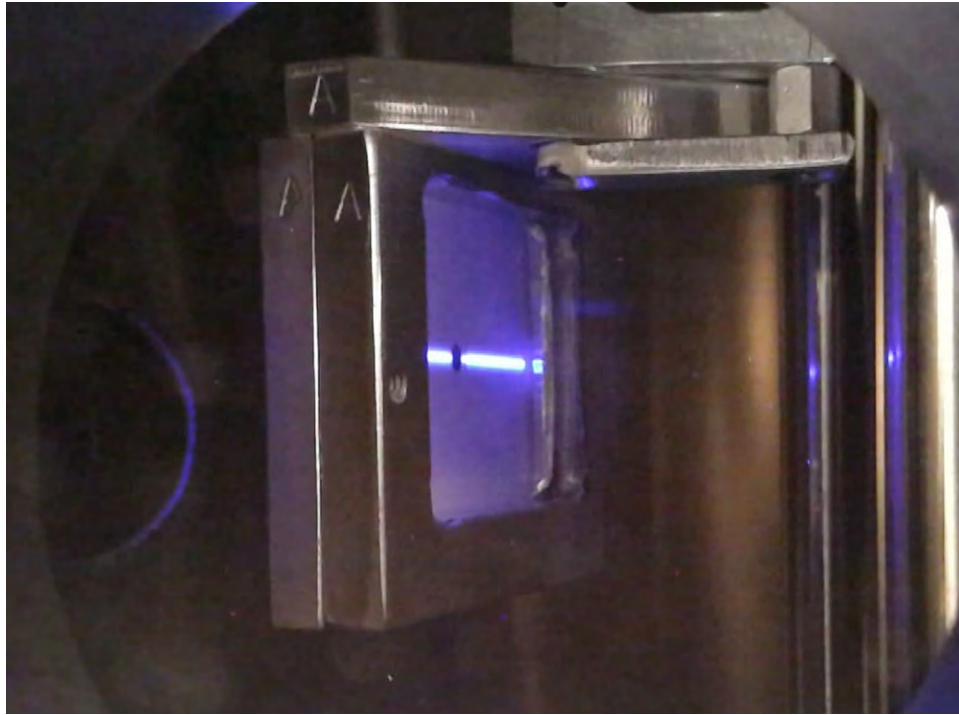


Figure 4-56: The beam profile, after focusing by a single quadrupole.

4.7.3 Accelerator Optimization

On the third day of beam commissioning, the accelerator controls were scanned to determine the optimal settings. Some of the parameters that were changed include:

- Beam focusing solenoid current (upstairs, at accelerator exit)
- Upstream beam steering controls (N-S and E-W)
- 90° magnet current

Two particularly important parameters were scanned: N-S beam steering, and 90° magnet current. The former controls the location of where the beam enters the 90° magnet (Fig. 4-58), and the latter its bending strength. If the beam hits the target, the exact path it took to get there is not known: various combinations of these controls put the beam on target. The edges of the workable parameter space were determined. In the middle, the least amount of beam distortion was observed. These parameters were recorded for future runs. It is believed that they direct the beam to the center of the 90° bend.

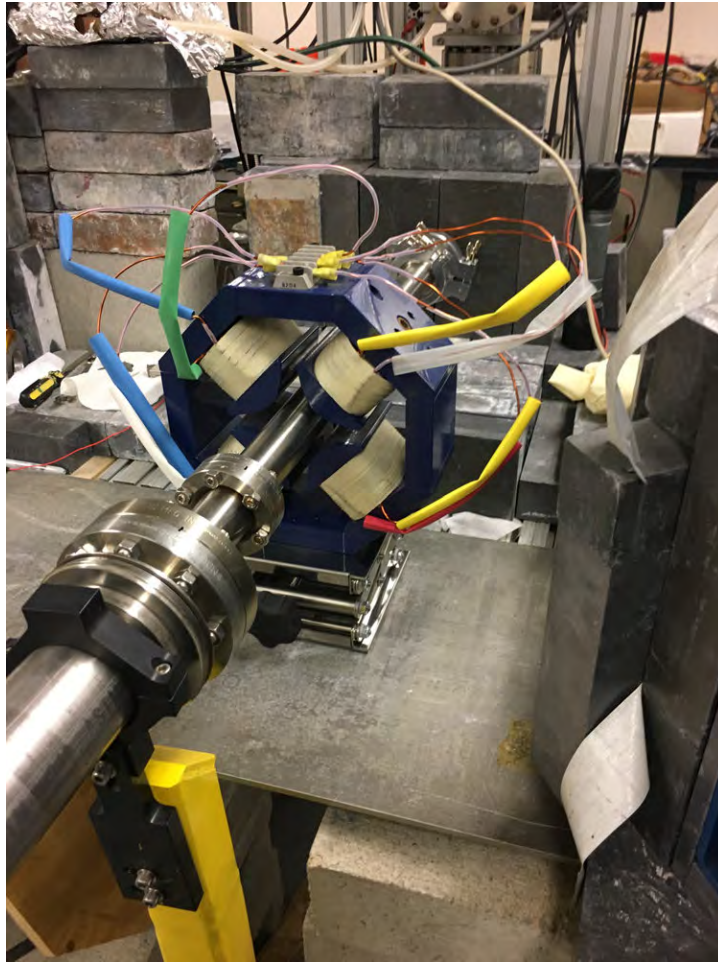


Figure 4-57: The quadrupole installed on the beamline.

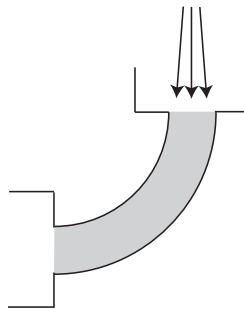


Figure 4-58: One of the beam parameters explored: the angle/position entering the 90° bend magnet (shaded area).

4.7.4 Conclusions from the Commissioning Run

The commissioning run identified that a beam can be produced, but that additional infrastructure would be required to reduce the spot size and control its position. In particular, focusing and steering magnets would be required.

4.8 Upgrades Installed after the Commissioning Run

After the commissioning run, a number of priorities were identified. First, the installation of a new pair of quadrupoles would be essential. Second, two sets of steering coils were desired. Third, the new Faraday Cup would be tested and installed in the apparatus. During the Fall of 2017, these goals were achieved.

These upgrades necessitated a replacement of the existing upstream beamline with one of a smaller diameter, in order to accommodate the quadrupoles. In the process, a gate valve was installed to separate the experiment from the HVRL's vacuum, when necessary. A 6-way cross was also installed, for the dual purpose of housing a nitrogen backfill port and a future second BeO screen.

4.8.1 Faraday Cup

A Faraday Cup was developed with the goal of measuring the beam current (typically 10–100 nA) to 1%. It was designed to connect at the far downstream end of the experimental apparatus to provide an online, real-time current monitor, by collecting the scattered beam electrons (e.g. [32, 33, 34]) and measuring them with an electrometer [35]. The Faraday Cup operates under vacuum, in order to achieve the cleanest signal. It has an optional bias of up to 500 V, in order to trap backscattered electrons. Figure 4-59 shows a diagram of the construction; Fig. 4-60 indicates the internal dimensions.

The Faraday Cup was tested by connecting it directly to the beamline (Fig. 4-61). This permitted troubleshooting prior to the more-permanent installation at the downstream end of the experiment. The bias voltage was scanned, but no change in the signal was observed. As a result, in future runs, the bias was left disconnected. The accelerator controls were also further optimized to maximize the current delivered to the location of the Faraday Cup.

4.8.2 Quadrupoles and Steering Magnets

With the aid of the MIT Bates Laboratory, two quadrupoles and two sets of steering coils were installed at the upstream end of the beamline (Figs. 4-62, 4-63). They were constructed to fit around the new 1.5'' upstream beamline. The

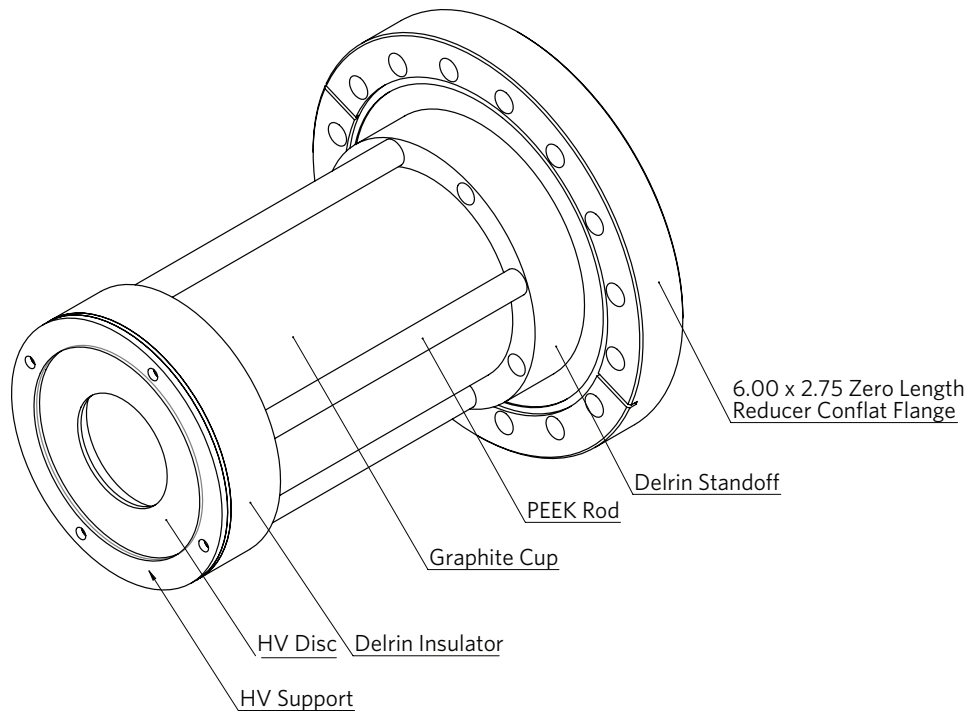


Figure 4-59: Diagram of the Faraday Cup construction.

quadrupoles were oriented such that they focused in the vertical and horizontal directions. They were mounted on a track, to allow for easy positioning. The track sat on a sturdy support plate, precisely positionable using turnbuckles. Two full sets of Haimson air-core steering magnets were mounted before and after the quadrupoles (Fig. 4-64). These provided more-than-adequate position control of the beam. The beam quality at the target location was substantially improved after installation of the quadrupoles and steerers. A spot size of approximately 1/8" was routinely achievable (Fig. 4-65).

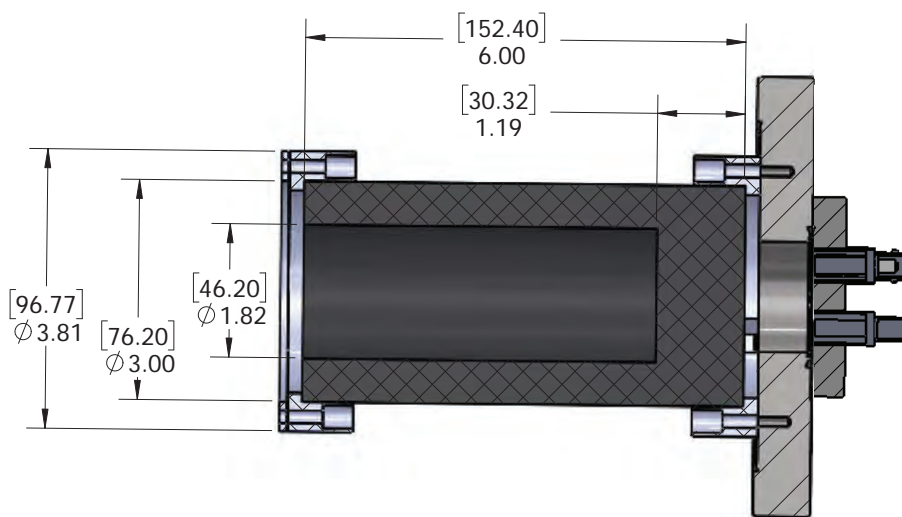


Figure 4-60: Faraday Cup cutaway view including dimensions. Bracketed dimensions are in millimeters, unbracketed in inches.



Figure 4-61: The Faraday Cup, installed directly on the beamline.

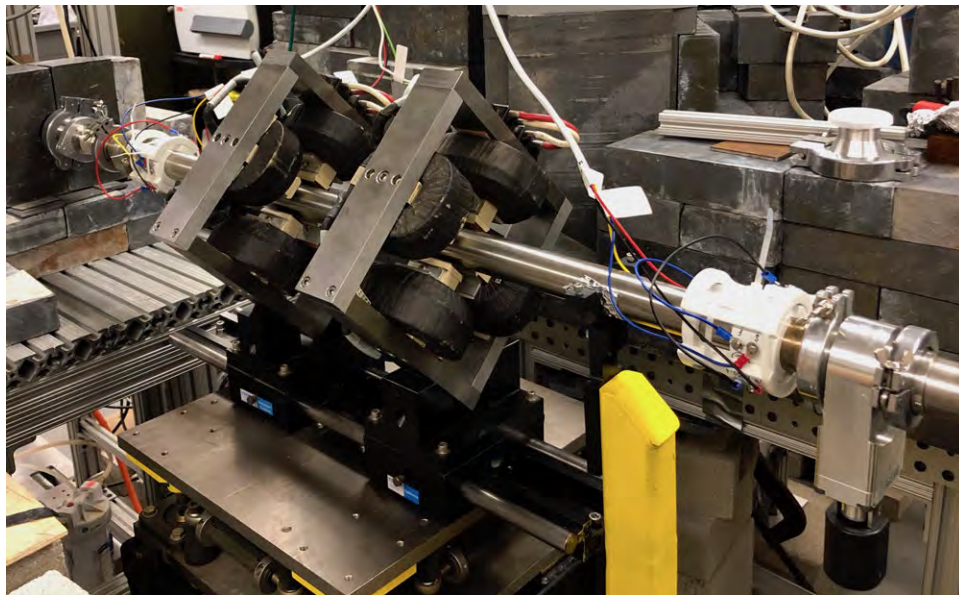


Figure 4-62: The quadrupoles, steering magnets, and gate valve.

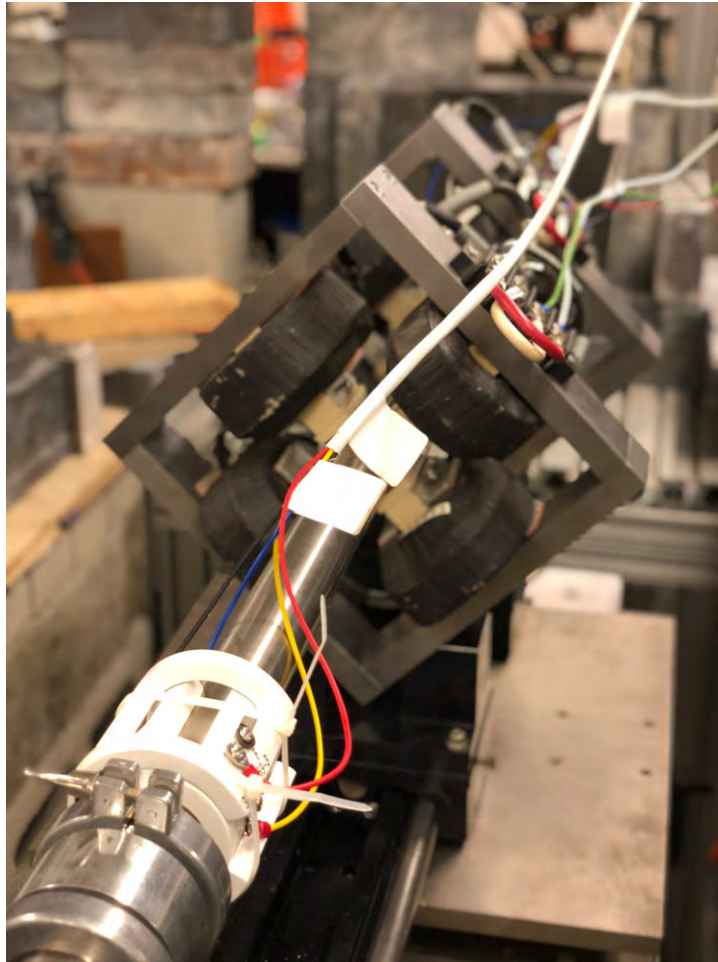


Figure 4-63: Steering magnets and quadrupoles.

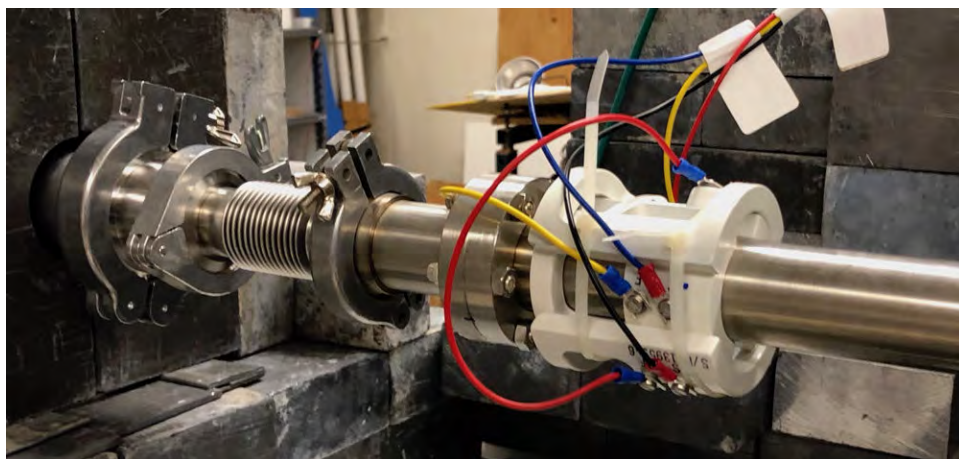


Figure 4-64: Haimson steering coils, attached to the beamline.

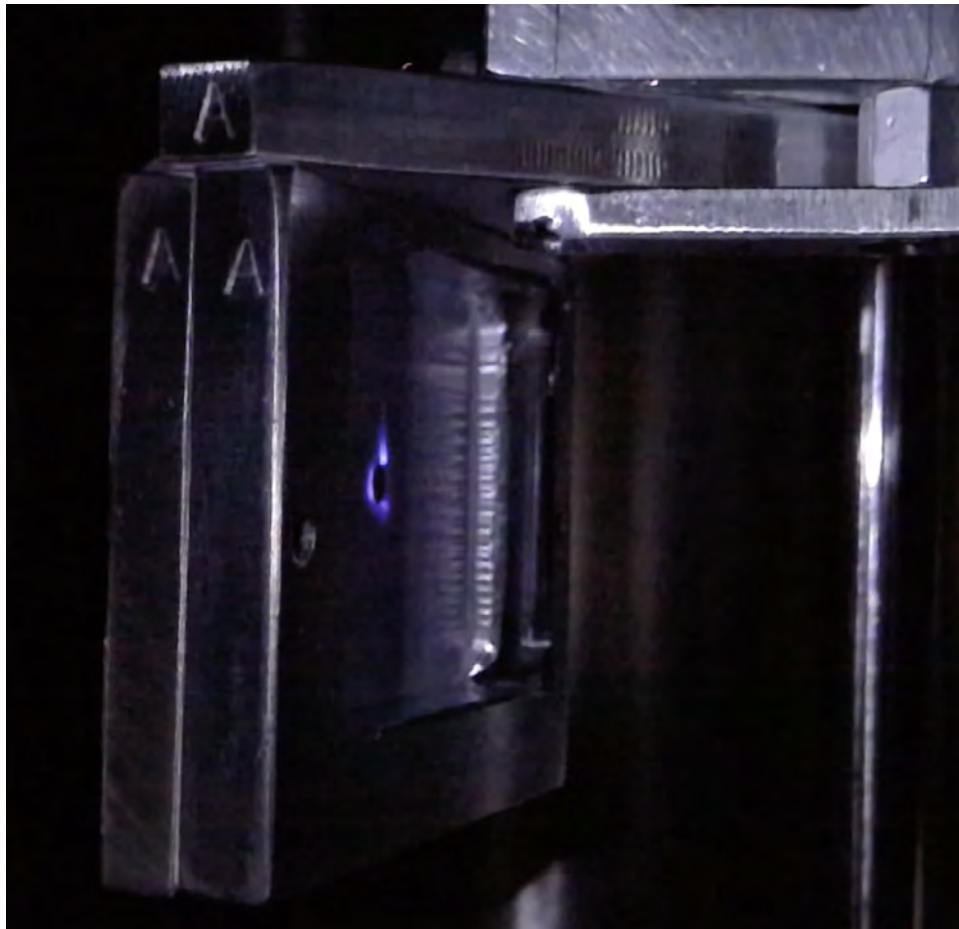


Figure 4-65: Beam spot after installation of the quadrupoles and steerers. The halo is visible, while the majority of the beam passes through the 1/8" hole.

THIS PAGE INTENTIONALLY LEFT BLANK

Chapter 5

Slow Control and Data Acquisition Systems

A wide variety of systems were developed in order to facilitate the running of the experiment. These included new custom data acquisition/processing software, a LabView slow-control graphical interface, and some additional custom Python controllers. The majority of the experimental hardware systems were controlled using two primary computers. This chapter describes how these systems were realized and configured.

5.1 Data Acquisition with the VME TDC

The focal-plane detector's amplifier/discriminator cards contain an LTC6754 comparator for each channel. These each produce a digital LVDS pulse when the associated SiPM voltage rises above threshold. A CAEN VME v1190A TDC reads out the pulses and assigns a time to each hit. Code documentation can be found in Appendix A.

In a typical configuration, the TDC outputs the time difference between a trigger pulse and a signal pulse, using a high-resolution clock. However, we prefer to stream all of the hits out of the TDC and do the analysis in software. This requires gathering the hit channels and their absolute hit times from the TDC. In the end, we want channel-time pairs upon which to perform the analysis.

The primary clock is 32 bits long with a period of 98 ps: this rolls over approximately every 52 μ s. If this were the only clock, it would be impossible to tell whether events in the data stream occurred near the same time (were related), or were actually separated by more than 52 μ s. Two events in a batch could receive similar clock values, but be separated by an unknown number of rollovers. As a result, a counter longer than the primary clock is required in

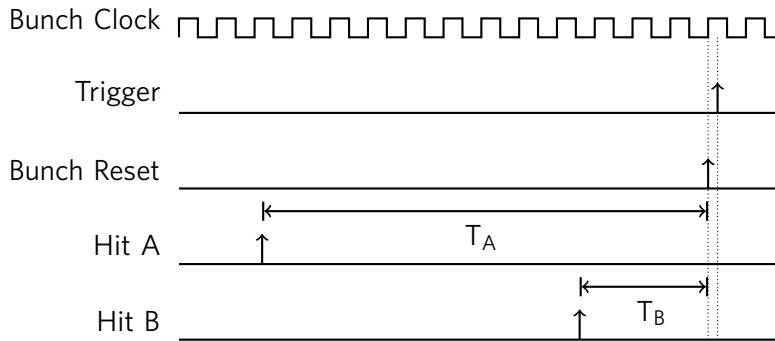


Figure 5-1: Diagram of the times measured in a trigger window. *Clock* refers to the bunch clock ETTT; T_A and T_B are measured using the high resolution, 98 ps timer. Based on figure from [36].

order to tell these apart.

Fortunately, the TDC includes a secondary 32-bit, extended counter, with a resolution of 25 ns. This is commonly referred to as the *bunch counter*. This bunch counter rolls over approximately every 10^7 seconds. When this counter is saved, its value is referred to as the Extended Trigger Time Tag (ETTT). When the TDC receives a trigger signal, it records the bunch counter as the ETTT; when it receives an event pulse, it records the time between it and the bunch increment¹. Figure 5-1 illustrates the times that are recorded for an example trigger window. By combining the short, high-resolution time with the longer ETTT, an absolute hit time can be reconstructed with a full resolution of 98 ps. This can be used by the DAQ software to evaluate coincidence matching. In order to enable continuous readout, a function generator configured to output a -0.8 V (NIM-level) square wave provides a constantly-running fixed-frequency trigger.

5.1.1 Programming the TDC

A number of trigger parameters are set when configuring the TDC (see Fig. 5-2). They are:

- **Match window width**

This sets the length of the match window, in 25 ns clock cycles. The maximum is 2048.

- **Match window offset**

This sets the offset of the match window from the trigger signal. It is

¹The TDC can be configured to output the time to the trigger signal rather than the bunch increment. However, this is not our desired mode of operation, because it introduces a jitter of 25 ns to our quantity of interest.

typically negative. For a continuous set of measurements like we are performing, it is mostly meaningless.

- **Extra search window width**

The TDC accumulates events in the L1 buffer while waiting for a trigger signal. The events are not necessarily written in temporal order. This window width is a measure of how far away to look when searching for matching hits.

- **Reject margin**

In the L1 buffer, hits are stored until no conceivable trigger could require them. The reject margin sets how much longer, than the minimum required time, hits should be kept before being discarded.

- **Trigger time subtraction (enabled/disabled)**

If enabled, the hit time is measured to the trigger signal. If disabled, it is measured to the bunch reset.

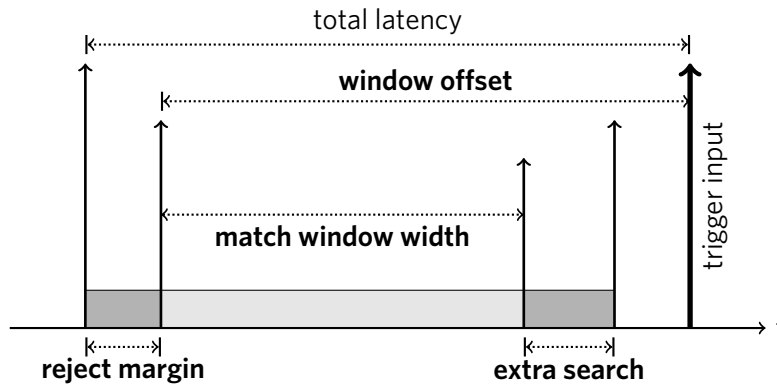


Figure 5-2: Diagram of the configurable trigger timing options. Items in bold are programmable. Based on figure from [36].

Table 5.1 shows typical operation parameters. Appendix A.3 shows a typical configuration script.

5.2 Data Acquisition Software

The TDC streams binary output to a FIFO buffer. The DAQ software reads the raw data from this buffer, and recovers the channel and timing information. However, in order to provide a tool to tune the detector, the DAQ must also be able to visualize the detected hits in real time. Additionally, it must be fast: the DAQ must read events from the FIFO buffer at least as fast as it is filled, in order

Table 5.1: Typical TDC configuration parameters.

Match window width	2032 (0x7F0)
Match window offset	-2032 (0xF810)
Extra search window width	8 (0x08)
Reject margin	2 (0x02)
Trigger time subtraction	Disabled (0x00)
Control register	Bits 5, 9 and 11 (0xa20)
TDC header and trailer	Disabled (0x3100)
Maximum hits per event	Unlimited (0x3300 and 0x0009)

that no events are lost. Software, written in Python/Cython, was developed in order to meet these goals.

5.2.1 Software Structure

The DAQ software is multithreaded and split into specialized modules. Figure 5-3 shows the direction of data flow through the DAQ.

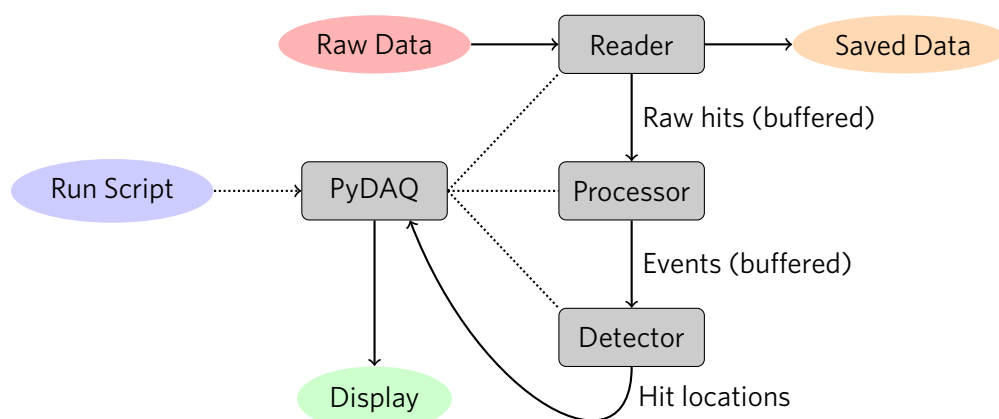


Figure 5-3: The data path in the acquisition software.

There are three primary components to the DAQ software: the Reader, Processor, and Detector. These are all managed by the main DAQ class (PyDAQ), which is controlled in the Run Script (RunDAQ.py). The Run Script provides the DAQ with Reader, Processor, and Detector instances, and instructions on where to find the data, where to save it, and where to display it. The Reader and Processor each run in separate background threads, communicating via buffers. The Detector processing is controlled in the main thread.

The Reader

The *Reader* extracts hits from the FIFO buffer and decodes them. First, the raw decoded version is saved to a PyTables HDF5 file. The reader continues by reconstructing the absolute time for each of the recorded hits. It then passes these channel-time pairs to an internal buffer.

There is a secondary option in which the Reader can receive hits from a ZMQ TCP/IP stream. This allows the DAQ chain to be split onto different computers, or different programs. This option is not commonly used.

The Processor

The *Processor* pulls channel-time pairs off the raw hit buffer, and processes them into *events*. There are multiple processors that can be used. For example, a Coincidence Processor selects groups of hits that are separated by less than the specified coincidence window. A Direct Processor records some basic information, and then passes the events along. These *events* are then saved to a second internal buffer.

The Detector

The *Detector* pulls events from the Processor buffer, and then translates them into physical, reconstructed detector hits. The Detector contains information about our scintillating tile detector; in particular, a mapping from TDC channel to physical tile location. Typically, the Detector is run at a refresh rate of ~ 1 Hz, processing ~ 1 s worth of events per frame.

A Coincidence Detector processes events by analyzing the groups of coincidence hits. First, it sorts them by whether they were located in the top or bottom tile layers. It then looks at top/bottom hit pairs, and calculates all possible hit locations. These locations are then displayed, in real-time.

A Direct Detector simply identifies which tile was hit. The entire tile bar is shown on the screen, rather than just the intersection spot. However, the intersection point will be incremented twice (one for each hit), so it will appear highlighted.

Visualization

Primarily, the detector hits are shown directly in the terminal. Here, special ASCII characters are used in order to display an image of the hit locations. Associated rates/counts are included, such as the total number of counts, total rate, and rate for each tile.

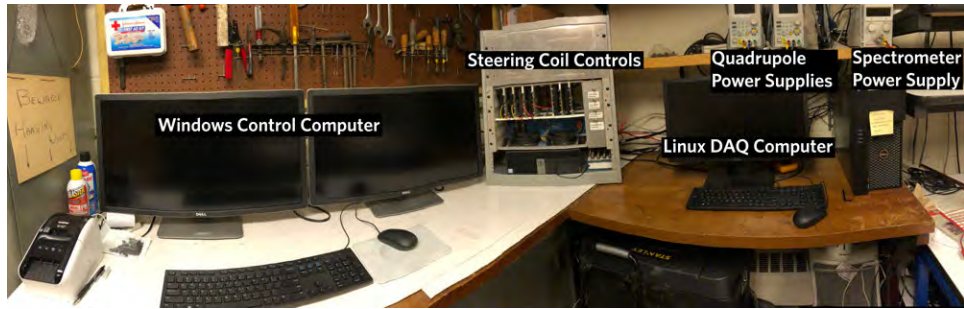


Figure 5-4: Layout of the experiment control panel.

A secondary method of visualization is via streaming to plot.ly, a cloud-based plotting service. This produces prettier plots and allows any internet-connected computer to see the live results, but it is bulkier and its features are not typically necessary.

5.3 Magnets and their Controls

The magnets in use during the experiment included:

- Main spectrometer magnet
- Two sets of X-Y steering coils (total four current controls)
- Two quadrupoles (total two current controls)

The main spectrometer magnet was controlled by a Sorenson XPD programmable power supply, drawing currents from approximately 0 to 6 amps. Due to the limited precision of the on-board display, this was largely controlled via a computer. The quadrupoles were controlled with Rigol DP700 power supplies connected via serial, requiring currents of roughly 0 to 1.5 amps.

The steering coils were controlled by a specialized crate provided by Bates. This provided an interface for a bipolar power supply, offering currents ranging from -0.5 A to 0.5 A. Each coil circuit (four in total) had an associated current distribution card. These cards were controlled by a voltage ranging from -5 V to 5 V, used in a feedback loop to regulate the output current. The control voltages were provided by a secondary on-board power supply and were adjusted by potentiometers. A computer interface was used to read out the control voltages and provide a display. Later, a USB-controlled voltage output device replaced the secondary ± 5 V supply, allowing LabView control of the steering coils.

5.4 LabView Control Software

The majority of slow controls were automated through a LabView interface. A National Instruments PXIe crate containing Analog IO and Serial RS-232 modules, connected via PCIe, provided the hardware interface between the devices and a Windows host computer. This allowed control of the following:

- Target ladder position control and readout
 - This used a USB relay to control the actuator, and an analog input to read back the encoder position.
- Steering coil current readout
 - This was provided by four analog inputs.
- Steering coil current control (provided by a separate NI USB BNC analog voltage output device)
- Faraday Cup current readout
 - Facilitated by a serial connection to a Keithley electrometer.
- Accelerator terminal voltage readout
 - This made use of a board of ADCs connected to the HVRL eBeam control panel.
- Detector power and SiPM bias
 - This was achieved via RS-232 connection to a power supply located in the basement.

The Windows machine also displayed the output of a USB camera focused on the BeO screen. The Linux DAQ computer, located in the control room, was connected via ethernet to the VME crate (in the vault). This machine oversaw the readout of the following:

- A sodium iodide (NaI) detector measuring backgrounds in the vault, connected directly via USB.
- Data acquisition, via the DAQ software running on the VME crate.
- An Arduino, connected to the VME crate, used to control the discriminator threshold on the detector cards.
- The main spectrometer power supply, connected to the VME crate via RS-232 and controlled by a custom slow-control shell.

By and large, the magnet power supplies were located in the control room, and all readout electronics were located in the vault. This required a significant amount of cabling: approximately 70 feet per run. The long RS-232 connections were facilitated by active serial-over-ethernet repeaters, and direct USB 3.0 repeating cables were used for the other connections.

5.5 Typical Run Protocol

After becoming comfortable with the system, it could be tuned relatively quickly and reliably. The following steps were typically taken, to produce a beam and start data acquisition. This protocol was repeated each time the accelerator was turned on, or the parameters modified (due to drift, or other instabilities).

1. Lower the BeO oxide screen into the beamline.
2. Tune the beam to hit the BeO screen as cleanly as possible.
3. Carefully tune the quadrupoles to focus the beam. Typical currents were roughly 1.4 A for the upstream (horizontal) quadrupole, and 1.2 A for the downstream (vertical) quadrupole.
4. Use the steering coils to move the beam to the center of the BeO target. Preference was given to the upstream steerers, when possible, to keep the modifications as far from the target as possible.
5. Re-focus the beam after steering. Typically, only fine-tuning was required at this point in order to pass the beam through the hole in the BeO screen.
6. Start data acquisition:
 - (a) Turn on power to the detector
 - (b) Use the Arduino controller to set a threshold of approximately 700–800 (DAC units, equivalent to roughly 4096/5000 mV).
 - (c) Turn on the detector bias voltage
 - (d) Start the PyDAQ program
7. Tune the spectrometer to the electron-carbon peak
8. Adjust the *accelerator* controls in order to minimize noise and optimize the signal quality. Typically, a quarter-turn or less of the solenoid current fine-control was necessary, with perhaps some steering adjustments. It was verified that these had little to no effect on the beam spot seen by the BeO screen.
9. Continue acquisition for Møller and electron-carbon data

Chapter 6

Data Analysis and Results

Commissioning data were acquired throughout the Spring of 2018. Data sets intended for analysis were not acquired until after additional lead shielding was installed at the end of May. This ensured that the following acquisition runs were as free from noise as possible.

In the end, data for Møller scattering and electron-carbon scattering were acquired at the angles of 30° , 35° , and 40° at a beam energy of 2.5 MeV. Data were acquired in individual runs of approximately 60 seconds, in order to be able to isolate issues from the beam becoming unstable should the need arise. The acquisition rates were high enough that 60 seconds were plenty for statistical errors to shrink to the size of the systematics.

6.1 Construction of a Matching Simulation

A Geant4 simulation of the experiment was constructed, conceived to be as true to the actual physical design as possible. Nearly all major design components were included, coded in the form of GDML (Geometry Description Markup Language). A Python interface was used to produce the geometry files (see App. B.2). The resulting model can be seen in Fig. 6-1. The magnetic field of the spectrometer reflects a realistic map calculated from the SolidWorks model, using Ansys Maxwell software. The target foil, lead shielding, internal vacuum, Kapton windows, and external air gap were all included in the simulation.

The detector was modeled to closely reflect reality: each scintillating tile was afforded its own physical volume. Hit locations were determined by finding the intersection point of the associated scintillating tiles, just as in the actual analysis. However, effects due to light yield and subsequent attenuation are not included.

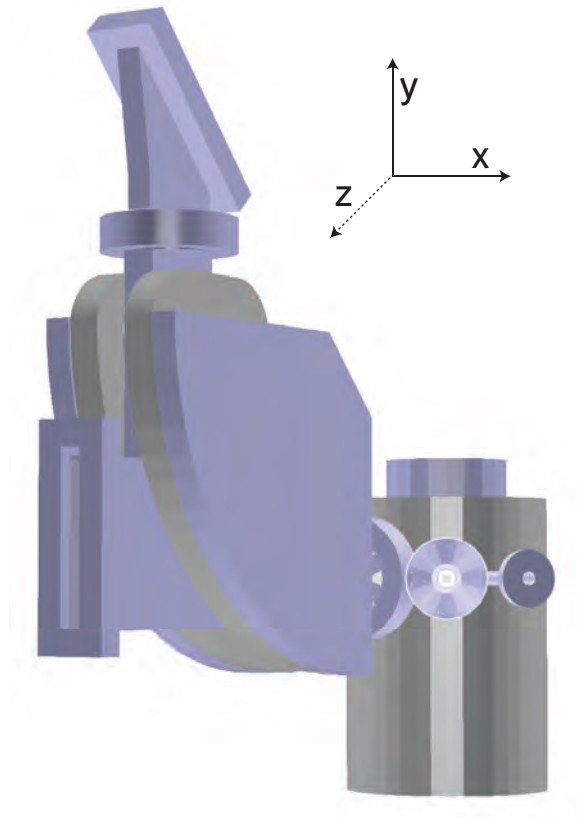


Figure 6-1: The GDML model of the detector, used in Geant4 simulations. The view is into the beamline.

6.1.1 Event Generators used in Simulation

The new radiative Møller generator was used extensively in the simulations. However, a non-radiative Born-level generator was used for comparison and testing. In addition, the radiative electron-proton event generator used by OLYMPUS [37] was modified to represent the electron-carbon interaction ($G_E = 6$, $G_M = 0$). Since the beam energy is too low to trigger excitations in the carbon atoms, this is a reasonable approximation. This generator was used primarily to determine if any significant backgrounds were caused by electron-carbon scattering; none were found.

6.1.2 Consideration of Systematic Uncertainties

The simulation bands trace out the envelope of a large number of simulations performed over a range of possible values of the beam-related parameters. Such parameters are detailed in Table 6.1. In this way, systematics were introduced

into the comparison between data and theory.

Table 6.1: Selected systematic uncertainties included in simulations.

Measurement angle	$\pm 0.75^\circ$
Beam angular spread	1.0° to 1.05°
Beam energy	-75 keV to +10 keV
Effective target multiple scattering	$0.25 \times 2.0 \text{ g/cm}^3$ carbon at $2 \mu\text{m}$

The measurement angle uncertainty, $\pm 0.75^\circ$, represents uncertainty on both the beam angle and the spectrometer angle. It is, however, dominated by uncertainty on the beam angle: this is bounded only by the pipe diameter.

The beam energy uncertainty is asymmetric, due to two sources of uncertainty. Chathan Cooke has on occasion measured the beam energy, and has found that the GVM readout is accurate to within about 5–10 keV. However, a recent measurement, performed by extracting the bremsstrahlung endpoint with a LaBr scintillator [38], indicates that the beam energy is roughly 75 keV below the GVM readout. With no data to break the tie, the entire range was used in the uncertainty estimation (fortunately, the effects were small).

The beam angular spread was derived from an estimate of the beam’s transverse geometric emittance. The beam spot size had been measured, in previous years, at a location corresponding to the upstream-most end of our experiment. Here, it was seen to be as small as 1 mm, with proper tuning. The vacuum pipe, however, can accommodate a beam as wide as roughly 1 cm. During the commissioning run, the beam spot was observed to be approximately 1'' in diameter, 2 m downstream at the BeO screen. From this, an angular divergence can be derived, thus providing an emittance when combined with the corresponding upstream spot size. In normal operation, the beam spot can be focused down to a diameter of approximately 1/8'' at the target. Combining this with the estimated emittance yields an angular spread.

The angular spread due to the divergence, and due to multiple scattering in the target are separate yet intertwined effects. Multiple scattering in the target is an effect that is largest at large angles, since the electrons pass through more of the target. On the other hand, effects due to the beam emittance are mostly independent of angle. By adjusting the magnitude of these two effects, the simulations were matched to the data. This involved omitting simulated spectra that were inconsistent with the data. The data indicate a level of multiple scattering consistent with one-fourth what would be expected for a $2 \mu\text{m}$ target at a density of 2.0 g/cm^3 . This could indicate that the target is either thinner than expected, less dense, or that Geant4 is not handling multiple

scattering accurately for such a thin material. An additional beam angular spread of approximately 1.0° to 1.05° is consistent with both the data and the emittance estimation. Significantly different values of the target thickness and the beam angular spread were inconsistent with the acquired spectra.

6.2 Calibration of the Spectrometer Mapping

A necessary component of the analysis is the conversion between momentum and hit position on the detector. Being located on the focal plane, this conversion should be approximately, although not exactly linear. A method was devised to calculate this by adjusting the magnet current.

The calibration was performed using the elastic electrons, which have a uniform momentum. Rather than stepping the electron energy and extracting the calibration, the magnetic field was stepped, as this has an equivalent effect. Assuming that the magnet current is directly proportional to the magnitude of the magnetic field, it can be used as a proxy.

The elastic peak was swept across the focal plane detector by varying the magnet current. The position was determined by a Gaussian fit to the top of the peak (Fig. 6-2). The extracted position of the elastic peak (tile number), as a function of magnet current, is shown in Fig. 6-3. The last data point differs from the general trend due to problems in the fit at the detector edge; it was thus omitted from further portions of the analysis.

The magnet current was then translated to an effective electron momentum, and the data fit to a third-order polynomial. An orthogonal distance regression was used, owing to the presence of both x and y error bars. The result can be seen in Fig. 6-4.

The exact same procedure was repeated with the simulated detector, in order to extract a mapping for use on the simulated data (Fig. 6-5). This was done in order to help mitigate effects resulting from differences between the simulated and real magnetic field maps. By performing the calibration twice, and using the simulated map for simulated data, and the experimental map for real data, these discrepancies can be largely cancelled.

6.3 Estimation of the Detector Efficiencies

Effects of light attenuation are clearly visible in the data. This attenuation was modeled, fit, and then the data were corrected. A double-exponential model was used as a starting point for the model. This contains two terms: one for light attenuated as a result of internal reflection, and a term for light attenuated

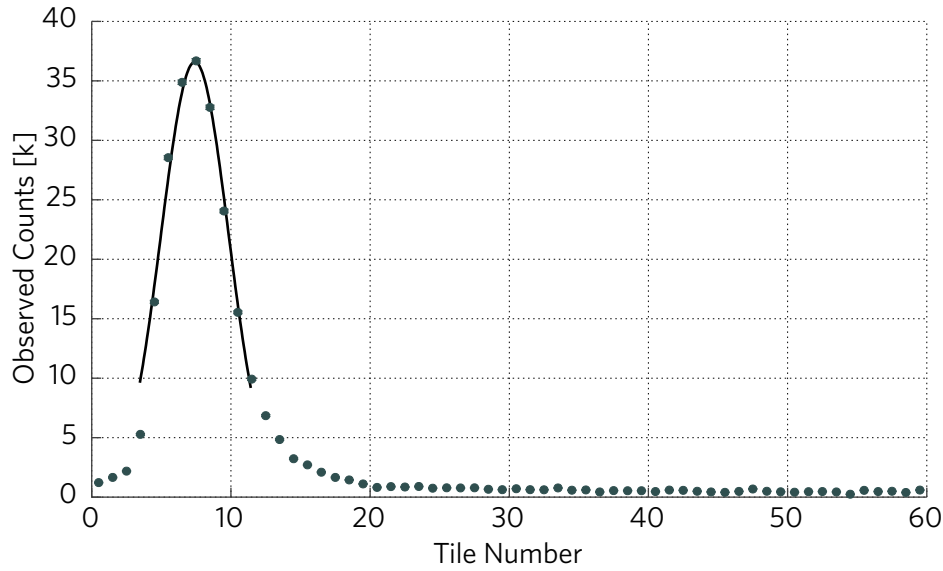


Figure 6-2: Fit used to determine the location of the elastic peak. The y axis is in thousands of counts. The fit indicates a peak location of 7.41 ± 0.07 (effective tile number).

in the bulk material. The bulk attenuation length is quoted by the manufacturer as 2.5 m, which indicates practically constant attenuation on the relevant short length scales. The rate R as a function of distance x was thus parameterized as:

$$R(x) = \exp(-x/l) + C \quad (6.1)$$

with free parameters l (reflective attenuation length) and C (bulk offset). The overall scale was fixed.

To extract the values of these parameters, two splines were fit around each edge of the detector: one on even tiles, and one on odd tiles (Fig. 6-6). With a proper correction for light attenuation, these splines should converge. The parameters of the correction model were then fit in order to minimize the difference between the splines.

The detector efficiencies were extracted from the data using an iterative unfolding method. The X and Y tiles were treated separately in each iteration. To calculate each cycle's X-tile efficiencies, splines were fit along the Y tiles. Then the tile efficiencies were then fit in order to minimize the sum, at every point, of the squared deviations of the splines from the data. The same method was used to find the Y-tile efficiencies, by fitting splines along the X tiles. The end result efficiencies were determined by multiplying the intermediate efficiencies of all of the iterations. The algorithm converged relatively quickly, in

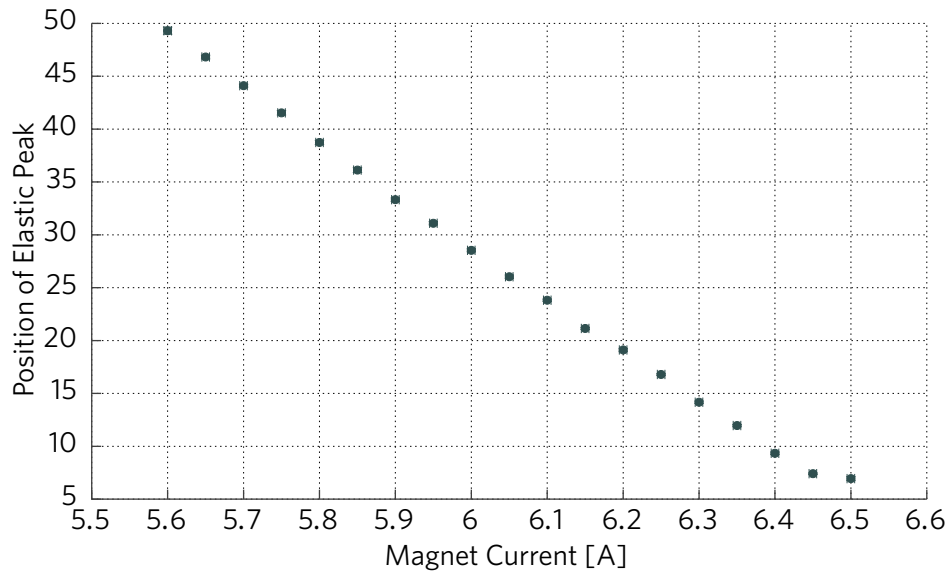


Figure 6-3: Mapping from magnet current to peak position.

roughly 25 or fewer iterations.

The iterative unfolding method is useful when the underlying “true” data can be well-represented by splines. To that end, spline-induced bias is minimized when the data are as flat and smooth as possible. Such “flat” spectra were generated by scanning the magnet current to methodically move the Møller peak across the detector (e.g. Fig. 6-8). Efficiencies were reconstructed from this relatively flat data set (Fig. 6-9), and then applied to the real data of interest. Some bias is unavoidable based on the validity of the assumptions, but it is ideally small in the region of interest. It is also important to note that this method can only provide the relative efficiency between the tiles, not the absolute efficiency. Likewise, it cannot account for long-range structure in the detector efficiency, only short-range tile-by-tile variation.

The efficacy of this reconstruction method was evaluated by using a toy model. Fake efficiencies were applied to a flat data set, which was then fed through the reconstruction algorithm. The efficiencies were drawn from a normal distribution with a mean of 1 and width of 0.05. Figure 6-7 shows the result of this, in which the efficiency parameters were reconstructed to roughly 10%. As a result, the error bars on the presented data points consist of both uncertainty from statistics, and that resulting from an estimated 10% uncertainty in the efficiency parameters. An example raw data set at 30° is shown in Fig. 6-10, which is reconstructed to that in Fig. 6-11. Note that there are three malfunctioning tiles. For comparison, a simulation at a single set of

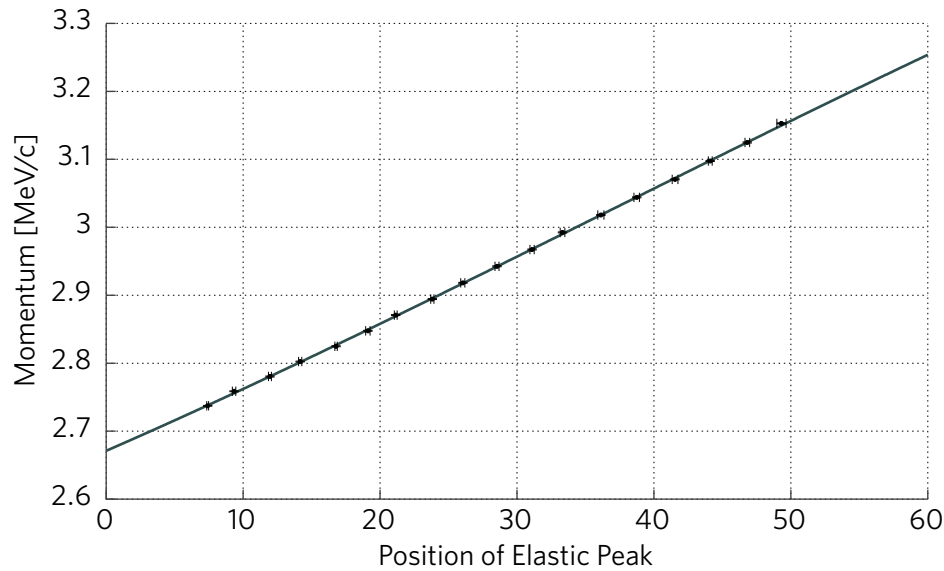


Figure 6-4: Mapping from hit position to momentum, for real data events.
 $\chi_r^2 = 1.12$.

parameters is shown in Fig. 6-12.

6.3.1 Detector Rate Linearity

The detector should have minimal effects from deadtime. The total acquisition rate did not exceed 20 kHz. The readout itself is intrinsically deadtime-free, but a 250 ns post-hit suppression time was added on a per-channel basis, in order to suppress false hits due to ringing effects. This indicates that there should be no significant effects until the rates approach the ~ 4 MHz level. This was tested by measuring the detector hit rate at a range of currents, as shown for both electron-carbon and Møller in Fig. 6-13. Typical beam currents during data acquisition ranged within 20–50 μA . The data do not indicate any obvious non-linearities, meaning that effects from pileup, deadtime, or TDC buffer overflow are insignificant.

6.4 Comparison of Data with Simulation

Figures 6-14, 6-15, and 6-16 show a comparison between the extracted Møller spectra and that reconstructed from a complete radiative simulation. The data have been scaled vertically to match. Small (sub percent-level) horizontal offsets were added to the data in order to optimize the overlap. These small offsets are consistent with uncertainties resulting from magnet hysteresis and

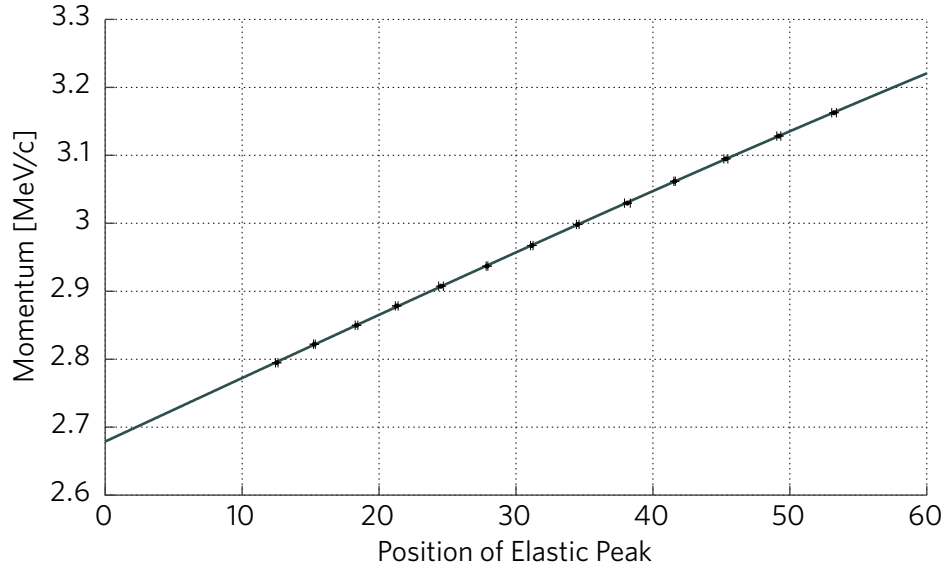


Figure 6-5: Mapping from hit position to momentum, for simulated events. $\chi_r^2 = 0.83$.

the intrinsic accuracy of the power supply. The full-scale momentum spectrum is shown in Fig. 6-17, demonstrating the relative positions of the electron-carbon and Møller peaks.

The absolute Møller cross-section was also extracted at these three angles, and compared with theory. The cross-sections were extracted by considering the ratio between the electron-carbon and Møller rates. The rate measured by the detector can be decomposed as:

$$R_i = \kappa I_i \sigma_i e_i, \quad (6.2)$$

where κ is defined as the geometric, unchanging part of the luminosity such that

$$\mathcal{L} = \kappa I = \left[\frac{\rho N_A t}{M_{\text{mol}} q_e} \right] I \quad (6.3)$$

with I is the beam current. The cross-section is represented by σ_i , and the detection efficiency as e_i . The ratio of the electron-carbon and Møller rates can then be expressed as

$$R_M/R_e = \frac{I_M}{I_e} \frac{\sigma_M}{\sigma_e} \frac{e_M}{e_e}. \quad (6.4)$$

The Møller cross-section can be extracted:

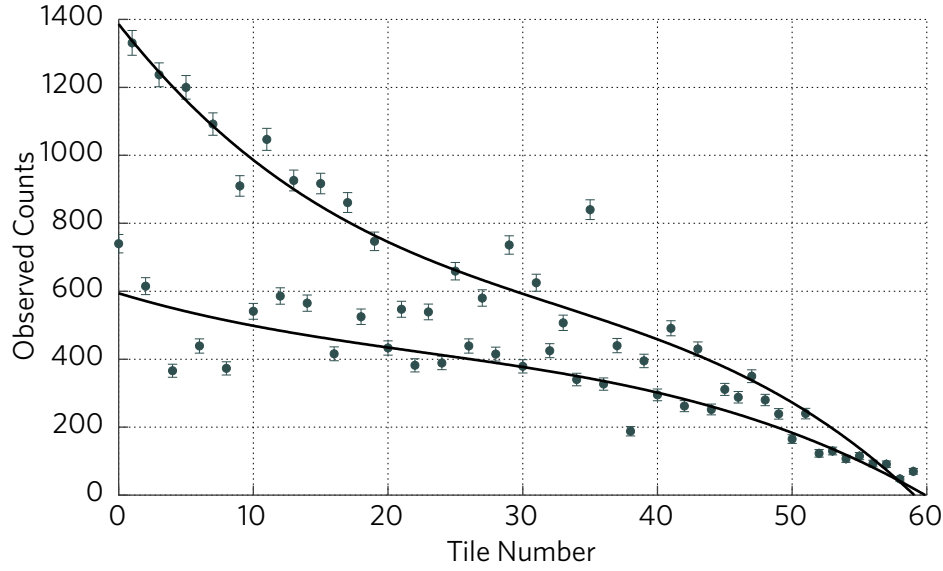


Figure 6-6: Example of an even-odd dual-spline fit used to extract the attenuation length. Only statistical errors are shown (efficiencies have not yet been corrected).

$$\sigma_M = \sigma_e \left(\frac{R_M}{R_e} \right) \left(\frac{I_e}{I_M} \right) \left(\frac{e_e}{e_M} \right). \quad (6.5)$$

The beam currents I_e and I_M are provided by the Faraday Cup data. Two models of calculating σ_e were considered: with and without radiative corrections. The model presented in [1] was used for the non-radiative estimates. The modified OLYMPUS electron-proton radiative generator, mentioned earlier, was used for the radiative-corrected model [37].

The values of e_e and e_M were estimated from the Monte Carlo simulation by comparing the predictions of the raw generator and full Geant4 simulation. It should be noted that this estimation has a nonzero dependence on the detector threshold set in Geant4, with no principled way to assign a quantitative error. This is exacerbated by the high threshold required by the noisy amplifier/discriminator cards (with which the simulations must match as best as possible), since the effect is larger at higher thresholds. A future iteration of the experiment should aim to better constrain this quantitatively, or circumvent the issue with quieter cards.

Figures 6-18 and 6-19 show the extracted cross-sections. Comparisons are shown between the data (extracted with the radiative and non-radiative electron-carbon cross-sections) and both the non-radiative and radiative-corrected Møller theory. At all three angles, reasonable agreement is observed. All three

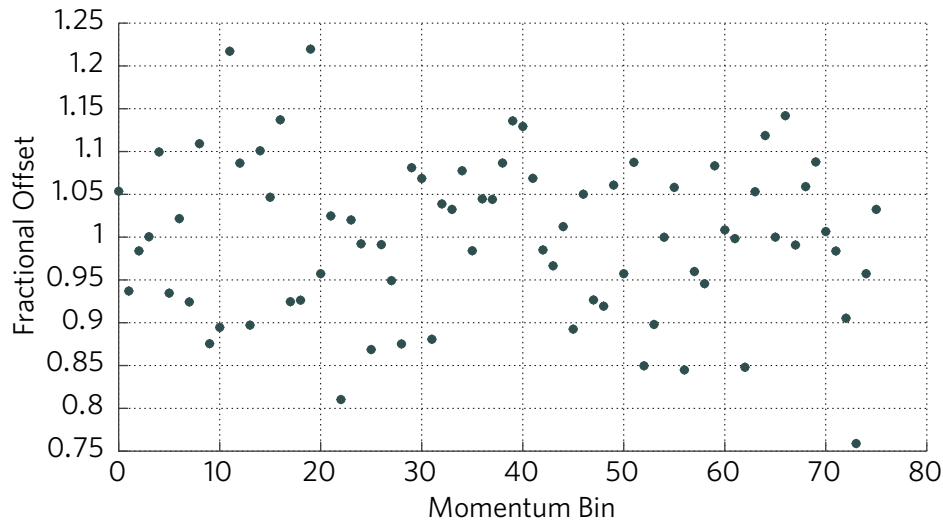


Figure 6-7: Recovered efficiency parameters compared with truth, for a toy model. The distributions have been normalized.

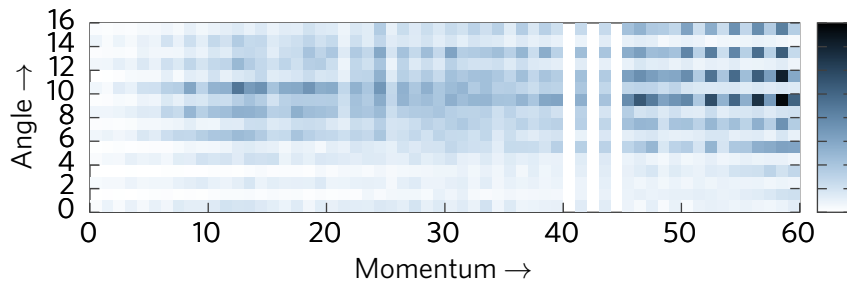


Figure 6-8: Raw constructed “flat” hit map used for efficiency reconstruction (linear color scale).

cross-sections are on the order of 10^{10} pb/° (integrated over 2π in ϕ).

6.5 Discussion and Future Directions

The data acquired show good agreement with the predictions of the new radiative theoretical calculation. The shape of the spectra at 30° , 35° , and 40° are well-described: this was the primary goal set out at the beginning of this experimental effort. Some deviations from the general trend are seen in the 30° comparison, although these fall within the error bars. Future iterations of this experiment should be able to improve upon the precision of this measurement.

Figure 6-20 shows a comparison between Geant4 simulations with the

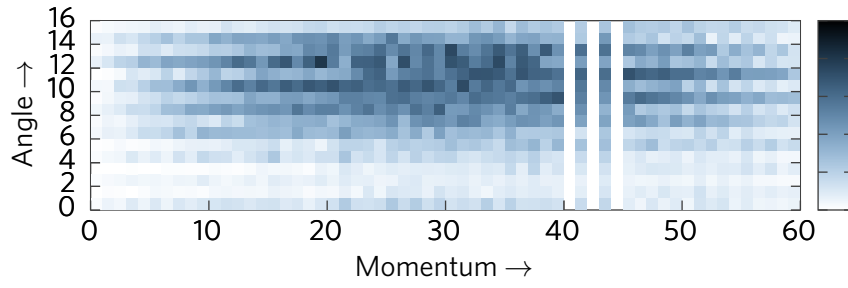


Figure 6-9: Recovered “flat” hit map after efficiency reconstruction (linear color scale).

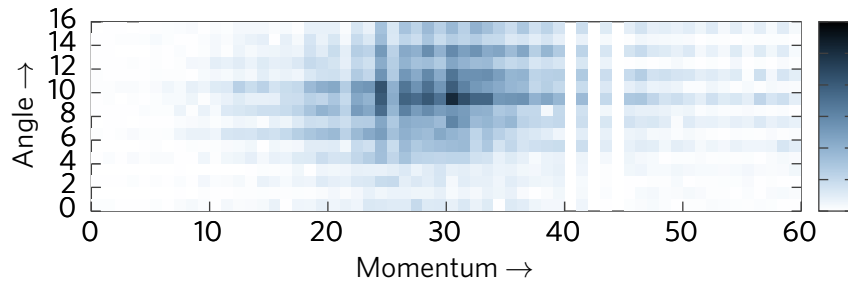


Figure 6-10: Raw hit data at 30° (linear color scale).

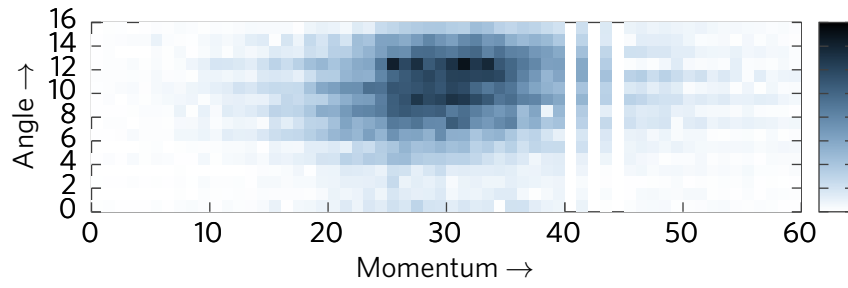


Figure 6-11: Recovered hit data at 30° (linear color scale).

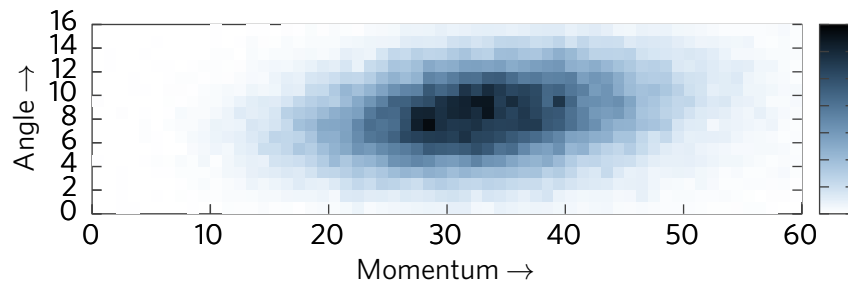


Figure 6-12: Simulated hit data at 30° (linear color scale).

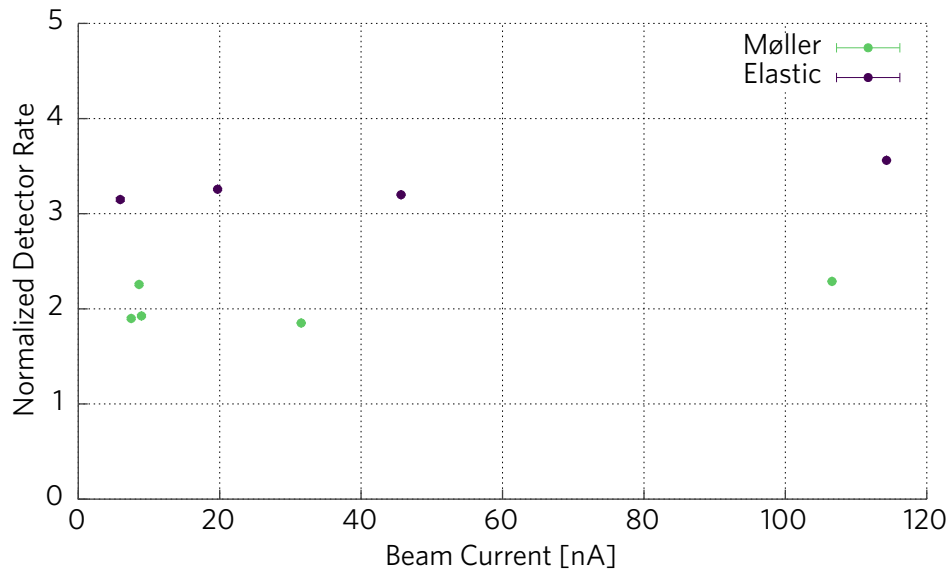


Figure 6-13: Normalized rate as a function of beam current.

radiative generator and with the non-radiative generator, at the single central values of the beam parameter scan at 30° . The comparison is shown for both nominal beam emittance, and a low beam emittance (characterized by no angular spread at the target). Small differences between the spectra are visible, although they are much more obvious with lower beam angular spread. It follows that even if we were to understand the systematics perfectly, i.e. no uncertainty in the beam angle, beam energy, target thickness, or beam emittance, it would still be quite difficult to see a difference between the radiative and non-radiative spectra. Only with significant improvements to the apparatus would the differences become apparent.

As a result, an initial area upon which to focus is the beam emittance. Effects due to target multiple scattering and beam angular spread are among the biggest effects blurring the measured spectrum. The installation of an upstream collimator could help to reduce both the beam spot size and the angular spread. An additional significant effect is the distance between the focal plane detector and the associated Kapton vacuum window. A future iteration of the detector could be constructed to fit closer to the window, thus reducing the lever arm on multiple scattering effects. Simulations have shown that replacing the air with a helium bag would not significantly reduce these effects; they are really a result of multiple scattering in the window. A measurement at higher beam energy would also help to mitigate these effects. In order to substantially improve the precision of this measurement, many of these facets will need to be addressed.

Møller Data vs Simulation: 30°

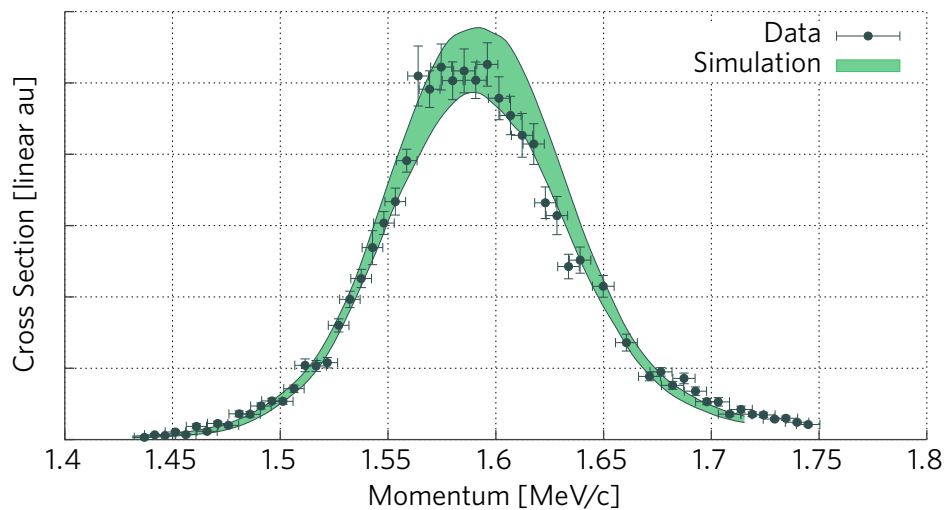


Figure 6-14: Data versus simulation at 30°.

Møller Data vs Simulation: 35°

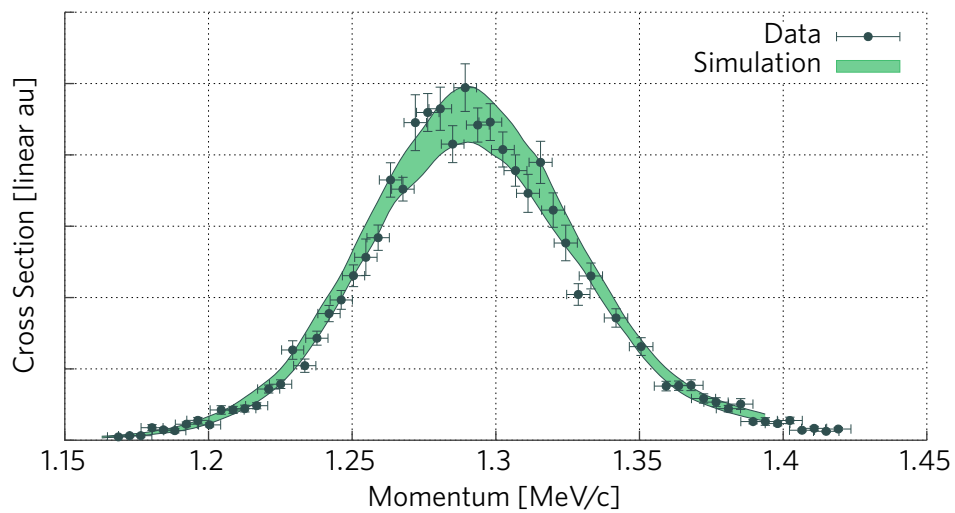


Figure 6-15: Data versus simulation at 35°.

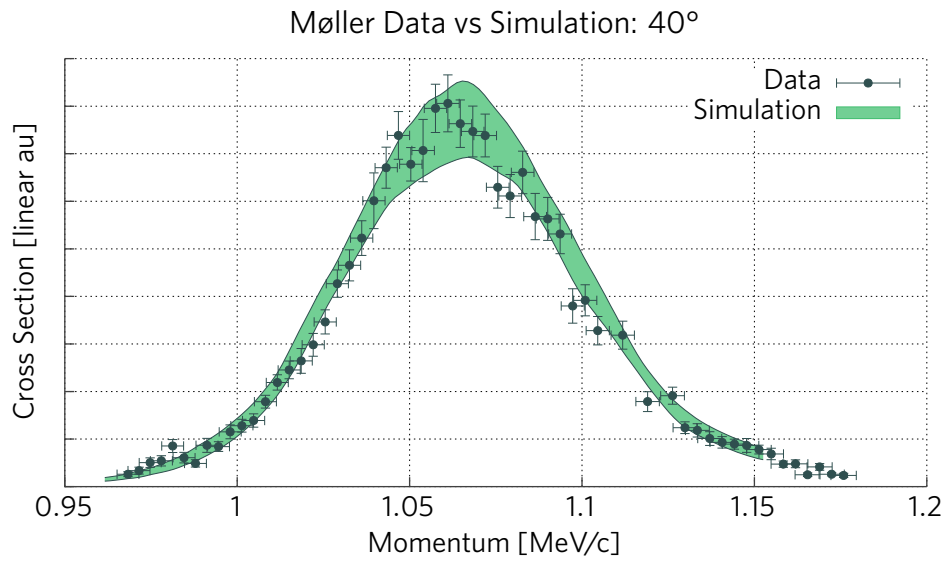


Figure 6-16: Data versus simulation at 40°.

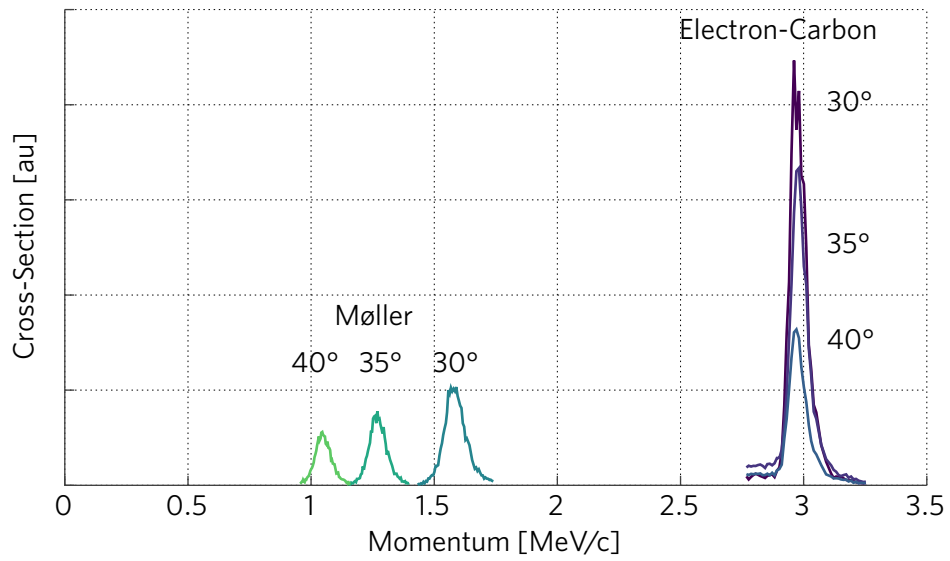


Figure 6-17: Full-scale momentum spectrum at 30°, showing the Møller and electron-carbon peaks.

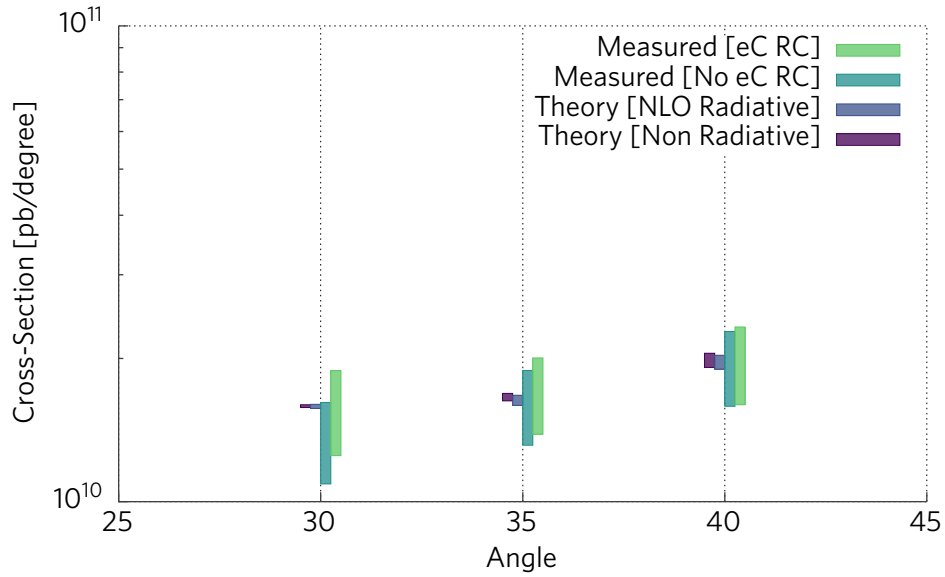


Figure 6-18: Extracted Møller cross-section, compared with theoretical calculations.

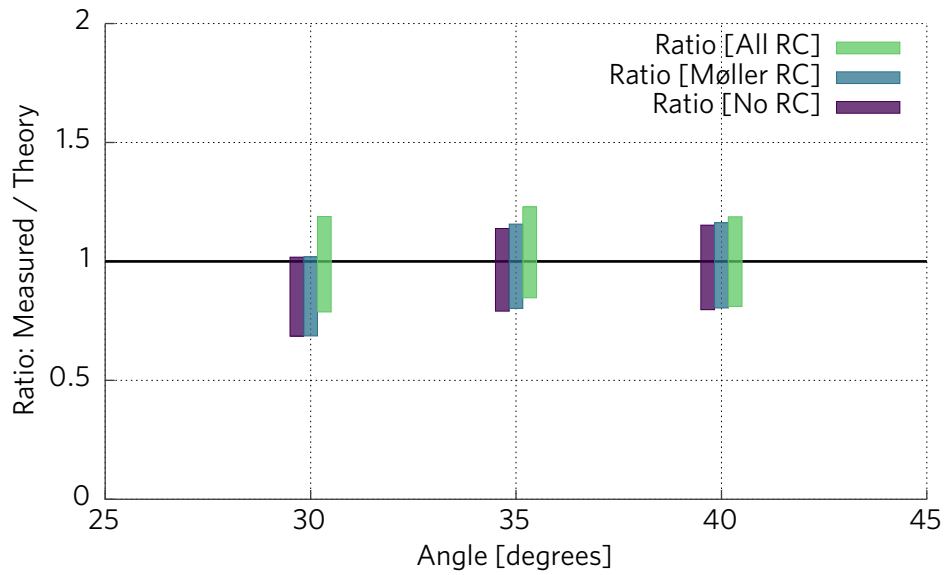


Figure 6-19: Ratio of measured Møller cross-section to theoretical calculations.

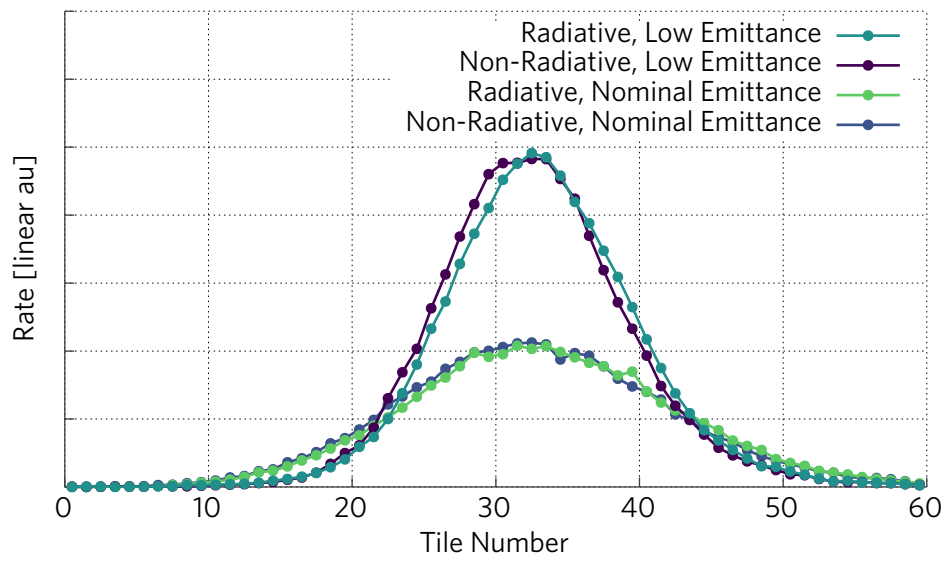


Figure 6-20: Radiative versus non-radiative simulation at 30°, for nominal and low-emittance beams.

Appendix A

DAQ and TDC Software Documentation

A.1 DAQ Code Documentation

The following section describes the various classes (▶) and methods (▷) provided by the DAQ software. Section A.4 shows an example run script.

▶ `cdef class PyDAQ`

The data acquisition chain is controlled by this class.

▷ `def __init__(self, Reader, Processor, Detector)`

PyDAQ must be instantiated with a Reader, Processor, and Detector.

▷ `cpdef void PlotToPlotly(self)`

Display output using plot.ly

▷ `cpdef void PlotAsASCII(self)`

Display output in the terminal.

▷ `cpdef void StartReader(self)`

Begin reading in raw data.

▷ `cpdef void StartProcessor(self)`

Begin processing data into events.

▷ `cpdef void StartDetector(self, float accTime)`

Begin processing events into hit locations.

The variable `accTime` sets the refresh rate.

▷ `cpdef void Stop(self)`

Stop acquiring data.

A.1.1 Readers

► `cdef class BufferReader`

This reader is used when decoding the FIFO buffer.

▷ `def __init__(self, str fName, str lfName, str outFileName, double dt)`

The arguments are:

`fName` Input buffer file path.

`lfName` Output log file path.

`outFileName` Output PyTables file path.

`dt` Artificial channel deadtime (to suppress oscillation hits).

▷ `cpdef void NoSeek(self)`

Read from the end of the buffer rather than the top. Set this only when reading from a test buffer file.

▷ `cpdef void readDataStream(self, hitBuffer)`

Internal—contains the main decode loop.

▷ `cpdef void Start(self, hitBuffer)`

Internal—starts threading of the main loop.

▷ `cpdef void Stop(self)`

Internal—stops the thread.

► `cdef class TCPReader`

This reader is used when decoding a TCP/IP stream.

▷ `def __init__(self, addr)`

Must be instantiated with the IP address of the incoming stream.

▷ `cpdef void readDataStream(self, Processor)`

Internal—contains the main decode loop.

▷ `cpdef void Start(self, Processor)`

Internal—starts threading of the main loop. No Stop mechanism has been written yet.

A.1.2 Processors

► `cdef class DirectProcessor`

A minimal processor that shuttles hits from the raw buffer to the Detector.

▷ `def __init__(self)`

- ▷ cpdef void setup(self)
 - Internal*—reset.
 - ▷ cpdef void readStreamData(self, int channel, double hitTime)
 - Internal*—adds the channel–time pair to the stack.
 - ▷ cpdef void processStream(self, buffer)
 - Internal*—the main loop that reads from the raw buffer.
 - ▷ cpdef list getHits(self)
 - Internal*—called by the Detector to pull off hits.
 - ▷ cpdef void Start(self, buffer)
 - Internal*—starts threading of the main loop.
 - ▷ cpdef void Stop(self)
 - Internal*—stops the thread.
- cdef class CoincidenceProcessor
This processor evaluates coincidences.
- ▷ def __init__(self, double CoincidenceWindow)
 - Must me instantiated with the desired coincidence window.
 - ▷ cdef void setup(self, double CoincidenceWindow)
 - Internal*—reset.
 - ▷ cpdef void readStreamData(self, int channel, double hitTime)
 - Internal*—adds the channel–time pair to the stack.
 - ▷ cpdef void processStream(self, buffer)
 - Internal*—the main loop that reads from the raw buffer
 - ▷ cpdef list getHits(self)
 - Internal*—called by the Detector to pull off sets of coincidence hits.
 - ▷ cpdef void Start(self, buffer)
 - Internal*—starts threading of the main loop.
 - ▷ cpdef void Stop(self)
 - Internal*—stops the thread.

A.1.3 Detectors

- cdef class DirectTileArray
A minimal detector that displays all tiles that have been hit.

- ▷ `def __init__(self)`
- ▷ `cpdef tuple checkHit(self, int ch)`
Internal—checks that the channel maps to a physical tile, and if so, returns its location.
- ▷ `cpdef void SetHistory(self, double frac)`
Sets how much of the previous frame is displayed on the next. Useful for switching between real-time and long-term accumulation.
- ▷ `cpdef tuple processHits(self, hits)`
Internal—processes a list of channels.
- ▶ `cdef class CoincidenceTileArray`
A detector that displays coincidence coordinates.
 - ▷ `def __init__(self)`
 - ▷ `cpdef tuple checkPair(self, int ch1, int ch2)`
Internal—checks that the channels map to physical tiles, and that they are in different planes. If so, it returns their locations.
 - ▷ `cdef tuple getCoordinates(self, int topCh, int bottomCh)`
Internal—converts two channels to a physical hit coordinate.
 - ▷ `cpdef void SetHistory(self, double frac)`
Sets how much of the previous frame is displayed on the next. Useful for switching between real-time and long-term accumulation.
 - ▷ `cpdef tuple processHits(self, channelLists)`
Internal—process lists of coincidence-matched channels.
- ▶ `cdef class ChannelRates`
A “detector” that prints the channel rates to the terminal.
 - ▷ `def __init__(self)`
 - ▷ `cpdef np.ndarray processHits(self, hits)`
Internal—accumulates hit rates by channel number.

A.1.4 Internal / Auxiliary

- ▶ `class DataStorage(IsDescription)`
Internal—this defines the data structure of the PyTables file.
 - ▶ `class GlobalHeader(IsDescription)`

- EventID = Int64Col()
 - GEO = Int64Col()
- ▶ class EventData(IsDescription)
 - Channel = Int64Col()
 - ShortTime = Int64Col()
 - Trailing = Int64Col()
- ▶ class ETTT(IsDescription)
 - ExtendedTime = Int64Col()
- ▶ class GlobalTrailer(IsDescription)
 - Status = Int64Col()
 - WordCount = Int64Col()
 - GEO = Int64Col()
- ▶ cdef class EventBuilder

Internal—this is used to help construct sets of hits from the FIFO buffer's bunch information.

 - ▷ def __init__(self)
 - ▷ def AddEvent(self, channel, time, trailing)
 - ▷ def GetEvents(self)
 - ▷ def Sort(self)

Arranges the hits sequentially in time. This is required because they are not necessarily written to the buffer in correct temporal order. The Processors will not function properly if the hits are not ordered.
 - ▷ def Clear(self)
- ▶ cdef class HitBuffer

Internal—holds the raw hits and shuttles them between the Reader and the Processor.

 - ▷ def __init__(self)
 - ▷ cpdef void setup(self)
 - ▷ cpdef list getRawHits(self)
 - ▷ cpdef void AddHit(self, ch, time)

- ▷ `def SaveBuilder(builder,entry)`
Internal—this saves the content in the event builder to an entry in the PyTables file.
- ▷ `def ProcessStream(hitBuffer,builder)`
Internal—this passes the content in the event builder to the raw hit buffer.
- ▷ `cpdef void line(np.ndarray cols, term, int x, int y)`
Internal—prints a line of the hit map to the terminal.
- ▷ `cpdef void print_array(np.ndarray arr, term, int x, int y0)`
Internal—prints the hit map to the terminal.

A.2 File Documentation

The above classes and methods are arranged in the following files.

A.2.1 Readers.pyx

- ▶ TCPReader
- ▶ BufferReader
- ▶ DataStorage
- ▶ EventBuilder
- ▷ SaveBuilder
- ▷ ProcessStream

A.2.2 Detectors.pyx

- ▶ DirectTileArray
- ▶ CoincidenceTileArray
- ▶ ChannelRates

A.2.3 Processors.pyx

- ▶ DirectProcessor
- ▶ CoincidenceProcessor

A.2.4 Display.pyx

- ▷ line

- ▷ print_array

A.2.5 PyDAQ.pyx

- ▶ PyDAQ

- ▶ HitBuffer

A.3 Example TDC configuration script

```
#!/bin/bash

modprobe vme_ca91cx42 geoid=1
modprobe vme_vmivme7805

cd /usr/src/vmedrivers/v1190
make -j && insmod v1190.ko addr=0x1111
cd ..

#This sets the following trigger parameters:
#matchwindowwidth windowoffset
#extrasearchwindowwidth rejectmargin trigtimesubenabled
echo 0x7F0 0xF810 0x08 0x02 0x00 > /sys/bus/vme/devices/v1190.0-0/trigger
sleep 1

#This sets bits 5, 9, and 11 to the control register.
#Bit 5: integral nonlinearity compensation. Bits 9&11: ETTT
echo 0xa20 > /sys/bus/vme/devices/v1190.0-0/ctrl
sleep 1

#This disables the TDC Header and Trailer during readout
echo 0x3100 > /sys/bus/vme/devices/v1190.0-0/uC
sleep 1

#This sets the max number of hits per event.
#0x0009 means 1001 = unlimited.
echo 0x3300 > /sys/bus/vme/devices/v1190.0-0/uC
echo 0x0009 > /sys/bus/vme/devices/v1190.0-0/uC
sleep 1

#1 sets Trigger Matching Mode. 0 sets continuous storage mode
echo 1 > /sys/bus/vme/devices/v1190.0-0/storage_mode
```

A.4 Example Run Script

A basic minimum working example follows. This is a simplified version of what appears in RunDAQ.py.

```
#!/usr/bin/env python
from RadMollerPyDAQ import *
import sys, os
import signal

HISTORY = 0
COINCIDENCE_WINDOW = 2 #ns
ACC_TIME = 1.0 #s
BUFFER_PATH = "/sys/bus/vme/devices/v1190.0-0/data"
OUTPUT_FILE = "output.pt"
DEADTIME = 1000.0 #ns

Processor = CoincidenceProcessor(COINCIDENCE_WINDOW)
Detector = CoincidenceTileArray()
Reader = BufferReader(BUFFER_PATH, "logfile1.txt", OUTPUT_FILE, DEADTIME)

Detector.SetHistory(HISTORY)

DAQ = PyDAQ(Reader, Processor, Detector)
DAQ.PlotAsASCII()

#This is to correctly map ctrl-c to stop the DAQ
def signal_handler(*args):
    DAQ.Stop()
    os.system('cls' if os.name == 'nt' else 'clear')
    sys.exit()
signal.signal(signal.SIGINT, signal_handler)

DAQ.StartReader()
DAQ.StartProcessor()
DAQ.StartDetector(ACC_TIME)
```

THIS PAGE INTENTIONALLY LEFT BLANK

Appendix B

Software Development

B.1 The QSquared Data Analysis Toolkit

The QSquared data analysis toolkit was developed in order to support the work described in this thesis. However, it may be of use to the general community. QSquared is a set of extensions to existing data analysis packages, on which it is dependent, including ROOT, zodb, numpy, and Gnuplot. The extensions are intended to be useful for the average high-energy physics user, and include pythonic versions of objects like 3- and 4-vectors, 1D and 2D histograms, and some basic data structures and File IO. The emphasis is on ease of use, speed, and storage efficiency. Some highlights include:

- Code acceleration via Cython compilation, when appropriate
- 1D and 2D histogram classes with C back-end
- Direct interface with Gnuplot: allows histograms to be saved easily to a publication-quality PDF
- Various data structures (Histograms, Series, Line, etc)
- Fast and space-efficient object storage via the ZODB database back-end and using `zc.zlibstorage` compression
- Easy conversion from ROOT histograms to QSquared histograms
- Easy conversion of ROOT files to QSquared QFiles; more and more ROOT object formats are being supported as time goes on
- Easy interface with ROOT trees, etc, and conversion to QFiles
- Easy unit conversions and unit cancellation (factor-label). User can edit external units file.
- Uncertainty arithmetic and propagation

- PDG information about elementary particles, easy to access their mass, width, etc.
- Optional plotting Canvas with various automated plotting tools
- Various histogram color schemes available. The default is `veridis` from `matplotlib`, which is grayscale- and colorblind-safe. For 2D plots, a custom perceptually uniform color scheme is used.
- Beamer interface and utilities for generating slides out of plots made with `QSquared`

B.2 GDML Generation in Python

One way to prepare an experiment’s geometry for Geant4 simulations is to encode it in an XML-based GDML file. GDML provides a number of benefits to the user over hard-coded C++ (e.g. portability), but coding it directly is error-prone and requires dealing with complicated syntax. Colton O’Connor assembled software to allow GDML files to be generated from plain-text human-readable files. We have extended his software and produced a Python interface for preparing GDML files. The result allows complex geometries to be created using the simple syntax and object-oriented simplifications available to Python.

Some of the notes below will refer to items that are specific to the implementation for the Radiative Møller experiment. However, with proper renaming and rewriting, the framework could be used for any setup.

B.2.1 General Workflow

1. Code geometry using Python classes.
2. Execute Python program to generate GDML files.

B.2.2 Overview of File Contents

Python Front-End Interface

Files providing the front-end:

- `GDML_Shapes.py`
 - Contains code for the Python implementations of various geometric objects.
- `GDML_Util.py`

- Contains various utility functions that may be useful in coding the geometry.
- procGDML.py
 - This file runs all of the scripts necessary to generate GDML from a Python-coded model.

Plain-Text to GDML Converter

Colton's plain-text to GDML converter contains a number of files:

- generateGDML.py
 - This is the main file, in which the input and output filenames are specified.
- materials.txt
 - Various material definitions are stored here.
- gdmlModule.py
- olympusWriter.py
- writer.py

B.2.3 Classes and Methods

Geometry Classes

- Box(*name*, *dx*, *dy*, *dz*)
- Tube(*name*, *rmin*, *rmax*, *z*, *startphi*, *deltaphi*)
- SubtractionSolid(*name*, *solidA*, *solidB*, *pos*=[0,0,0], *rot*=[0,0,0])

There are two other types of solids that have the same structure:

- UnionSolid(...)
- IntersectionSolid(...)
- Trapezoid(*name*, *dx1*, *dx2*, *dy1*, *dy2*, *dz*)
- Cone(*name*, *z*, *rmin1*, *rmin2*, *rmax1*, *rmax2*, *sphi*, *dphi*)
- EllipticalTube(*name*, *x*, *y*, *z*)
- UnionChain(*objs*)

- An object that helps if you want to Union together a number of objects. Put them in a list and pass it as the argument to UnionChain and it will return an object representing the Union of the objects in that list.

Other stuff

- Object (generic base class)
- Detector(*prefix*, *objs=[]*)
 - The main container class into which objects are (automatically) placed.

Auxiliary Definitions

Functions:

- CopyObject(*obj*)
 - Makes an implementation-safe copy of an object and appends "_copy" to the name (this can later be changed)
- degToRad(*x*)
 - Degrees to radians
- radToDeg(*x*)
 - Radians to degrees
- sqrSum(*l*)
 - Returns the square-root of the sum of the squared values in list *l*
- PolarPosition(*r*, *angle*, *height*)
 - Returns a list containing the x-y-z coordinates corresponding to the cylindrical coordinates *r*, *angle* (degrees), and *height*
- RotateX(*pos*, *angle*)
 - Returns a rotated list of coordinates corresponding to those in *pos* rotated around X by *angle*
- RotateY(*pos*, *angle*)
 - Same; Y axis

- `RotateZ(pos, angle)`
 - Same; Z axis
- `XYZtoZYX(v)`
 - A key function for placing objects rotated about multiple axes. When specifying `SetRotation(...)` the expected angles correspond to a rotation around Z, then Y, then X. However, it may be useful to describe rotations in the opposite direction. This function returns the ZYX version of a rotation specified in XYZ order.
- `minus(l)`
 - Returns a version of the list *l* with the signs of each element flipped
- `subtract(l1, l2)`
 - Subtracts the list *l2* from *l1*
- `add(l1, l2)`
 - Adds the lists *l1* and *l2*

Classes:

- `Centers`
 - Useful for keeping track of the center positions of stacked objects

Important Geometry Class Methods

- `Name()`
 - Returns the object's name
- `SetName(name)`
 - Set an object's name to *name*
- `SetVirtual()`
 - Set an object to be a placeholder, i.e., one that exists in the GDML but is not physically in the geometry. For example, if it is just being used as a block that is subtracted from another.
- `UnsetVirtual()`

- Opposite of SetVirtual()
- IsVirtual()
 - Returns true/false if an object is Virtual
- SetPosition($[x, y, z]$)
 - Set the physical position of the object to $[x, y, z]$. The default is $[0, 0, 0]$.
- SetRotation($[xr, yr, zr]$)
 - Set the physical rotation of the object to $[xr, yr, zr]$ (degrees). The default is $[0, 0, 0]$.
- GetPosition()
 - Return an object's position
- GetRotation()
 - Return an object's rotation
- SetMaterial(*mat*)
 - Set an object's material to *mat*, e.g. "G4_Al" (see materials.txt for options)
- SetColor(*color*)
 - Set an object's color; the default is "t663675714"
- SetSensitive()
 - Set an object to be a sensitive detector
- FillVacuum()
 - For objects that have an inner volume (e.g. tubes), this will return an object made of "G4_Galactic" that fills the inner volume and has the same position/rotation as the parent volume.

B.2.4 Project Structure

Begin the main detector file (in this case MollerDetector.py) with these lines:

```
from __future__ import division
from PyGeoGDML import *
```

Then, initialize a detector; for example:

```
MollerExp = Detector("Moller")
```

Here, “Moller” will be the output text-file prefix. Then, provide this instance to the base Object class by calling:

```
SETEXPERIMENT(MollerExp)
```

The point of this is that now all new instances of Object-derived classes will carry a reference to the Detector and can place the object in the geometry without extra lines of code.

Now define the geometry. For example:

```
A_BOX = Box("BoxName", 2, 3, 4)
A_BOX.SetMaterial("G4_Al")
A_BOX.SetPosition([1, 2, 3])
A_BOX.SetRotation([0, 25, 0])
```

At the end of the file, save the Detector by calling:

```
MollerExp.Save()
```

THIS PAGE INTENTIONALLY LEFT BLANK

Bibliography

- [1] W. W. Buechner, R. J. Van De Graaff, A. Sperduto, E. A. Burrill, and H. Feshbach, “Further Experiments on the Elastic Single Scattering of Electrons by Nuclei,” *Physical Review*, vol. 72, no. 8, pp. 678–679, 1947.
- [2] R. J. Van de Graaff, W. W. Buechner, and H. Feshbach, “Experiments on the Elastic Single Scattering of Electrons by Nuclei,” *Physical Review*, vol. 69, no. 9-10, pp. 452–459, 1946.
- [3] E. M. Lyman, A. O. Hanson, and M. B. Scott, “Scattering of 15.7-Mev Electrons by Nuclei,” *Physical Review*, vol. 84, no. 4, pp. 626–634, 1951.
- [4] F. E. Close, *An Introduction to Quarks and Partons*. New York: Academic Press, 1979.
- [5] R. Hofstadter and R. W. McAllister, “Electron scattering from the proton,” *Physical Review*, vol. 98, no. 1, pp. 217–218, 1955.
- [6] R. E. Taylor, “Deep inelastic scattering: The early years,” *Reviews of Modern Physics*, vol. 63, no. 3, pp. 573–595, 1991.
- [7] MOLLER Collaboration, “The MOLLER Experiment: An Ultra-Precise Measurement of the Weak Mixing Angle Using Møller Scattering,” *arXiv:1411.4088v2*, 2014.
- [8] K. S. Kumar, “The E158 experiment,” *European Physical Journal A*, vol. 32, no. 4, pp. 531–532, 2007.
- [9] J. C. Bernauer *et al.*, “The OLYMPUS Internal Hydrogen Target,” *Nucl. Instrum. Methods Phys. Res. A*, vol. 755, pp. 20–27, 2014.
- [10] C. S. Epstein and R. G. Milner, “QED radiative corrections to low-energy Møller and Bhabha scattering,” *Physical Review D*, vol. 94, p. 033004, Aug 2016.
- [11] A. Afanasev, E. Chudakov, A. Ilyichev, and V. Zykunov, “MERADGEN 1.0: Monte Carlo generator for the simulation of radiative events in parity conserving doubly-polarized Møller scattering,” *Computer Physics Communications*, vol. 176, pp. 218–231, Feb 2007.

- [12] G. Balossini, C. M. C. Calame, G. Montagna, O. Nicosini, and F. Piccinini, “Matching perturbative and parton shower corrections to Bhabha process at flavour factories,” *Nuclear Physics B*, vol. 758, no. 1–2, pp. 227–253, 2006.
- [13] C. M. C. Calame, G. Montagna, O. Nicosini, and F. Piccinini, “The BABAYAGA event generator,” *Nuclear Physics B - Proceedings Supplements*, vol. 131, pp. 48–55, 2004.
- [14] Y. S. Tsai, “High-Energy Electron-Electron Scattering,” *Phys Rev*, vol. 120, no. 1, pp. 269–286, 1960.
- [15] A. B. Arbuzov and E. S. Scherbakova, “Next-to-Leading-Order Corrections to Bhabha Scattering in Renormalization Group Approach (I): Soft and Virtual Photonic Contributions,” *JETP Letters*, vol. 83, no. 10, pp. 427–432, 2006.
- [16] A. Ilyichev and V. Zykunov, “Lowest order QED radiative corrections to longitudinally polarized Moller scattering,” *Phys Rev D*, vol. 72, no. 3, p. 33018, 2005.
- [17] A. Denner and S. Pozzorini, “Electroweak radiative corrections to polarized Moller scattering at high energies,” *The European Physical Journal C*, vol. 7, no. 2, pp. 185–195, 1999.
- [18] N. Kaiser, “Radiative corrections to lepton-lepton scattering revisited,” *J. Phys. G: Nucl. Part. Phys.*, vol. 37, no. 11, p. 115005, 2010.
- [19] I. Akushevich, H. Gao, A. Ilyichev, and M. Meziane, “Radiative corrections beyond the ultra relativistic limit in unpolarized ep elastic and Møller scatterings for the PRad Experiment at Jefferson Laboratory,” *The European Physical Journal A*, vol. 51, no. 1, pp. 1–10, 2015.
- [20] D. R. Yennie, S. C. Frautschi, and H. Suura, “The Infrared Divergence Phenomena and High-Energy Processes,” *Annals of Physics*, vol. 13, pp. 379–452, 1961.
- [21] T. Hahn, “A Mathematica Intefrace for FormCalc-generated Code,” *arXiv:hep-ph/0611273*, 2006.
- [22] E. Haug and W. Nakel, *The Elementary Process of Bremsstrahlung*. World Scientific Publishing Co. Pte. Ltd., 2004.
- [23] S. Jadach, “Foam: A general-purpose cellular Monte Carlo event generator,” *Computer Physics Communications*, vol. 152, no. 1, pp. 55–100, 2003.
- [24] F. Berends and R. Gastmans, “Hard photon corrections for $e^+e^- \gamma\gamma$,” *Nuclear Physics B*, vol. 61, pp. 414–428, Sep 1973.

- [25] “Magnetic spectrometers,” *Chris Tschalär, personal communication.*, 2014.
- [26] R. Alarcon, S. Balascuta, S. V. Benson, W. Bertozzi, J. R. Boyce, R. Cowan, D. Douglas, P. Evtushenko, P. Fisher, E. Ihloff, N. Kalantarians, A. Kelleher, R. Legg, R. G. Milner, G. R. Neil, L. Ou, B. Schmookler, C. Tennant, C. Tschalär, G. P. Williams, and S. Zhang, “Transmission of megawatt relativistic electron beams through millimeter apertures,” *Physical Review Letters*, vol. 111, no. 16, 2013.
- [27] “Diamond-like Carbon Foils,” <http://www.micromatter.com/FoilsforBeamStripping.aspx>, 2017.
- [28] NIST, “ESTAR: Stopping-power and Range Tables for Electrons,” 2015.
- [29] “General Purpose Plastic Scintillator Datasheet,” *Eljen Technology*, 2016.
- [30] “Scintillating Optical Fibers Datasheet,” *Saint-Gobain Crystals*, 2016.
- [31] “Hamamatsu MPPC S13360-2050VE/-3050VE/-6050VE Datasheet,” *Hamamatsu Photonics*, 2016.
- [32] C. Sosolik, A. Lavery, E. Dahl, and B. Cooper, “A technique for accurate measurements of ion beam current density using a Faraday cup,” *Review of Scientific Instruments*, vol. 71, no. 9, pp. 3326–3330, 2000.
- [33] J. Prokúpek, J. Kaufman, D. Margarone, M. Krús, A. Velyhan, J. Krása, T. Burris-Mog, S. Busold, O. Deppert, T. E. Cowan, and G. Korn, “Development and first experimental tests of Faraday cup array,” *Review of Scientific Instruments*, vol. 85, no. 1, p. 013302, 2014.
- [34] A. Luches, V. Nassisi, and M. R. Perrone, “Movable Faraday cup for high-intensity electron beam pulses,” *Review of Scientific Instruments*, vol. 56, no. 5, pp. 758–759, 1985.
- [35] Keithley, “6517B Electrometer/High Resistance Meter Datasheet,” 2016.
- [36] CAEN SpA, *Technical Information Manual: V1190 A/B, VX1190 A/B Multihit TDCs*, rev. 14 ed., Nov 2016.
- [37] R. Milner, D. K. Hasell, *et al.*, “The OLYMPUS Experiment,” *Nucl. Instrum. Methods Phys. Res. A*, vol. 741, pp. 1–17, 2014.
- [38] J. R. Vavrek, B. S. Henderson, and A. Danagoulian, “Experimental demonstration of an isotope-sensitive warhead verification technique using nuclear resonance fluorescence,” *Proceedings of the National Academy of Sciences of the United States of America*, vol. 115, no. 17, pp. 4363–4368, 2018.